Photo-induced Charge Carrier Dynamics in Nanostructured Hybrid Systems for Solar Energy Conversion

Peng Han

Photo-induced Charge Carrier Dynamics in Nanostructured Hybrid Systems for Solar Energy Conversion
Peng Han

Photo-induced Charge Carrier Dynamics in Nanostructured Hybrid Systems for Solar Energy Conversion

Photo-induced Charge Carrier Dynamics in Nanostructured Hybrid Systems for Solar Energy Conversion

ACADEMISCH PROEFSCHRIFT

ter verkrijging van de graad van doctor
aan de Universiteit van Amsterdam
op gezag van de Rector Magnificus
prof. dr. ir. K.I.J. Maex
ten overstaan van een door het College voor Promoties
ingestelde commissie,
in het openbaar te verdedigen
op dinsdag 2 juni 2020, te 12:00 uur

door

Peng Han

geboren te Sichuan

PROMOTIECOMMISSIE

Promotor:	prof. dr. M. Bonn	Universiteit van Amsterdam
Copromotor	dr. E. Cánovas Díaz	IMDEA Nanociencia
Overige Leden:	prof. dr. A.F. Koenderink	Universiteit van Amsterdam
	dr. A. de Visser	Universiteit van Amsterdam
	dr. C. de Mello Donegá	Universiteit Utrecht
	prof. dr. M.S. Golden	Universiteit van Amsterdam
	prof. dr. L.D.A. Siebbeles	TU Delft

Faculteit der Natuurwetenschappen, Wiskunde en Informatica

The work described in this thesis was carried out at the *Max-Planck-Institut für Polymerforschung* (MPIP, Ackermannweg 10, 55128, Mainz, Germany).

This thesis is dedicated to all lives suffering from coronavirus disease 2019.

PUBLICATIONS COVERED IN THIS THESIS

Chapter 3:

P. Han, I.C.Y. Hou, H. Lu, X-Y. Wang, K. Müllen, M. Bonn, A. Narita and E. Canovas. Chemisorption of graphene quantum dots on metal oxide films greatly accelerates interfacial electron transfer. *J. Phys. Chem. Lett.*10,7 (2019): 1431-1436

Chapter 4:

P. Han, X.L. Yao, Q. Chen, M. Bonn, K. Müllen, A. Narita and E. Canovas. Size-dependent electron transfer from atomically defined nanographenes to metal oxide nanoparticles. *In preparation*

Chapter 5:

P. Han‡, R.H. Dong‡, H. Arora, M. Ballabio, M. Karakus, Z. Zhang, C. Shekhar, P. Adler, P. St. Petkov, A. Erbe, S.C.B. Mannsfeld, C. Felser, T. Heine, M. Bonn, X. Feng and E. Canovas. High-mobility band-like charge transport in a semiconducting two-dimensional metal–organic framework. *Nature Materials*.17,11 (2018):1027

OTHER PUBLICATIONS

C.Q. Yang, R.H. Dong, M. Wang, P.St. Petkov, Z.T. Zhang, M.C. Wang, P. Han, M. Ballabio, S.A. Bräuninger, Z.Q. Liao, J.C. Zhang, F. Schwotzer, E. Zschech, H-H. Klauss, E. Canovas, S. Kaskel, M. Bonn, S.Q. Zhou, T. Heine and X.L. Feng. A semiconducting layered metal-organic framework magnet. *Nature communications*.10,1 (2019): 3260

K.Y. Jiang, I.A. Baburin, P. Han, C.Q. Yang, X.B. Fu, Y.F. Yao, J.T. Li, E. Canovas, G. Seifert, J.S. Chen, M. Bonn, X.L. Feng, X.D. Zhuang. Interfacial approach toward benzene-bridged polypyrrole film-based micro-supercapacitors with ultrahigh volumetric power density. *Adv. Funct. Mater*. (2019): 1908243

CONTENTS

OUTLINE **11**

CHAPTER 1: NANOSTRUCTURED HYBRID MATERIALS FOR SOLAR ENERGY CONVERSION **14**

1.1 SOLAR ENERGY CONVERSION 14
1.1.1 Photovoltaics (PV) 14
1.1.2 Photocatalytic water splitting 17
1.2 NANOGRAPHENES AS SUNLIGHT ABSORBERS IN DYE-SENSITIZED SOLAR CELLS 19
1.2.1 Dye-sensitized solar cells (DSSCs) 19
1.2.2 Nanographenes in DSSCs 23
1.2.3 Photo-induced electron transfer at the sensitized interfaces 24
1.3 METAL ORGANIC FRAMEWORKS 26
1.3.1 Overview 26
1.3.2 Charge transport in MOFs 28
REFERENCES 31

CHAPTER 2: TIME-RESOLVED TERAHERTZ SPECTROSCOPY **36**

2.1 OVERVIEW 36
2.2 EXPERIMENTAL SETUP 37
2.3 OPTICAL-PUMP TERAHERTZ-PROBE SPECTROSCOPY 39
2.4 EXTRACTING PHOTOCONDUCTIVITY 40
2.5 CONDUCTIVITY MODELS 44
2.5.1 Drude model 45
2.5.2 Drude-Smith model 47
REFERENCES 49

CHAPTER 3: CHEMISORPTION OF ATOMICALLY PRECISE 42-CARBON GRAPHENE QUANTUM DOTS ON METAL OXIDE FILMS GREATLY ACCELERATES INTERFACIAL ELECTRON TRANSFER **50**

3.1 INTRODUCTION AND AIM OF THE WORK 50
3.2 METHODS 51
3.2.1 Materials 51

3.2.2 Synthesis 52
3.2.3 Characterization 52
3.3 RESULTS AND DISCUSSION 53
3.3.1 OPTP characterization 53
3.3.2 Gas-phase DFT calculations 55
3.3.3 Absorbance & Valence Band XPS 57
3.4 SUMMARY 58
3.5 APPENDIX 59
3.5.1 Materials and methods 59
3.5.2 Supplementary figures 63
REFERENCES 70

CHAPTER 4: SIZE-DEPENDENT ELECTRON TRANSFER FROM ATOMICALLY DEFINED NANOGRAPHENES TO METAL OXIDE NANOPARTICLES 76

4.1 INTRODUCTION AND AIM OF THE WORK 76
4.2 METHODS 78
4.2.1 Materials 78
4.2.2 Synthesis 78
4.2.3 Characterization 79
4.3 RESULTS AND DISCUSSION 79
4.3.1 Size-dependent HOMO-LUMO gaps in NGRs 79
4.3.2 OPTP characterization 80
4.3.3 Marcus theory interpretation 82
4.4 SUMMARY 84
4.5 APPENDIX 85
4.5.1 Extracting HOMO-LUMO gaps from absorption measurements of nPAHs dispersed in the Toluene 85
4.5.2 Extracting driven force for hot ET process as the difference of LUMO PAH levels (inferred from gas phase DFT) and SnO_2 CB edge level 87
4.5.3 Extracting driven force for cool ET process by considering the stokes shift for PAHs combining absorption and emission spectrum 88
REFERENCES 88

CHAPTER 5: HIGH-MOBILITY BAND-LIKE CHARGE TRANSPORT IN A SEMICONDUCTING TWO-DIMENSIONAL METAL–ORGANIC FRAMEWORK 95

5.1 INTRODUCTION AND AIM OF THE WORK 95
5.2 METHODS 96

5.2.1 Materials 96
5.2.2 Synthesis of $Fe_3(THT)_2(NH4)_3$ 2D MOF film 97
5.2.3 AC conductivity measurements by THz spectroscopy 97
5.2.4 Hall bar fabrication 97
5.2.5 Four-probe conductivity and Hall effect measurements 98
5.2.6 DFT modeling 98
5.3 RESULTS AND DISCUSSION 98
5.3.1 Synthesis and sample characterization 98
5.3.2 Photoconductivity of $Fe_3(THT)_2(NH4)_3$ 2D MOF by THz spectroscopy 101
5.4 SUMMARY 105
5.5 APPENDIX 106
5.5.1 Materials 106
5.5.2 General characterization 107
5.5.3 ^{57}Fe Mössbauer spectroscopy measurements 107
5.5.4 First-principle calculations of $Fe_3(THT)_2(NH_4)_3$ layers 108
5.5.5 Structural characterization of the $Fe_3(THT)_2(NH_4)_3$ 2D MOF film 109
5.5.6 Compositional analysis of the $Fe_3(THT)_2(NH_4)_3$ 2D MOF film 111
5.5.7 Analysis of Fe(II)/Fe(III) ratio from XPS data 112
5.5.8 ^{57}Fe Mössbauer spectra measurement 113
5.5.9 Analysis of Fe(II)/Fe(III) ratio from ^{57}Fe Mössbauer spectra 115
5.5.10 Element analysis of MOF sample 115
5.5.11 Analysis of electron transfer during the MOF synthesis 116
5.5.12 Electronic structure of $Fe_3(THT)_2$ 2D MOFs with NH_4^+ counter ions 117
5.5.13 Rational for the origin of the Urbach tail resolved by absorbance and its potential impact on THz spectroscopy 119
5.5.14 Photoconductivity of $Fe_3(THT)_2(NH_4)_3$ 2D MOFs by THz spectroscopy 120
5.5.15 Calculation of charge carrier density, quantum yield and mean free path 121
5.5.16 4-probe DC conductivity measurements 122
5.5.17 Hall Effect measurements 124
5.5.18 Analysis of reduced activation energy 128

5.5.19 DC conductivity of the $Fe_3(THT)_2(NH_4)_3$ 2D MOF film from 2-probe method 130
REFERENCES 132

SUMMARY 139

SAMENVATTING 142

ACKNOWLEDGEMENTS 146

OUTLINE

In this thesis we have employed time-resolved terahertz spectroscopy (TRST) for the interrogation of photo-induced charge carrier dynamics and charge transport in hybrid nanostructures. TRTS is an all-optical technique that enables probing the photoconductivity in a sub-picosecond resolution and without applying any physical contact. By applying this unique approach, we have gained substantial insight into the photo-induced charge transport properties in several nanostructured hybrid materials which are relevant for solar energy conversion; specifically we have analyzed interfacial electron transfer on graphene quantum dots sensitizing metal oxide nanoparticles and charge transport in novel 2D metal organic frameworks. Below I briefly summarize these research lines within the chapters that are contained in this thesis.

- **Chapter 1: Nanostructured hybrid materials for solar energy conversion**

  In this chapter, I introduce briefly the basics of operation of solar cells and solar fuel cells, specifically, regarding the fundamentals of interfacial charge transfer in dye-sensitized solar cells and the fundamentals of charge transport in metal organic frameworks (with potential application in photocatalytic water splitting cells).

- **Chapter 2: Time-Resolved Terahertz Spectroscopy**

  The main tool employed in this thesis, Time-resolved terahertz spectroscopy (TRTS), is introduced. Specifically, the experimental setup, the experimental methods as well as the methods of extracting the photoconductivity from TRTS measurements are explained. This chapter also includes a description for the conductivity models (Drude and Drude-Smith) employed throughout this thesis.

- **Chapter 3: Chemisorption of Atomically Precise 42-Carbon Graphene Quantum Dots on Metal Oxide Films Greatly Accelerates Interfacial Electron Transfer**

  Graphene quantum dots (GQDs) are emerging as environmentally friendly, low-cost and highly tunable building blocks in solar energy conversion architectures, such as solar (fuel) cells. Specifically, GQDs constitute a promising alternative for organometallic dyes in sensitized oxide

systems. Current sensitized solar cells employing atomically precise GQDs are based on physisorbed sensitizers, with typically limited efficiencies. Chemisorption has been pointed out as a solution to boost photoconversion efficiencies, by allowing improved control over sensitizer surface coverage and sensitizer-oxide coupling strength. In this chapter, employing time-resolved THz spectroscopy, we demonstrate that chemisorption of atomically precise C42-GQDs (hexa-peri-hexabenzocoronene derivatives consisting of 42 sp^2 carbon atoms) onto mesoporous metal oxides, enabled by their functionalization with a carboxylate group, enhances electron transfer (ET) rates by almost two orders of magnitude when compared with physisorbed sensitizers. Density functional theory (DFT) calculations, absorption spectroscopy and valence band X-ray photoelectron spectroscopy reveal that the enhanced ET rates can be traced to stronger donor-acceptor coupling strength enabled by chemisorption.

- **Chapter 4: Size-dependent electron transfer from atomically defined nanographenes to metal oxide nanoparticles**

  Atomically defined nanographenes (NGRs) feature finite size-dependent energy gaps induced by quantum confinement. Their energy-tunability and robustness make NGRs appealing candidates as active elements in sensitized geometries, where NGRs functionalize a large-area-to-volume ratio metal oxide (MO) film. Despite the prominent relevance of NGR/MO interfaces for developing novel solar energy conversion architectures, to date, little information is available regarding the fundamentals of electron transfer (ET) processes taking place from NGR donors to MO acceptors. Here, we analyze the interplay between the size of atomically precise NGRs and ET dynamics at NGR/MO interfaces. We observe that as the size of NGR decreases, ET between the NGR donating state and MO acceptor state speeds up. This dependence can be qualitatively understood from variations in the donor-to-acceptor interfacial overpotential as the NGR size (HOMO-LUMO gap) is reduced (increased), and can be quantified within the framework of Marcus ET theory.

- **Chapter 5: High-mobility band-like charge transport in a semiconducting two-dimensional metal–organic framework**

Metal-organic frameworks (MOFs) are hybrid materials based on crystalline coordination polymers consisting of metal ions connected by organic ligands. In addition to traditional applications in gas storage and separation or catalysis, the long-range crystalline order in MOFs, as well as the tunable coupling between organic and inorganic constituents, has led to the recent development of electrically conductive MOFs as a new generation of electronic materials. However, to date, the nature of charge transport in MOFs has remained elusive. In this chapter, we demonstrate, using high-frequency THz photoconductivity and Hall effect measurements, Drude-type band-like transport in a new semiconducting, π-d conjugated, porous $Fe_3(THT)_2(NH_4)_3$ (THT=2,3,6,7,10,11-triphenylenehexathiol) two-dimensional MOF, with a room temperature mobility up to ~220 cm^2/Vs. The temperature-dependent conductivity reveals that this mobility represents a lower limit for the material, as mobility is limited by impurity scattering. These results illustrate the potential for high-mobility semiconducting MOFs as active materials in thin film optoelectronic devices.

CHAPTER 1: NANOSTRUCTURED HYBRID MATERIALS FOR SOLAR ENERGY CONVERSION

1.1 Solar energy conversion

Over the last century, global energy demand has been increasing in line with population growth and social development. To date, most of the consumed energy is produced from fossil fuels. This approach of energy production has been directly linked to the emission of pollutants that do have a negative impact on global warming and climate change [1]. Thus, looking for environmentally friendly energy production schemes (renewable energy sources) has become a mandatory and urgent target for modern society. Among all renewable energy sources, solar energy has been identified as one of the cleanest energy sources that have the potential to both fulfill the increasingly high worldwide energy demand [2] and alleviate the detrimental effects of climate change. However, transitioning from a carbon-based to a solar-based economy requires the development of solutions capable of converting (and storing) solar energy at high efficiency/cost ratios. Therefore, the development of novel solar energy conversion technologies is nowadays of a huge practical significance. While efficiency is undoubtedly a pivotal parameter to take into account for the development of new technologies, pursuing high efficiency alone is not sufficient to allow technologies to transition from the lab to the market. Instead, high efficiency/cost ratios should be targeted. Improving efficiency/cost ratios for most emerging technologies is a big challenge, and this also applies to technologies that are currently available in the market. In this thesis, we have studied two novel hybrid systems that hold potential for being employed in the development of novel solar energy conversion schemes, specifically in solar cells and solar fuels architectures.

1.1.1 Photovoltaics (PV)

The historical development of photovoltaics (i.e. the direct conversion of light into electricity) has been classified into three generations [3]. First-generation solar cells generally refer to conventional semiconducting p-n junctions based on

crystalline silicon; a mature and market-dominant technology. While silicon solar cells have reached efficiencies close to their theoretical limit, they are yet - in most situations - rather expensive to economically compete with electricity production from fossil fuels. One of the main aspects resulting in the high cost of silicon PV is that solar cells based on this absorber are rather thick, an aspect closely connected with the indirect bandgap nature of this semiconducting material. To alleviate this problem, second-generation solar cells were introduced and developed with the aim of reducing cost from first-generation approaches. The main reduction of cost came from the employment of thin-film absorbers (direct bandgap materials) that can fully absorb, above its bandgap, all solar radiation impinging in the cell. In thinner cells, less material is needed and then lower production costs are achievable. In parallel, thin-film technologies are also expected to be capable to reduce costs by employing low-temperature processing methods in cell preparation and manufacturing (including as well the employment of cheap and flexible substrates enabling mass production in e.g. roll-to-roll processing). However, it is generally the case that lower temperatures of processing are linked with a higher density of defects in the samples, an aspect that has direct impact on device efficiency. Altogether, second-generation devices (like state-of-the-art CdTe and CIGS solar cells), while cheaper, display lower photoconversion efficiencies when compared with first-generation solar cells. Finally, third-generation solar cells refer to approaches that aim at producing ultrahigh efficiency (beyond the Shockley-Queisser (SQ) limit [4] as shown in Fig.1.1) at low cost. This is the ultimate goal in photovoltaics, as third-generation PV aims to get the best performing aspects of 1st and 2nd generation solar cells into a single device (i.e. high efficiency and low cost respectively).

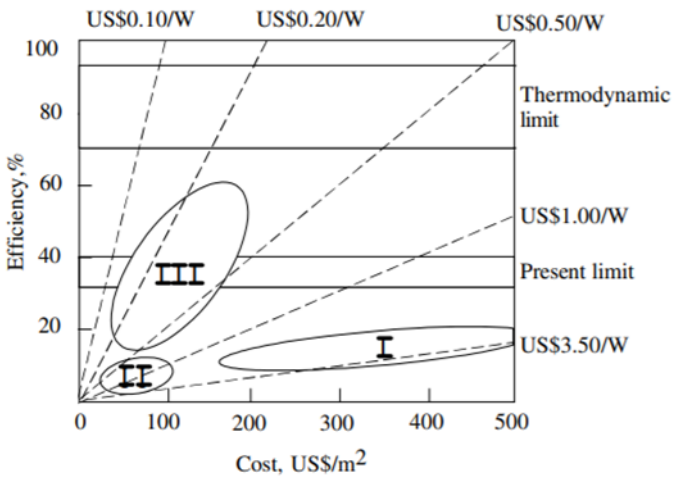

Figure 1.1. Efficiency vs cost per unit area for I, II and III generation solar cells. In addition, the figure shows two regimes representing the present limit (SQ limit) and thermodynamic limit (Carnot limit) respectively. Adapted from refs [5,6].

During the last two decades, researchers have introduced a plethora of novel solar cell geometries in order to reduce the costs in PV. For example, cells employing small organic molecules and polymers have been developed and are referred as organic-based solar cells. These cells, which can be embedded within 2nd generation approaches, aim at even reduced costs when compared with dominant market technologies (i.e. CdTe and CIGS). However, to date, the efficiency of these devices is much lower than those based on conventional inorganic semiconducting materials. In addition, it is still an ongoing challenge to assure the reliability of organic-based cells, which are generally prone to photodegradation of the organic constituents over time, a feature that strongly limit the lifetime of the devices. Alternatively, inorganic-organic hybrid materials have been also considered recently for thin-film solar cell development. A remarkable example in terms of efficiency refers to halide perovskites [7], a unique material that parallels the efficiencies of inorganic counterparts even when its production is made by solution-processing at room temperature (i.e. contradicting the rule of thumb that low energy input in the production of material is linked with low efficiency). However, the outstanding performance in terms of efficiency is shadowed by short term stability issues linked with these

cells. Prior to the emergence of the perovskites, and also framed within 2nd generation PV cells, other hybrid geometries were also considered for solar energy conversion. Notably dye- and quantum dot- sensitized oxide interfaces have been widely studied as building blocks for the schemes of solar cells and fuel cells. While these cells can be prepared at moderate temperatures, their efficiency is yet modest (almost half of that provided by CdTe, CIGS and perovskites). This poorer performance has been linked, to a large extent, to the intricate and complex chemistry of sensitizer-mesoporous oxide hybrid interfaces. Therefore it is still an ongoing challenge to develop hybrid schemes where tailorable interfaces are promoting rather than degrading the performance of novel solar energy conversion devices.

1.1.2 Photocatalytic water splitting

While the direct production of electricity from light in PV schemes can alleviate many of the challenges faced by society within this century, excess energy produced in PV has to be stored safely and reliably for long periods of time (and ideally without any losses). In this sense, an appealing approach refers to solar fuel cells where solar energy is stored – in principle for an unlimited time - in chemical bonds following photochemistry in a so-called catalyst. Among the different technologies that have been proposed, photocatalytic water splitting is an appealing approach. It deals with the production of molecular hydrogen and oxygen by decomposing water from sunlight. The appeal of the approach relies on the fact that water is abundant and environmentally friendly; storing energy in the form of molecular hydrogen is easily scalable and transportable, and might eventually provide a feedstock for the generation of other environmentally friendly fuels. Similarly to the case of solar cells, the ultimate goal in solar energy-to-hydrogen conversion is to produce hydrogen fuels from sunlight with high solar-to-hydrogen efficiency (STH) [8] at reduced costs.

In 1970s Honda and Fujishima [9] demonstrated that, irradiating titanium dioxide single crystals with light produced molecular hydrogen and oxygen stoichiometrically. A typical photoelectrochemical cell is shown in Fig.1.2(a). Here the photoanode is generally referred to as the photocatalyst. In Fig.1.2(b) is shown the kinetically relevant interfacial processes taking place in the devices. In brief, electron-hole pairs are generated when above-bandgap photons are absorbed by the photocatalyst. After that, photoinduced electrons and holes

trigger the reaction of photoreduction and photooxidation at cathode and anode respectively. In this manner, molecular hydrogen is produced by water splitting. The half-reactions undergoing on each electrode as well as the overall reaction for water splitting together with the change of free Gibbs energy, ΔG are given below [10]:

$$H_2O + 2(h^+) \rightarrow {}^1/_2\, O_2 + 2H^+ \qquad \text{(photooxidation)}$$

$$2H^+ + 2e^- \rightarrow H_2 \qquad \text{(photoreduction)}$$

$$H_2O \rightarrow {}^1/_2\, O_2 + H_2 \qquad \Delta G = +237.2\ \text{kJ/mol} \quad \text{(full reaction)}$$

The positive ΔG for water dissociation implies that the water-splitting process is, in essence, an uphill reaction that is thermodynamically unfavorable, i.e. an input of energy is required for the reaction to take place (e.g. light in photocatalysis). From a kinetic perspective, there are many competing processes against hydrogen generation, which are directly connected with efficiency losses. For example, the photoexcited electron-hole pairs can recombine through pathways in the semiconducting photocatalyst both radiatively and nonradiatively; this can happen in the bulk as well as at the interface as briefly summarized in Fig.1.2(b).

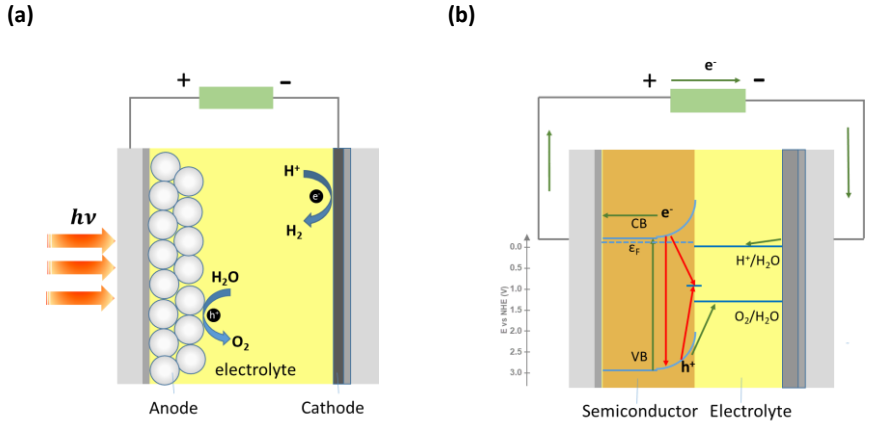

Figure 1.2. A water-splitting cell employing a semiconductor photocatalyst: (a) scheme of involved elements; (b) scheme for the band structure across the device and relevant interfacial kinetics, adapted from ref [10]. Green arrows refer to the kinetical processes that are favorable for the water-splitting process, while the red arrows represent recombination processes that are detrimental.

The nature of the employed semiconducting photocatalyst plays a central role in the overall STH efficiency of water splitting cells. To achieve high efficiency at low cost, multiple conditions need to be fulfilled by a given photocatalyst [11]: 1) a suitable bandgap usually close to near-infrared (NIR) region to harvest the maximum amount of light; 2) a suitable energy band alignment of the photocatalyst conduction band edge and valence band edge towards water redox potentials to efficiently drive the kinetic reactions (see Fig.1.2(b)); 3) a good stability in the presence of light as well as solution; 4) a low manufacturing cost and therefore suitability of mass production; 5) earth abundance and recyclability; and, finally 6) nontoxicity and environmental benignity. Obviously, it is non-trivial to find a candidate that fulfills all the above demands simultaneously. State-of-the-art photocatalysts are generally based on metal oxides which are robust in terms of stability during the photocatalytic process. However, the light-harvesting efficiency of most metal oxides is usually very low due to the poor absorption in the visible to NIR region of the solar spectrum. To bypass this handicap, strategies such as doping, and/or sensitizing the metal oxides with molecular dyes[12] and quantum dots[13] have been adopted. For the latter, the sensitizer (molecular dye or quantum dot), which is sensitive to VIS-NIR radiation, is placed onto the oxide. Following photon absorption in the sensitizer, photogenerated electrons can be transferred towards the oxide. These electrons are then able to produce the chemical reaction of interest at the surface of the oxide. Apart from the improved – and tailorable - sunlight photon absorption at sensitized interfaces, a large loading of sensitizers in the sample is critical (to boost optical density in the device). The main strategy that has been followed refers to having an oxide electrode consisting of nanoparticles (rather than a bulk crystal). Mesoporous films (consisting of interconnected metal oxide nanoparticles) provide larger surface-to-volume ratios and a correspondingly large surface area to be sensitized. Apart from the large area, an excellent electrical conductivity for the electrode is desired, so electrons in the e.g. metal oxide can travel to the location where a given chemical reaction takes place.

1.2 Nanographenes as sunlight absorbers in dye-sensitized solar cells

1.2.1 Dye-sensitized solar cells (DSSCs)

As briefly introduced before, sensitized solar cells represent a relatively new approach within second-generation photovoltaics. These thin-film solar cells can be prepared onto flexible substrates at moderate temperatures by solution processing. All these aspects have a positive effect on reducing manufacturing costs. While harvesting light with single crystal semiconducting metal oxides was initially interrogated by many researchers, it was quickly recognized that photoconversion efficiency was rather low [14,15] owing to the wide bandgap of most metal oxides. In order to make metal oxides sensitive to light absorption in the visible region of the electromagnetic spectrum, impurities were introduced in the samples, a type of defects that are able to extend the absorption response of the samples (but do also improve recombination in the electrodes). Later, a more flexible approach employed molecular dyes as external sensitizers. These molecular entities do have larger absorption cross-sections when compared with impurities, and when placed onto the oxide are capable to enhance charge collection in the oxide while not introducing undesired recombination pathways. They are also more versatile than impurities, e.g. their optoelectronic properties can be tuned for boosting the photoresponse of the dye/oxide system [16].

While sensitization by molecular dyes has proven very successful, initial approaches based on a planar oxide geometry were unable to produce large photocurrents in the oxides, owing to the low optical density induced by a single layer of molecular dyes onto the planar geometry. In 1991, Gratzel et. al. [17] introduced a novel geometry where photocurrent was truly boosted by employing a large-area-to-volume-ratio mesoporous oxide geometry. Thanks to the large surface of this geometry when compared to the planar one, the loading of photo-active sensitizers onto the oxide rocketed. The resulting dye-sensitized solar cells (DSSCs) based on mesoporous geometries demonstrated an overall efficiency of about 8% in initial devices (reaching figures up to 14% nowadays). This breakthrough triggered a brand new area of research with implications in photovoltaics and solar chemical fuel generation.

Figure 1.3(a) shows a sketch of a conventional n-type DSSC. The dye molecules are absorbed on the surface of a mesoporous semiconducting n-type metal oxide layer acting as a photoanode. The photoanode is sandwiched between a transparent conductive oxide window and the counter electrode. For common DSSCs, a liquid electrolyte is employed as a hole conductor which is in close contact with a counter electrode operating as a cathode. As illustrated in Figure 1.3(b), the working principle of this device is based on the following steps: 1)

photocarrier generation, where electron-hole pairs are generated by absorption of above-bandgap photons in the dye molecules; 2) interfacial exciton dissociation, where electrons (and holes) are injected from the donating (accepting) molecular state of the dye onto the accepting states of the metal oxide (and electrolyte), respectively; 3) charge carrier collection, where electrons are transported towards an external load through the metal oxide and holes are transported through the electrolyte respectively. The processes described above are kinetically competing with several recombination processes that are detrimental for device performance as illustrated in Fig 1.3(b). For example, for step 1 and 2, photo-generated electron-hole pairs can recombine radiatively within the dye; for step 3, back transfer of electrons populating the oxide conduction band towards the dye or the electrolyte are typical processes. Following this scheme, it is evident that it is critical to study and eventually control the kinetics at these hybrid interfaces to prevent detrimental relaxation paths and hence to boost the performance in devices.

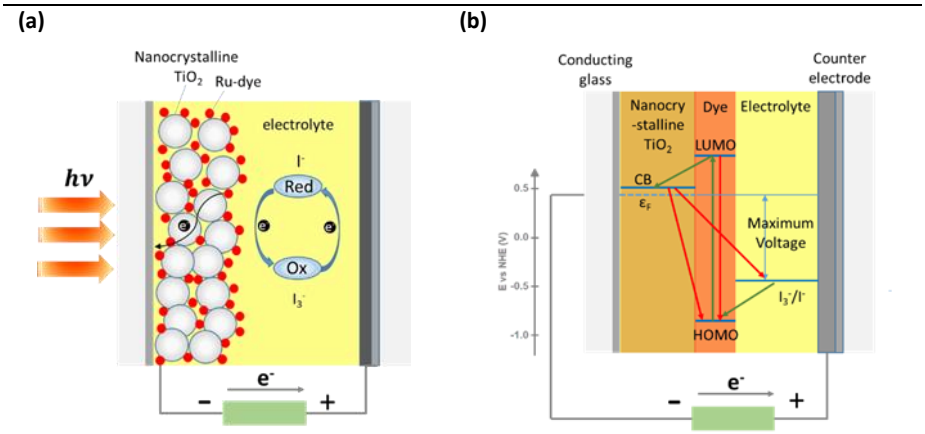

Figure 1.3. An n-type liquid-based dye-sensitized solar cell: (a) scheme revealing the main components and morphology; (b) energy band structure and related interfacial kinetics, adapted from ref [18]. In (b), the dashed line refers to the Fermi level (ε_F) of TiO_2. The solid blue lines marked with CB, LUMO, HOMO and I_3^-/I^- refer to the conduction band of TiO_2, the lowest unoccupied molecular orbital and the highest occupied molecular orbital of the dye molecule, and the redox potential of an iodide (I_3^-/I^-) electrolyte, respectively. The maximum voltage is determined by the difference between ε_F and $E_{I_3^-/I^-}$. The green arrows refer to favorable electron pathways, while red arrows illustrate detrimental pathways for photoconversion.

The key success of Graztel's cell, as stated above, relies to a large extent upon the use of a nanostructured photoanode. However, it is nontrivial to define the optimum geometry and chemistry of a given oxide employed as photoanode in a DSSC. For instance, a larger surface-area-to-volume ratio for a given electrode can be achieved by employing smaller oxide particles, which might enhance device´s overall efficiency via increased dye loading. However, it also imposes some detrimental effects for the device since the probability of recombination at interfaces increases as well with the electrode area. Furthermore, charge transport in the electrode is impeded by the presence of grain boundaries between nanoparticles, whose density is boosted when employing smaller-particle larger-area electrodes. From the latter, it is clear, that a trade-off based on kinetically competing factors does exist while optimizing an oxide electrode for DSSCs. Similar trade-offs based on kinetic competition at the interfaces are found as well while trying to optimize a given sensitizer. Obviously, there are many parameters inter-related that need to be taken into account, as such developing cost-effective DSSCs requires the design and integration of novel hybrid photoanodes with optimal control of the dye-oxide interfacial kinetics.

Many sensitizers have been developed for DSSCs [19], among them, organometallic dyes, such as Ru(II) polypyridyl dyes, are the most popular sensitizers thanks to their broad spectral light absorption (from ultraviolet to NIR region), relatively high molecular stability (when compared with other dyes), favorable interfacial dye/oxide energetics and linked interfacial kinetics. However, the relatively low molar extinction coefficients of Ru dyes (~10^4 $M^{-1}cm^{-1}$), as well as the high cost of ruthenium, motivated researchers to search for new sensitizers. As a promising substitute, several metal-free organic dyes that exhibit higher molar extinction coefficients (~10^5 M^{-1} cm^{-1}) while maintaining cost-effective synthetic methods were introduced. As a drawback, most dyes from this sub-class do have larger UV HOMO-LUMO gaps, which is detrimental towards efficient sunlight absorption. As an alternative to molecular dyes, colloidal inorganic quantum dots (CQDs) were introduced as efficient sensitizers. Several features are especially appealing when using CQDs as sensitizers, including, but not limited to, size/shape-tunable energy bandgaps, and much stronger – when compared with dyes – near optical bandgap absorption coefficients (~10^5 cm^{-1}). Currently, the highest efficiency reported on CQDs-sensitized solar cells [20] has paralleled those reported in state-of-the-art Ru-based DSSCs, approximately 14% for both approaches. As a drawback, most CQD based solar cells developed to

date are fabricated with scarce (and then expensive) and environmentally unfriendly elements, an aspect that compromises their future eventual implantation in the market.

1.2.2 Nanographenes in DSSCs

Nanographenes, often called graphene quantum dots (GQDs) and/or extended polycyclic aromatic hydrocarbons (PAHs), are fragments of graphene with finite sizes that exhibit quantum confinement effects [21]. These carbon-based metal-free sensitizers can be prepared with atomic precision, that allows fine control of its size/shape/edge morphology, all these aspects directly defining their optoelectronic properties [22]. All these unique features can be achieved following close-to-room-temperature synthesis by solvent chemistry [23] via "bottom-up" methods. Nanographenes show great potential in many applications, such as active or passive elements in optoelectronics as well as biomedical markers [24–26]. Specifically, for solar energy conversion, designed nanographenes can absorb light over the entire UV-VIS-NIR spectral region by simply tuning their size (i.e. energy gaps) [23]. In addition, they feature very high extinction coefficients [22,27], which hold the potential for developing thinner (and then cheaper) sensitized solar and fuel cell schemes. All these features were exploited for the first time in a sensitized geometry by Yan's group [28], where they employed solution processing methods to fabricate large (168 conjugated carbon atoms) and highly-soluble (separated by 3 peripheral alkyl chains from each molecule) PAHs as shown in Fig.1.4(a). The obtained PAHs revealed a broad absorption band in the visible region (centered at 591nm) with an extinction coefficient that is one order of magnitude higher than that of state-of-the-art ruthenium dyes. However, from the J-V characterization of solar cells made from these sensitizers (shown in Fig 1.4(b)), a moderate solar cell efficiency was inferred (way smaller than that obtained in ruthenium based dye-sensitized solar cells). Authors linked the poor performance with an ineffective sensitization for the employed TiO_2 mesoporous electrode. The functionalization of the electrode was based on physisorption for the employed PAH, an aspect that determines the sensitizer loading efficiency as well as the nature of the kinetics at the interface between PAH and metal oxide. In this thesis, we analyze the interplay between electron transfer dynamics and mode of PAH sensitization (physisorbed vs chemisorbed) on metal oxides by time-resolved terahertz spectroscopy.

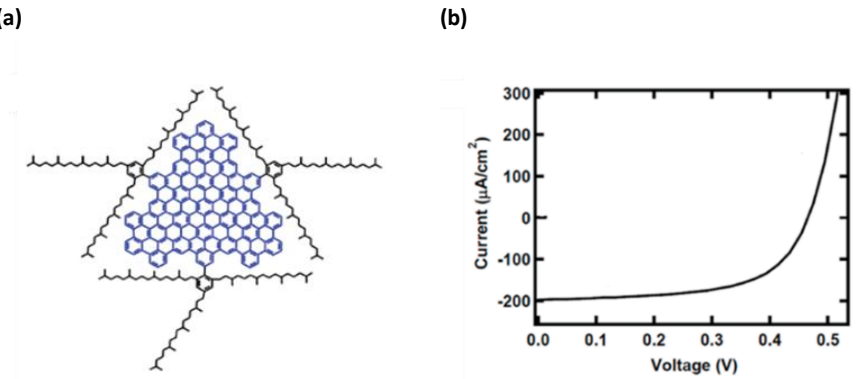

Figure 1.4. (a) Illustration of a GQD consisting of 168 conjugated carbon atoms; this molecule is highly-soluble due to the 3 peripheral alkyl chains; (b) J-V curves measured from a DSSC where C 168 GQDs are employed as sensitizers. Adapted from ref [28].

1.2.3 Photo-induced electron transfer at the sensitized interfaces

Electron transfer in donor (D) –acceptor (A) systems has been commonly described by the semiclassical rate expression provided by Marcus [29–32]:

$$k_{ET} = \frac{2\pi}{\hbar}\hat{H}(E)^2 \frac{1}{\sqrt{4\pi\lambda k_B T}} \exp[-\frac{(\Delta G_0 + \lambda)^2}{4\lambda k_B T}] \qquad \text{(Equation 1.1)}$$

Here, k_{ET}, $\hat{H}(E)$, ΔG_0 and λ represent the electron transfer (ET) rate constant from the reactant state (D^*-A) to the product state (D^+-A^-), the D-A coupling strength, the driving force for ET and the reorganizational energy, respectively. Eqn.1.1 reveals that k_{ET} depends on the interplay of multiple parameters which are often correlated.

A free-energy diagram between a donating and accepting state is shown in Fig.1.5(a). In this diagram, the variation of the free energy between a reactant and a product (R and P) as a function of the reaction coordinate is represented by two parabolas intersecting at the transition state, denoted as TS. The minima for both free energy surfaces, i.e. R^0 and P^0 refer to R and P in their equilibrium states. Within Marcus theory, ΔG_0 refers to the difference between the free energy of P^0 and that of R^0. Since the reaction is exothermic, ΔG_0 is negative. Moreover reaching TS from R^0 is determined by the activation energy barrier denoted as

ΔG^*, i.e. the difference between the free energy of TS and R^0 at a given temperature. Also shown in Fig.1.5(a) is λ which refers to the difference in free energy between R^0 and the point on the reactant parabola vertically above P^0. In this respect, λ can be interpreted as the free energy required to distort R^0 to R that possesses an equivalent reaction coordinate to P^0 without transferring the electron. Finally, $\widehat{H}(E)$ represents the wavefunction overlap between donor and acceptor state. k_{ET} is often plotted as a function of $-\Delta G_0$ on a semi-logarithmic scale as shown in Fig.1.5(b). By vertically shifting the P parabola with respect to R parabola, i.e. by keeping λ invariant while changing ΔG_0, we can define two distinct dependences of k_{ET} from Eqn.1.1, the normal region, when $-\Delta G_0 < \lambda$ (and k_{ET} grows with $-\Delta G_0$) and the inverted region, when $-\Delta G_0 > \lambda$ (and k_{ET} decreases with $-\Delta G_0$). When $-\Delta G_0 = \lambda$, the ET rate constant reaches its maximum [31].

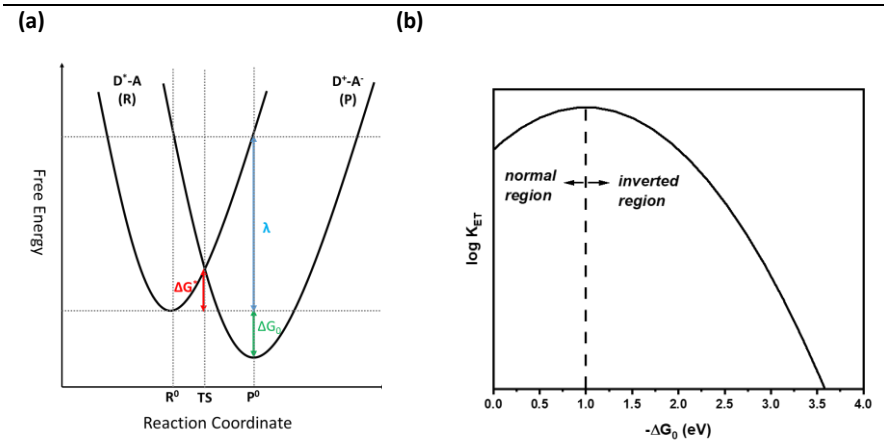

Figure 1.5. (a) Free energy surfaces of a discrete reactant state (D^*-A) and a discrete product state (D^+-A^-) as a function of reaction. R^0 and P^0 represent the reaction coordinate corresponding to the R and P in their equilibrium states; the transition state TS represents the reaction coordinate at which the two parabolas intersect, i.e. the transition state. $-\Delta G_0$, ΔG^* and λ refer to the ET driven force, activation energy barrier and reorganization energy respectively. Adapted from ref [31]. (b) variation of $\log(k_{ET})$ as a function of $-\Delta G_0$ predicted by Eqn.1.1. where $\widehat{H}(E) = 1meV, \lambda = 1eV$ and $T = 298K$.

When the acceptor state is a continuum rather than a discrete state, as in the case of the ET at the QD/MO interfaces, the many-state Marcus model is

commonly applied. In this case, Eqn.1.1 must be adapted by adding the effect of the continuum of states in the conduction band of MO [32–34]:

$$k_{ET} = \frac{2\pi}{\hbar}\int_{0}^{-\Delta G_0} dE\rho(E)\left|\hat{H}(E)\right|^2 \frac{1}{\sqrt{4\pi\lambda k_B T}}\exp[-\frac{(\lambda - \Delta G_0 + E)^2}{4\lambda k_B T}] \qquad \text{(Equation 1.2)}$$

where $\rho(E)$ refers to the density of accepting states located at energy E above the conduction band edge of MO. Within this picture, the integral implies that all states between $-\Delta G_0$ and the bottom of the CB are – in principle – able to accept the donated electron. The many-state Marcus model is employed in this thesis to model the interplay between k_{ET} and the size of PAHs in GQDs sensitized MO systems.

1.3 Metal organic frameworks

1.3.1 Overview

Metal organic frameworks (MOFs) are hybrid materials which are based on metal building blocks coordinating organic ligands. The metal-based components can be single metal ions, metal clusters or advanced secondary building units (SBUs) [35]. As an example, the unit cell of MOF-5 [36], i.e. $Zn_4O(BDC)_3$ (BDC=1,4-bezenedicarboxylate) illustrated in Fig.1.6(a), is made of eight zinc-based clusters coordinating orthogonal BDC linkers in a cubic porous geometry. This crystalline structure is characterized by an ultra-high surface area which is established by its long-range crystalline order. Beyond this particular example, and thanks to the recent development of reticular chemistry, the structure of a given MOF and then its porosity can be easily tuned by engineering each component, and/or by functionalizing the material with guest molecules using both in-situ and ex-situ synthetic approaches [37,38]. In addition, the permeability and reactivity of MOFs to certain guest molecules can be tailored. As such, MOFs represent a unique class of materials for a plethora of applications, among them as photoelectrode materials in solar energy conversion schemes.

Owing to their large and tunable porosity and then large surface-to-volume ratios, MOFs have been considered as ideal candidates for photocatalysis. As most of the MOFs developed to-date are insulating, in photocatalytic applications

MOFs are expected to catalyze the reaction at the place where photons are locally absorbed, i.e. where excitons are created. In this respect, MOFs employed as photocatalyst operate as a photo-active material participating in the photoreaction directly, or a passive material providing a scaffold acceptor for a sensitizer donor acting as photo-active material (resembling the operation of a sensitized geometry). Generally, three operating mechanisms have been proposed to explain charge carrier dynamics in MOF-based photoactive systems as illustrated in Fig.1.6(b): 1) charge carriers are generated in the photo-active organic linker followed by a transfer to the metal-based building blocks according to a "ligand-to-metal-transfer" process; 2) charge carriers are generated in-situ at the photocatalyst encapsulated in the pore of MOFs; or 3) a more intricate charge transfer process between the MOF and the catalyst located within the pore which is not necessarily photo-active [39]. Independently of the specific process involved, a general prerequisite for a MOF-based photocatalyst is a good electronic "communication" between the inorganic and organic part as well as the framework and the guest molecules. If this is appropriately tailored, it is possible to enable long-range transport in the samples (i.e. produce free carriers in the MOFs rather than excitons upon light absorption). Only recently, this has been achieved. Semiconducting MOFs with long-range charge transport have been developed. This is an appealing new feature for MOFs that offers an avenue for novel photocatalytic designs to be made from MOFs, e.g. for electrocatalysis. Conductive MOFs are also appealing for a plethora of novel applications including but not limited to optoelectronics and chemiresistive sensing [40–46].

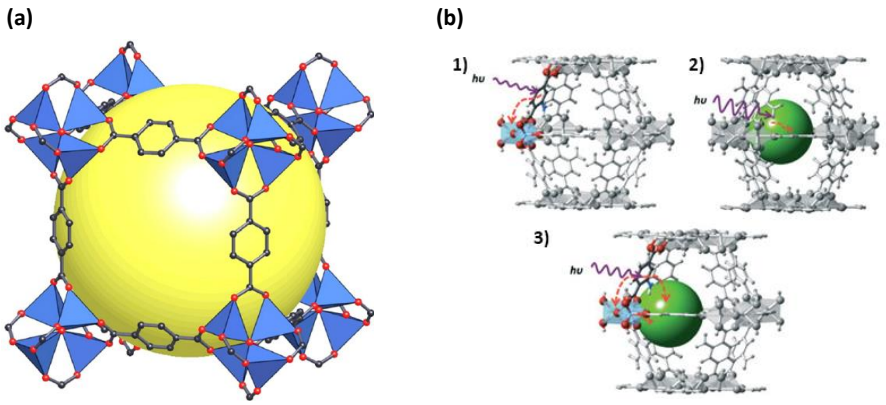

Figure 1.6. a) Unit cell of MOF-5, i.e. $Zn_4O(BDC)_3$ (BDC=1,4-bezenedicarboxylate). Adapted from ref [36]; b) three distinct mechanisms proposed for charge transfer in MOFs: 1) charge carriers are generated in the photo-active organic linker followed by a transfer to the metal-based building blocks according to the "ligand-to-metal-transfer" process; 2) charge carriers are generated in-situ at the photocatalyst encapsulated in the pore of MOFs; 3) charge transfer undergoes between the MOF and the encapsulated catalyst in the pore which is not necessarily photo-active. Adapted from ref [39].

Among the family of conductive MOFs, a relevant subclass family refers to two-dimensional (2D) π-conjugated MOFs. Materials in this family exhibit generally a honeycomb lattice structure, as defined by a square-planar coordination configuration determined by late-transition-metal ions linked by benzene-/triphenylene-derived planar ligands with *ortho*-di-substituted nitrogen, oxygen or sulfur atoms as donors. 2D π-conjugated MOFs have gained a broad interest due to their record electrical conductivities. However, to date, the nature of charge transport in MOFs is debated. Conductivity is generally scrutinized by contact and non-contact methods, and typically by temperature-dependent conductivity studies that can seed light into the nature of the mechanism which is operative (e.g. hopping or band-like transport). In the following section, the fundamentals of charge transport will be briefly introduced.

1.3.2 Charge transport in MOFs

a) Energy band models

As shown in Fig.1.7(a) solids can be classified, according to their conductive properties, as insulators, semiconductors, and metals. Generally speaking,

insulators and metals are poor and good conductors respectively, while semiconductors lie in between them in terms of resistance for current to flow.

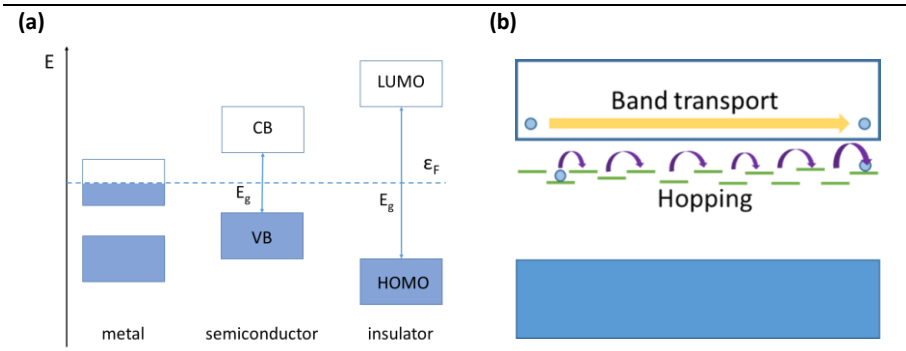

Figure 1.7. (a) Energy band diagram for an insulator, semiconductor, and metal: ε_F refers to the Fermi energy and E_g refers to the bandgap found in semiconductors and insulators; (b) Illustration depicting charge transport mechanisms (band transport and hopping transport). The pathways of charge transport for both mechanisms are indicated by the arrows.

As illustrated in Fig.1.7(a), metals are characterized by a band partially filled with electrons following Pauling's principle. Metals are characterized generally by a large density of electrons, usually linked to close-packed crystalline structures. In semiconductors, however, there is a forbidden energy region called the bandgap, E_g. A semiconductor will conduct similarly to metal only when electrons populate the upper band (conduction band), while the semiconductor will behave as an insulator if electrons are populating only the valence band. The number of electrons populating the conduction band can be tuned by an external perturbation (e.g. light) or by doping. Regarding doping, depending on whether the type of promoted majority carriers is electrons or holes, the material is called an n-type or p-type semiconductor respectively. Finally, insulators are characterized by an energy gap that is much larger than the one defining semiconductors (generally arbitrarily chosen around 3eV). Among other aspects, the large energy onset for the electrons to become conductive (to populate the conduction band) make these materials generally poor conductors.

b) Electrical conductance in the DC-limit

The DC electrical conductivity, defined as the inverse of resistivity, can be derived from Ohm's law:

$$J = \sigma_{DC} E \quad \text{(Equation 1.3)}$$

where σ_{DC} is the electrical conductivity in the DC-limit, and *J* and *E* refer to drift current density and electric field in the DC-limit, respectively. Since

$$J = \sigma_{DC} E \quad \text{(Equation 1.3)}$$

$$J = -env_d = -en(-\mu_{DC} E) = en\mu_{DC} E \quad \text{(Equation 1.4)}$$

we can derive the formula

$$\sigma_{DC} = en\mu_{DC} \quad \text{(Equation 1.5)}$$

where e, n, μ_{DC} represents the electron charge, density of free electrons, and the drift mobility of charges in the DC-limit respectively. From the definition of DC electrical conductivity, one can conclude that there are two pathways of enhancing the DC electrical conductivity in a given material. The first pathway is to increase the charge density by e.g. doping or photodoping [47]. The second pathway is to increase the charge mobility (e.g. by doping or by engineering materials where scattering mechanisms are largely suppressed). The definition of DC mobility is obtained by dividing the drift velocity of a charge carrier, $\boldsymbol{v}_d$ by the applied bias, as:

$$\mu_{DC} = -\frac{\boldsymbol{v}_d}{E} \quad \text{(Equation 1.6)}$$

which provides the following relationship:

$$\mu_{DC} = -\frac{\boldsymbol{e}\tau_S}{m^*} \quad \text{(Equation 1.7)}$$

where τ_S and m^* are the averaged scattering rate (the mean time interval between two scattering events for a free electron or hole) and the effective mass of the free charge carrier.

From Eqn.1.7, one can conclude that DC charge mobility can be improved by increasing τ_S and/or by reducing m^*. While m^* is generally constant for a given material, τ_S is a variable that depends on the nature and chemistry of the sample.

Generally speaking, τ_S is contributed by several scattering mechanisms impeding long-range charge motion, each of which is characterized by a $\tau_{S,i}$ within the Matthiessen's formalism [48]. Among the studied scattering mechanisms, the most relevant are often considered to be phonon scattering [49] and impurity scattering [50]. Normally phonon scattering dominates at high temperatures while impurity scattering is assumed to dominate in the low-temperature regime. As each scattering mechanism does have a specific dependence on temperature, temperature-dependent mobility studies are commonly employed to identify the nature of charge carrier scattering mechanisms limiting the mobility in the DC-limit.

Typically there are two charge transport mechanisms that can be found in (semi)conductors: band transport [51] and hopping [52] as illustrated in Fig.1.7(b). Band transport refers to charge carriers that are delocalized within a given band. This is a common observable in solid materials with highly ordered crystalline structures. Generally speaking, band-like transport is limited by electron-phonon scattering. As a result, reducing the temperature of a sample improves mobility (as the phonon population is decreased). On the other hand, if the disorder is large in a given sample, e.g. as often occurs in polycrystals, a hopping mechanism is generally operative. Hopping transport refers to charges that can only hop from one localized site to another by the assistance of temperature. Thus, solids dominated by hopping normally demonstrate a rather low DC charge mobility, which is even reduced at lower temperatures (i.e. hopping is a thermally activated process). Part of this thesis is focused on contributing to a better understanding of the nature of charge transport in 2D semiconducting MOFs.

References

(1) IEA webstore. Key World Energy Statistics 2018 https://webstore.iea.org/key-world-energy-statistics-2018 (accessed Oct 11, 2019).

(2) GEA Chapters - Chapters - IIASA https://www.iiasa.ac.at/web/home/research/Flagship-Projects/Global-Energy-Assessment/Chapters_Home.en.html (accessed Oct 11, 2019).

(3) Energy Agency, I. Technology Roadmap Solar Photovoltaic Energy - 2014 Edition.

(4) Shockley, W.; Queisser, H. J. Detailed Balance Limit of Efficiency of p-n Junction Solar Cells. J. Appl. Phys. 1961, 32 (3), 510–519.

(5) Conibeer, G. Third-Generation Photovoltaics. Mater. Today 2007, 10 (11), 42–50.

(6) Green, M. A. Third Generation Photovoltaics; Springer series in photonics; Springer Berlin Heidelberg, 2006; Vol. 12.

(7) Green, M. A.; Ho-Baillie, A.; Snaith, H. J. The Emergence of Perovskite Solar Cells. Nat. Photonics 2014, 8 (7), 506–514.

(8) Bolton, J. R. Solar Photoproduction of Hydrogen: A Review. Sol. Energy 1996, 57 (1), 37–50.

(9) Fujishima, A.; Honda, K. Electrochemical Photolysis of Water at a Semiconductor Electrode. Nature 1972, 238 (5358), 37–38.

(10) Walter, M. G.; Warren, E. L.; McKone, J. R.; Boettcher, S. W.; Mi, Q.; Santori, E. A.; Lewis, N. S. Solar Water Splitting Cells. Chem. Rev. 2010, 110 (11), 6446–6473.

(11) Acar, C.; Dincer, I.; Naterer, G. F. Review of Photocatalytic Water-Splitting Methods for Sustainable Hydrogen Production. Int. J. Energy Res. 2016, 40 (11), 1449–1473.

(12) Youngblood, W. J.; Anna Lee, S. H.; Maeda, K.; Mallouk, T. E. Visible Light Water Splitting Using Dye-Sensitized Oxide Semiconductors. Acc. Chem. Res. 2009, 42 (12), 1966–1973.

(13) Chen, H. M.; Chen, C. K.; Chang, Y.-C.; Tsai, C.-W.; Liu, R.-S.; Hu, S.-F.; Chang, W.-S.; Chen, K.-H. Quantum Dot Monolayer Sensitized ZnO Nanowire-Array Photoelectrodes: True Efficiency for Water Splitting. Angew. Chemie Int. Ed. 2010, 49 (34), 5966–5969.

(14) Ohnishi, T.; Nakato, Y.; Tsubomura, H. The Quantum Yield of Photolysis of Water on TiO_2 Electrodes. Berichte der Bunsengesellschaft für Phys. Chemie 1975, 79 (6), 523–525.

(15) Gerischer, H. Electrochemical Photo and Solar Cells Principles and Some Experiments. J. Electroanal. Chem. Interfacial Electrochem. 1975, 58 (1), 263–274.

(16) Tsubomura, H.; Matsumra, M.; Nomura, Y.; Amamiya, T. Dye Sensitised Zinc Oxide: Aqueous Electrolyte: Platinum Photocell. Nature 1976, 261 (5559), 402–403.

(17) O'Regan, B.; Grätzel, M. A Low-Cost, High-Efficiency Solar Cell Based on Dye-Sensitized Colloidal TiO2 Films. Nature 1991, 353 (6346), 737–740.

(18) Colodrero, S.; E., M.; Mguez, H. Photon Management in Dye Sensitized Solar Cells. In Solar Energy; InTech, 2010.

(19) Ye, M.; Wen, X.; Wang, M.; Iocozzia, J.; Zhang, N.; Lin, C.; Lin, Z. Recent Advances in Dye-Sensitized Solar Cells: From Photoanodes, Sensitizers and Electrolytes to Counter Electrodes. Mater. Today 2015, 18 (3), 155–162.

(20) Ling, X.; Zhou, S.; Yuan, J.; Shi, J.; Qian, Y.; Larson, B. W.; Zhao, Q.; Qin, C.; Li, F.; Shi, G.; et al. 14.1% $CsPbI_3$ Perovskite Quantum Dot Solar Cells via Cesium Cation Passivation. Adv. Energy Mater. 2019, 9 (28), 1900721.

(21) Bacon, M.; Bradley, S. J.; Nann, T. Graphene Quantum Dots. Part. Part. Syst. Charact. 2014, 31 (4), 415–428.

(22) Li, L. S.; Yan, X. Colloidal Graphene Quantum Dots. J. Phys. Chem. Lett. 2010, 1 (17), 2572–2576.

(23) Tian, P.; Tang, L.; Teng, K. S.; Lau, S. P. Graphene Quantum Dots from Chemistry to Applications. Mater. Today Chem. 2018, 10, 221–258.

(24) Shen, J.; Zhu, Y.; Yang, X.; Li, C. Graphene Quantum Dots: Emergent Nanolights for Bioimaging, Sensors, Catalysis and Photovoltaic Devices. Chem. Commun. 2012, 48 (31), 3686–3699.

(25) Jin, Z.; Owour, P.; Lei, S.; Ge, L. Graphene, Graphene Quantum Dots and Their Applications in Optoelectronics. Curr. Opin. Colloid Interface Sci. 2015, 20 (5–6), 439–453.

(26) Li, X.; Rui, M.; Song, J.; Shen, Z.; Zeng, H. Carbon and Graphene Quantum Dots for Optoelectronic and Energy Devices: A Review. Adv. Funct. Mater. 2015, 25 (31), 4929–4947.

(27) Li, L.; Wu, G.; Yang, G.; Peng, J.; Zhao, J.; Zhu, J.-J. Focusing on Luminescent Graphene Quantum Dots: Current Status and Future Perspectives. Nanoscale 2013, 5 (10), 4015.

(28) Yan, X.; Cui, X.; Li, B.; Li, L.-S. Large, Solution-Processable Graphene Quantum Dots as Light Absorbers for Photovoltaics. Nano Lett. 2010, 10 (5), 1869–1873.

(29) Barbara, P. F.; Meyer, T. J.; Ratner, M. A. Contemporary Issues in Electron Transfer Research. J. Phys. Chem. 1996, 100 (31), 13148–13168.

(30) Marcus, R. A.; Sutin, N. Electron Transfers in Chemistry and Biology. Biochim. Biophys. Acta - Rev. Bioenerg. 1985, 811 (3), 265–322.

(31) Archer, M. D.; Nozik, A. J. Nanostructured and Photoelectrochemical Systems for Solar Photon Conversion; Series on Photoconversion of Solar Energy; Published by Imperial College Press and distributed by World Scientific Publishing Co., 2008; Vol. 3.

(32) Asbury, J. B.; Hao, E.; Wang, Y.; Ghosh, H. N.; Lian, T. Ultrafast Electron Transfer Dynamics from Molecular Adsorbates to Semiconductor Nanocrystalline Thin Films. J. Phys. Chem. B 2001, 105 (20), 4545–4557.

(33) Tvrdy, K.; Frantsuzov, P. A.; Kamat, P. V. Photoinduced Electron Transfer from Semiconductor Quantum Dots to Metal Oxide Nanoparticles. Proc. Natl. Acad. Sci. 2011, 108 (1), 29–34.

(34) Tisdale, W. A.; Zhu, X.-Y. Artificial Atoms on Semiconductor Surfaces. Proc. Natl. Acad. Sci. 2011, 108 (3), 965–970.

(35) James, S. L. Metal-Organic Frameworks. Chem. Soc. Rev. 2003, 32 (5), 276.

(36) Rosi, N. L. Hydrogen Storage in Microporous Metal-Organic Frameworks. Science (80-.). 2003, 300 (5622), 1127–1129.

(37) Yaghi, O. M.; O'Keeffe, M.; Ockwig, N. W.; Chae, H. K.; Eddaoudi, M.; Kim, J. Reticular Synthesis and the Design of New Materials. Nature 2003, 423 (6941), 705–714.

(38) Furukawa, H.; Cordova, K. E.; O'Keeffe, M.; Yaghi, O. M. The Chemistry and Applications of Metal-Organic Frameworks. Science (80-.). 2013, 341 (6149), 1230444–1230444.

(39) Nasalevich, M. A.; van der Veen, M.; Kapteijn, F.; Gascon, J. Metal–Organic Frameworks as Heterogeneous Photocatalysts: Advantages and Challenges. CrystEngComm 2014, 16 (23), 4919–4926.

(40) Wang, J.-L.; Wang, C.; Lin, W. Metal−Organic Frameworks for Light Harvesting and Photocatalysis. ACS Catal 2012, 2, 25.

(41) Hendon, C. H.; Rieth, A. J.; Korzyński, M. D.; Dincă, M. Grand Challenges and Future Opportunities for Metal–Organic Frameworks. ACS Cent. Sci. 2017, 3 (6), 554–563.

(42) Wang, S.; Wang, X. Multifunctional Metal-Organic Frameworks for Photocatalysis. Small 2015, 11 (26), 3097–3112.

(43) Bon, V. Metal-Organic Frameworks for Energy-Related Applications. Curr. Opin. Green Sustain. Chem. 2017, 4 (1), 44–49.

(44) Zhang, H.; Nai, J.; Yu, L.; Lou, X. W. (David). Metal-Organic-Framework-Based Materials as Platforms for Renewable Energy and Environmental Applications. Joule 2017, 1 (1), 77–107.

(45) Stavila, V.; Talin, A. A.; Allendorf, M. D. MOF-Based Electronic and Opto-Electronic Devices. Chem. Soc. Rev. Chem. Soc. Rev 2014, 5994 (43), 5994–6010.

(46) Li, S. L.; Xu, Q. Metal-Organic Frameworks as Platforms for Clean Energy. Energy Environ. Sci. 2013, 6 (6), 1656–1683.

(47) Karl, N. Charge Carrier Transport in Organic Semiconductors. Synth. Met. 2003, 133–134, 649–657.

(48) Matthiessen, A.; Vogt, C. Ueber Den Einfluss Der Temperatur Auf Die Elektrische Leitungsfähigkeit Der Legirungen. Ann. der Phys. und Chemie 1864, 198 (5), 19–78.

(49) Holland, M. G. Phonon Scattering in Semiconductors From Thermal Conductivity Studies. Phys. Rev. 1964, 134 (2A), A471–A480.

(50) Conwell, E.; Weisskopf, V. F. Theory of Impurity Scattering in Semiconductors. Phys. Rev. 1950, 77 (3), 388–390.

(51) Glaeser, R. M.; Berry, R. S. Mobilities of Electrons and Holes in Organic Molecular Solids. Comparison of Band and Hopping Models. J. Chem. Phys. 1966, 44 (10), 3797–3810.

(52) Scher, H.; Lax, M. Stochastic Transport in a Disordered Solid. I. Theory. Phys. Rev. B 1973, 7 (10), 4491–4502.

CHAPTER 2: TIME-RESOLVED TERAHERTZ SPECTROSCOPY

2.1 Overview

Terahertz (THz) frequencies (0.1-10 THz or 3-300 cm^{-1}) lie between the infrared and the microwave spectral regions of the electromagnetic spectrum. Several particles and quasi-particles show a unique fingerprint response in the THz frequency regime, an aspect that allows for their characterization and modeling. In particular, the THz frequency range is specifically sensitive to free carrier motion, as such, charge carrier transport can be analyzed optically by THz spectroscopy. Charge carrier-scattering interaction, with e.g. phonons or impurities, often occurs in the timescale of picoseconds (that is, at THz frequencies [1]). Therefore detailed information about scattering processes (which determine charge carrier mobility) taking place in semi-conductors can be adequately characterized by their spectroscopic signatures in the THz spectral region.

Time-resolved THz spectroscopy (TRTS) is an ultrafast laser-based technique where the material of interest is first excited above its bandgap by a light pulse and then probed with a THz pulse in either transmission or reflection mode. Following this scheme, TRTS allows characterizing the non-equilibrium charge carrier dynamics of a given sample following a pump-probe scheme (i.e. optical-pump THz-probe spectroscopy or OPTP). The THz probe is essentially a freely propagating single pulse containing a bandwidth limited to few THz (the bandwidth is actually determined by the specific generation and detection schemes employed in a given setup, typically ~2 THz in our system). One of the biggest advantages of the TRTS technique, when compared with other pump-probe schemes, relies on the fact that the electric field of the THz probe pulse can be recorded in the time domain [2] (see Fig.2.1(a)), and as such, in a typical experiment, we can obtain information not only about changes in the amplitude of the THz probe (see Fig.2.1(b)) but also about changes in its phase, an aspect that allows retrieving the complex optical properties of a material.

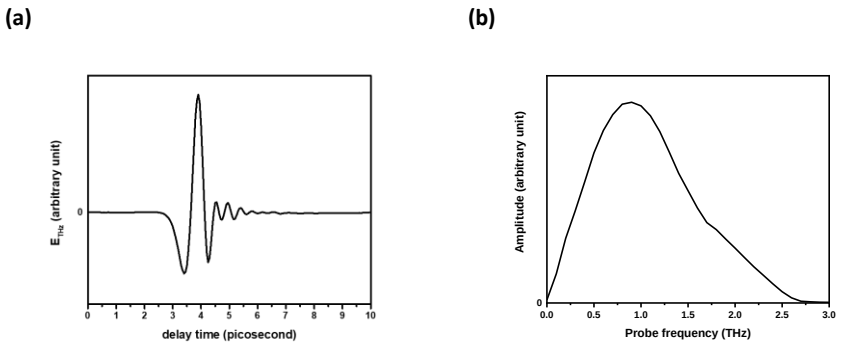

Figure 2.1. (a) Electric field E_{THz} of a freely propagating THz pulse in the time domain; (b) the frequency-resolved THz amplitude provided by (a) following a Fourier transform operation.

2.2 Experimental setup

Fig.2.2 shows a schematic of the experimental setup for TRTS measurements employed in this thesis. The setup is driven by a Ti: Sapphire mode-locked laser with an output pulse duration of 40 fs which is centered at 800 nm wavelength.

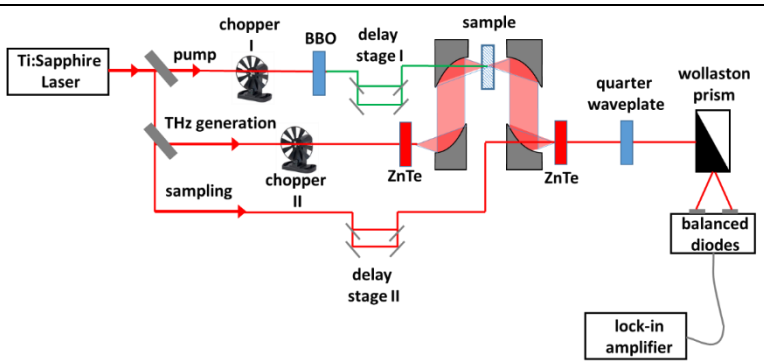

Figure 2.2. Experimental setup for TRTS measurement employed in this thesis. Pump, THz generation and sampling beams are all driven by the Ti: Sapphire laser.

In our setup, the laser output from the Ti:Sapphire laser is separated into three beams: two are employed to generate and detect THz pulses, and another one is used to optically excite a sample (acting as a pump). We will refer to them as the pump beam, THz generation beam, and sampling beam respectively as illustrated

in Fig.2.2. The frequency of the pump beam can be modulated by e.g. using a beta-barium-borate (BBO) crystal (which is capable of doubling the wavelength output of the Ti:Sapphire laser, from 800 to 400nm). A motorized delay stage is employed to control the pump-probe delay time, i.e. the arriving time of pump beam relative to that of the THz probe beam. In this manner, one can acquire the transient THz response of photo-excited samples as a function of time after excitation.

For THz generation, optical rectification is employed in our setup. In simple terms, the THz pulse is generated in a (110) ZnTe crystal and this emission is collected by a pair of parabolic mirrors that allow the probe to be focused onto the sample of interest. After this, the THz probe is transmitted through the sample and collected through another pair of parabolic mirrors, that are employed as well to focus the transmitted beam, but now onto a detection crystal (also a (110) ZnTe crystal in our system). For detection, our setup employs a scheme based on electro-optic (EO) sampling. The THz pulse impinging onto the detection crystal induces birefringence in the non-centrosymmetric (110) ZnTe material. This change can be traced by the sampling beam, that is, by changes of the polarization of a sampling beam that impinges the detection crystal with an initial (prior excitation) circular polarization. Following this scheme, the THz field can be characterized by means of the sampling beam by measuring separately the orthogonal polarization components of it. This is achieved by a differential detector (with 2 silicon-based photodiodes) that monitor both polarization components simultaneously. The polarization components can be easily separated by a Wollaston prism prior to reaching the detector as shown in Fig.2.2. When there is no THz light impinging the ZnTe crystal, the sampling beam keeps a circular polarization and a differential null signal is collected in the detector. When the THz pulse is present in the detection crystal, a change in polarization of the sampling beam is monitored differentially (light becomes elliptically polarized). This allows retrieving the field strength of the THz pulse as a function of time delay (Fig.2.1(a)) by the sampling delay time (optical delay stage II illustrated in Fig.2.2).

The output signal from the differential detector is monitored via a lock-in amplifier operating at a given frequency (fixed by a mechanical chopper spinning at 500Hz). As illustrated in Fig.2.2, chopper I is used to record THz signals while chopper II is used to record the photo-induced changes in the THz probe for pump-probe measurements. Since the frequency range of the THz pulse

generated in our setup coincides with the vibrational modes of water vapor [3], the entire setup is enclosed and protected by a dry nitrogen environment during the measurements.

In principle, two types of experiments can be performed using the TRTS experimental setup described above: THz time-domain spectroscopy (THz-TDS) and Optical-pump THz-Probe spectroscopy (OPTP). Each experiment enables respectively a study of THz response of a sample in equilibrium (without optical excitation) and out of equilibrium (with optical pump excitation). Since OPTP measurements have been primarily conducted within this thesis, I do introduce below the specifics of this approach alone.

2.3 Optical-Pump Terahertz-Probe Spectroscopy

Optical-Pump THz-Probe spectroscopy (OPTP) is a powerful tool of acquiring the temporal evolution of the photoconductivity of a given sample after pump excitation via a pump-probe scheme with a sub-ps resolution and optically. In this experiment, an optical pump pulse excites charge carriers in the sample and the THz pulse probes the light-induced modulation of the transmitted THz signal in the time domain. Using this approach, we can obtain the photoconductivity of the sample as a function of time after excitation. The time-dependent photoconductivity reflects the time evolution of the product of mobility and carrier density. As such, if the mobility does not change with time, OPTP provides the dynamics of the carrier density following photoexcitation. Provided that we are recording the THz pulses at any pump-probe delay, we can as well infer the frequency-resolved complex conductivity of the samples in OPTP experiments. I refer to these two operation modes as 1D spectroscopy and 2D spectroscopy, respectively.

1D spectroscopy refers to the measurement of carrier dynamics ($Re(\sigma)(t) = q\mu N(t)$) in a given sample following photo-excitation. In order to realize this scheme, the delay stage II is set at a position where the sampling pulse samples the maximum electric field of the THz pulse in the time domain (Fig.2.2). The evolution of the electric field strength, after pump excitation, is monitored over time by moving delay stage I. This simple layout allows obtaining the evolution of carrier density over time ($N(t)$) in a sample, from which the lifetime of charge carriers can be inferred.

Note that 1D spectroscopy does not provide any frequency-resolved spectral information. To obtain spectral information at any given pump-probe delay, we do 2D spectroscopy that simply refers to the characterization of the full time trace of transmitted THz pulse at each t_{pump}, which is accomplished by keeping pump delay fixed and scanning temporally the THz pulse by the sampling delay (see Fig.2.2). This measurement enables the extraction of both the real and imaginary parts of the photoconductivity spectrum at a specific time after excitation (selected by the pump delay stage).

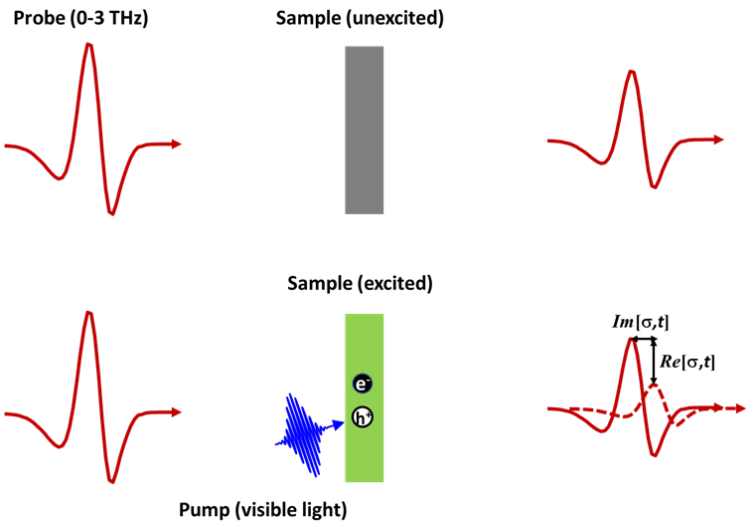

Figure 2.3. Scheme of a typical OPTP experiment. When the sample is unexcited (upper panel), the THz waveform propagating the sample is recorded in the time domain. Afterward, the sample is excited by a visible pump pulse (lower panel) to generate electron and hole pairs and subsequently probed by the THz pulse. The real and imaginary part of the photoconductivity can be retrieved from this data from the photo-induced changes in amplitude and phase of the transmitted THz waveform.

2.4 Extracting photoconductivity

As described above, OPTP measurements enable measuring the THz waveform in the time domain with and without photo-excitation of the sample. By Fourier transforming the time domain data, we can infer the complex refractive index of a

sample, $\tilde{n}(\omega) = n(\omega) + ik(\omega)$. Since the complex refractive index, complex dielectric constant $\tilde{\epsilon}(\omega)$ and complex conductivity $\tilde{\sigma}(\omega)$ are correlated [4] all of them can be inferred from the experiment:

$$\tilde{\epsilon}(\omega) = [\tilde{n}(\omega)]^2, \qquad \tilde{\sigma}(\omega) = -i\tilde{\epsilon}(\omega)\epsilon_0\omega = -i[\tilde{n}(\omega)]^2\epsilon_0\omega \qquad \text{(Equation 2.1)}$$

above ϵ_0 refers to the vacuum permittivity. In this thesis, we have been primarily interested in the complex photoconductivity $\tilde{\sigma}_{ph}(\omega)$, i.e. the change in conductivity of a given sample after photoexcitation.

Obtaining $\tilde{\sigma}_{ph}(\omega)$ from an OPTP experiment, requires some prior knowledge about the pump excitation profile. Listed in Fig.2.4 are three possible scenarios concerning this aspect, where pump profile excitation are accounted for by taking into account sample thickness d and the optical penetration depth l_p of the pump pulse. In the following context, we will first describe the methodology of extracting photoconductivity from scenario (a). Following that, methodologies regarding the other two scenarios will be discussed briefly.

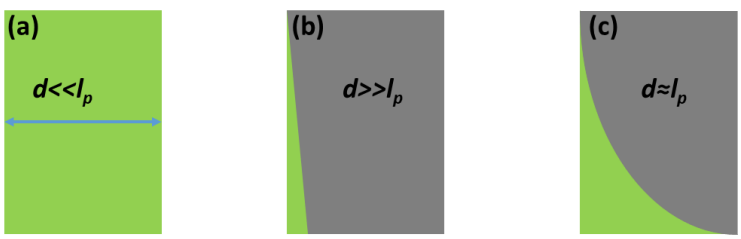

Figure 2.4. Different optical excitation pump profiles that can be obtained in an OPTP experiment. Based on the ratio between sample thickness d and the optical penetration depth l_p of the pump pulse, three excitation scenarios can be expected: (a) homogeneous excitation ($d \ll l_p$); (b) thin slab-like excitation close to the surface ($d \gg l_p$); (c) intermediate case where excitation is not uniform in the sample ($d \approx l_p$).

Represented in Fig.2.5 is a typical sample configuration while assuming (a) photoexcitation scenario (where $d \ll l_p$).

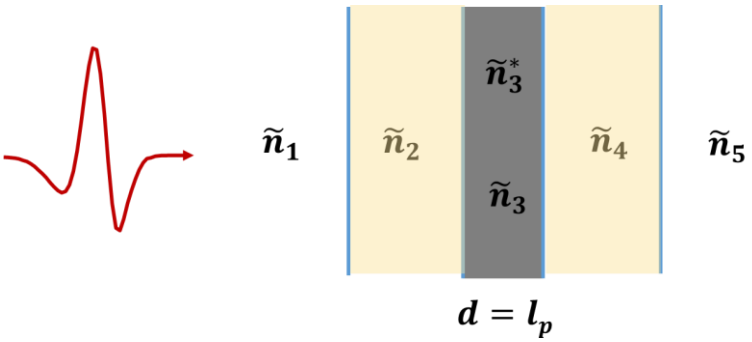

Figure 2.5. Layout of the sample for extracting photoconductivity in a typical OPTP measurement where the excitation scenario shown in Fig. 2.4(a) is applicable. The red pulse represents the THz waveform with frequency-dependent electric field $\vec{E}(\omega)$. It propagates through medium from 1 to 5 where medium 3 represents the photosensitive sample. $\tilde{n}_j$ refers to the complex refractive index $\tilde{n}$ in jth medium (j = 1 to 5). The asterisk represents the medium with photo-excitation. d refers to the thickness, i.e. optical excitation length of the medium of interest in this scenario.

Prior to any pump excitation of the sample, the transmitted THz waveform pulse with frequency-dependent electric field $\vec{E}(\omega)$ propagates through each medium j with a complex refractive index $\tilde{n}_j$, where j increases from 1 to 5 in this case. l_j is defined as the optical length of jth medium, and $t_{j-1,j}$, $t_{j,j+1}$, $r_{j-1,j}$, $r_{j,j+1}$ represent the Fresnel transmission and reflection coefficients at the interface before and after contacting the jth medium (j from 2 to 4) respectively. By taking into account the multiple reflections taking place at each phase, the THz waveform after propagating through the jth medium, $\vec{E}_{j+1}(\omega)$ can be expressed as [5,6]:

$$\vec{E}_{j+1}(\omega) = \frac{\vec{E}_{j-1}(\omega) * t_{j-1,j} * e^{\frac{i\tilde{n}_j\omega l_j}{c}} * t_{j,j+1}}{1 + r_{j-1,j} * e^{\frac{2i\tilde{n}_j\omega l_j}{c}} * r_{j,j+1}} \qquad \text{(Equation 2.2)}$$

Where $t_{j,j+1} = \frac{2\tilde{n}_j}{\tilde{n}_j+\tilde{n}_{j+1}}$, $r_{j,j+1} = \frac{\tilde{n}_{j+1}-\tilde{n}_j}{\tilde{n}_{j+1}+\tilde{n}_j}$.

For a typical OPTP measurement following Fig.2.5, the sample film is sandwiched by two fused silica windows and surrounded by dry nitrogen.

Denoting the initial electric field as $\vec{E}_0(\omega)$, the THz waveform transmitted through the unexcited sample film can be then determined as:

$$\vec{E}_{sample}^{unexcited}(\omega) = \frac{\vec{E}_0(\omega) * t_{1,2} * e^{\frac{i\tilde{n}_2\omega l_2}{c}} * t_{2,3} * e^{\frac{i\tilde{n}_3\omega l_3}{c}} t_{3,4} * e^{\frac{i\tilde{n}_4\omega l_4}{c}} * t_{4,5}}{1 + r_{2,3} * e^{\frac{2i\tilde{n}_3\omega l_3}{c}} * r_{3,4}}$$

(Equation 2.3)

Here only multiple reflections in the sample, i.e. 3rd medium, are considered.

After the pump beam reaches the sample, a similar analysis can be made, where the THz waveform transmitted through the sample film under photoexcitation reads:

$$\vec{E}_{sample}^{excited}(\omega) = \frac{\vec{E}_0(\omega) * t_{1,2} * e^{\frac{i\tilde{n}_2\omega l_2}{c}} * t_{2,3} * e^{\frac{i\tilde{n}_3^*\omega l_3}{c}} t_{3,4} * e^{\frac{i\tilde{n}_4\omega l_4}{c}} * t_{4,5}}{1 + r_{2,3} * e^{\frac{2i\tilde{n}_3^*\omega l_3}{c}} * r_{3,4}}$$

(Equation 2.4)

The asterisks in this equation denote the indexes of refraction when the sample has been photoexcited. By dividing Eqn.2.4 by Eqn.2.3, we obtain:

$$\frac{\vec{E}_{sample}^{excited}(\omega)}{\vec{E}_{sample}^{unexcited}(\omega)} = \frac{t_{2,3}^* * t_{3,4}^*}{t_{2,3} * t_{3,4}} * \frac{1 + r_{2,3} * e^{\frac{2i\tilde{n}_3\omega l_3}{c}} * r_{3,4}}{1 + r_{2,3}^* * e^{\frac{2i\tilde{n}_3^*\omega l_3}{c}} * r_{3,4}^*} * e^{\frac{i(\tilde{n}_3^* - \tilde{n}_3)\omega l_3}{c}}$$

(Equation 2.5)

Assuming that multiple reflections induced by photoexcitation in the sample are negligible, allows Eqn. 2.5 to be simplified to the form:

$$\frac{\vec{E}_{sample}^{excited}(\omega)}{\vec{E}_{sample}^{unexcited}(\omega)} = \frac{t_{2,3}^* * t_{3,4}^*}{t_{2,3} * t_{3,4}} * e^{\frac{i(\tilde{n}_3^* - \tilde{n}_3)\omega l_3}{c}}$$

(Equation 2.6)

In OPTP measurements, the THz waveform is recorded prior and after photoexcitation in the time-domain as $\vec{E}_{sample}^{\prime unexcited}(t)$ and $\Delta\vec{E}_{sample}^{\prime}(t) \equiv \vec{E}_{sample}^{\prime excited}(t) - \vec{E}_{sample}^{\prime unexcited}(t)$. Then the frequency-dependent terms, $\vec{E}_{sample}^{\prime unexcited}(\omega)$ as well as $\Delta\vec{E}_{sample}^{\prime}(\omega)$ can be obtained as:

$$\frac{\Delta\vec{E}'_{sample}(\omega)}{\vec{E}'^{unexcited}_{sample}(\omega)} = \frac{\vec{E}'^{excited}_{sample}(\omega) - \vec{E}'^{unexcited}_{sample}(\omega)}{\vec{E}'^{unexcited}_{sample}(\omega)} = \frac{\vec{E}'^{excited}_{sample}(\omega)}{\vec{E}'^{unexcited}_{sample}(\omega)} - 1$$

(Equation 2.7)

The photo-induced change of the complex refractive index of the sample, $\Delta\tilde{n}_3 = \tilde{n}_3^* - \tilde{n}_3$ and hence $\tilde{\sigma}_{ph}(\omega)$ can be then determined by solving the following equation:

$$\frac{\Delta\vec{E}'_{sample}(\omega)}{\vec{E}'^{unexcited}_{sample}(\omega)} + 1 = \frac{t^*_{2,3} * t^*_{3,4}}{t_{2,3} * t_{3,4}} * e^{\frac{i\Delta\tilde{n}_3\omega l_3}{c}}$$

(Equation 2.8)

For scenario (b) where $d \gg l_p$, only a thin slab of sample close to the surface is excited by the pump. Here an analytical method of extracting $\tilde{\sigma}_{ph}(\omega)$ can be applied. If the modulation of the THz probe by the photoexcitation of the sample is sufficiently small, the thin-film approximation [7] applies, and then $\tilde{\sigma}_{ph}(\omega)$ can be inferred as :

$$\tilde{\sigma}_{ph}(\omega) = -\frac{n+1}{Z_0 * l_p}\left[\frac{\Delta\vec{E}'_{sample}(\omega)}{\vec{E}'^{unexcited}_{sample}(\omega)}\right]$$

(Equation 2.9)

Where *n* and 1 refer to the refractive index of the unexcited part of the sample and air and Z_0 is a constant (377 Ω) that represents the impedance of free space.

When the excitation scenario is intermediate between those described above, as illustrated in Fig.2.4(c), that is when $d \approx l_p$, an exponential decay of the excitation density along the THz propagation direction must be taken into account. Under these circumstances, a tedious numerical analysis where the sample is treated as the sum of homogenously photoexcited slabs must be applied [8]. In order to avoid these complications, either d or l_p can often be chosen so that the sample photoexcitation scenario fulfills scenario (a) or (b) in Fig.2.4.

2.5 Conductivity models

The retrieved $\tilde{\sigma}_{ph}(\omega)$ from THz spectroscopy allows us to infer the two relevant parameters defining the conductivity, i.e. the carrier density and mobility

of a given sample. In order to do so, the frequency-resolved conductivity found in the sample at a given pump-probe delay can be inferred and modeled according to the nature of the sample. In this subsection, I will introduce two of the most common models employed when modeling the response in semiconductors: the Drude and Drude-Smith models.

2.5.1 Drude model

Drude model is based on the classical kinetic theory of gases where an electron-hole plasma is treated as a non-interacting electron gas. Therefore the major assumptions of the classical kinetic theory of gases are also applied to the Drude model: (1) free-electron approximation, i.e. electron interacts with the lattice only through randomizing scattering events; (2) independent electron approximation, i.e. electron-electron interactions are neglected; (3) electron collides with the nuclei of atoms in a mean free time τ_S independent of electron's position and velocity. Given these assumptions, the averaged trajectories of an ensemble of charge carriers in a time-dependent electric field $\vec{E}(t)$ is represented by the following equation of motion:

$$m^* \frac{d^2\langle \vec{r} \rangle}{dt^2} + m^* \gamma \frac{d\langle \vec{r} \rangle}{dt} = -e\vec{E}(t) \qquad \text{(Equation 2.10)}$$

where $\langle \vec{r} \rangle$ is the center of mass position of the electron gas, γ is the scattering rate which is the inverse of τ_S. e is the electronic charge and m^* is the effective mass of the free charge carrier. We can define the drift velocity $\vec{v}_d(t) = \frac{d\langle \vec{r} \rangle}{dt}$. Therefore Eqn.2.10 can be rewritten as:

$$m^* \frac{d}{dt}\vec{v}_d(t) + m^* \frac{1}{\tau_S}\vec{v}_d(t) = -e\vec{E}(t) \qquad \text{(Equation 2.11)}$$

where γ is defined by $\frac{1}{\tau_S}$. For an oscillating electric field at angular frequency ω, $\vec{E}(t) = \vec{E}_0 e^{-i\omega t}$, the above equation has the solution:

$$\vec{v}_d(t) = -\frac{e\tau_S}{m^*}\frac{1}{1 - i\omega\tau_S}\vec{E}_0 e^{-i\omega t} \qquad \text{(Equation 2.12)}$$

The AC mobility $\tilde{\mu}(\omega)$ can be deduced as:

$$\tilde{\mu}(\omega) = \frac{\vec{v}_d(t)}{\vec{E}(t)} = -\frac{e\tau_S}{m^*}\frac{1}{1 - i\omega\tau_S} \quad \text{(Equation 2.13)}$$

As such, the AC Drude conductivity can be expressed as

$$\tilde{\sigma}_{Drude}(\omega) = (-e)N\tilde{\mu}(\omega) = \frac{e^2 N\tau_S}{m^*}\frac{1}{1 - i\omega\tau_S} = \sigma_{D,DC}\frac{1}{1 - i\omega\tau_S} \quad \text{(Equation 2.14)}$$

where $\sigma_{D,DC}$ is the DC Drude conductivity and N is the carrier density. This formula allows us to obtain the scattering rate (τ_S) and (photo)doping of a sample (N). From τ_S, the mean free path of electrons l_{mfp}, i.e. the length traveled by the electron at the interval of collisions can be as well inferred from:

$$l_{mfp} = \tau_S\langle v_{th}\rangle \quad \text{(Equation 2.15)}$$

where v_{th} is the thermal velocity that from the Maxwell-Boltzmann distribution takes the form $v_{th} = \sqrt{3k_BT/m_0}$, where m_0 is the electron rest mass [9].

From the Drude model, if m^* is known, both $\mu_{D,DC}$ and N can be calculated accurately. Alternatively, if N is carefully determined, one can infer the effective mass of the probed free charge carriers. Illustrated below is the frequency-resolved complex conductivity predicted by the Drude model while considering an effective mass of 1, a carrier density of 10^{17} cm^{-3} as well as a scattering rate of 10^{13} s^{-1}.

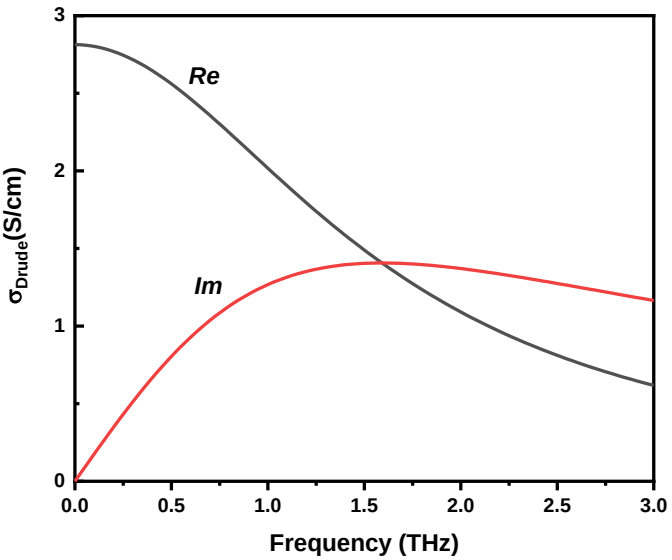

Figure 2.6. Frequency resolved conductivity spectra predicted by the Drude model: an effective mass of 1, a carrier density of 10^{17} cm^{-3} as well as a scattering rate of 10^{13} s^{-1} were considered.

2.5.2 Drude-Smith model

The Drude model is suitable to describe the conductivity of metals and semiconductors in which the charge carriers are fully delocalized. In materials where charge carriers are experiencing some degree of localization e.g. polycrystalline semiconductors, low-dimensional confined structures etc., a correction to the Drude model needs to be implemented. This was analyzed in depth by Smith [10] ; the Drude-Smith (DS) model is a phenomenological model to describe the conductivity in materials where long-range transport is impeded by backscattering of quasi-free charge carriers:

$$\tilde{\sigma}_{DS}(\omega) = \frac{e^2 N \tau_S}{m^*} \frac{1}{1-i\omega\tau_S}\left[1 + \sum_{j=1} \frac{c_j}{(1-i\omega\tau_S)^j}\right] \qquad \text{(Equation 2.16)}$$

where j is the sequence of scattering event, c_j is the probability for a free carrier of maintaining its momentum of $(j-1)$th event in the jth event. When

considering only the first scattering event with a nonzero c parameter, the equation simplifies to:

$$\tilde{\sigma}_{DS}(\omega) = \frac{e^2 N \tau_S}{m^*} \frac{1}{1 - i\omega\tau_S} \left(1 + \frac{c}{1 - i\omega\tau_S}\right) \qquad \text{(Equation 2.17)}$$

where $c = c_1$, and is commonly known as backscattering parameter. The classical Drude model is recovered when $c = 0$ as illustrated in Fig.2.7, that is, when preferential backscattering of free charges is absent. DS model has been widely applied to polycrystalline semiconductors where grain boundaries are expected to limit long-range DC transport.

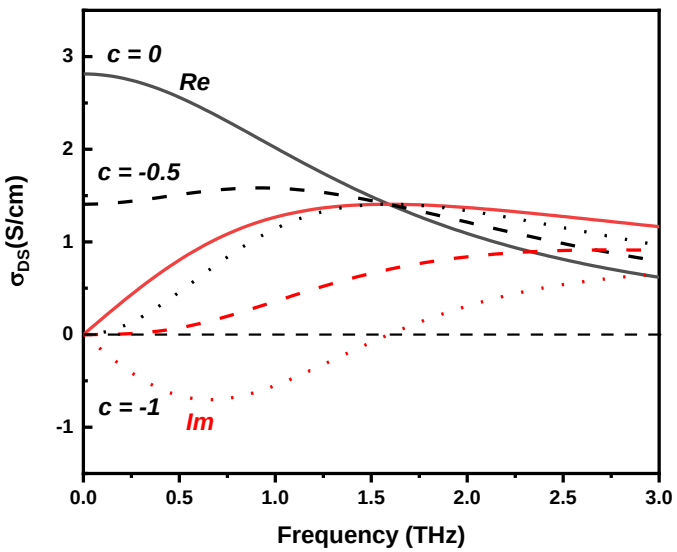

Figure.2.7. Frequency resolved conductivity spectra predicted by the DS model with varying backscattering parameter c by 0 (solid lines), -0.5 (dashed lines) and -1 (dotted lines). The black and red lines represent the real and imaginary parts of the conductivity respectively. The same effective mass, carrier density as well as scattering rate as that in Fig.2.6 were considered for all cases.

References

(1) Ulbricht, R.; Hendry, E.; Shan, J.; Heinz, T. F.; Bonn, M. Carrier Dynamics in Semiconductors Studied with Time-Resolved Terahertz Spectroscopy. Rev. Mod. Phys. 2011, 83 (2), 543–586.

(2) Schmuttenmaer, C. A. Exploring Dynamics in the Far-Infrared with Terahertz Spectroscopy. Chem. Rev. 2004, 104 (4), 1759–1780.

(3) Jensen, S. A. Charge Carrier Dynamics in Photovoltaic Materials; 2014.

(4) Dressel, M.; Grüner, G. Electrodynamics of Solids; Cambridge University Press, 2002.

(5) Duvillaret, L.; Garet, F.; Coutaz, J.-L. A Reliable Method for Extraction of Material Parameters in Terahertz Time-Domain Spectroscopy. IEEE J. Sel. Top. Quantum Electron. 1996, 2 (3), 739–746.

(6) Knoesel, E.; Bonn, M.; Shan, J.; Wang, F.; Heinz, T. F. Conductivity of Solvated Electrons in Hexane Investigated with Terahertz Time-Domain Spectroscopy. J. Chem. Phys. 2004, 121 (1), 394.

(7) Hegmann, F. A.; Lui, K. P. Optical Pump-Terahertz Probe Investigation of Carrier Relaxation in Radiation-Damaged Silicon-on-Sapphire. Ultrafast Phenom. Semicond. VI 2002, 4643 (June 2002), 31.

(8) Kindt, J. T.; Schmuttenmaer, C. A. Theory for Determination of the Low-Frequency Time-Dependent Response Function in Liquids Using Time-Resolved Terahertz Pulse Spectroscopy. J. Chem. Phys. 1999, 110 (17), 8589–8596.

(9) Sólyom, J. Fundamentals of the Physics of Solids (Volume 1); Springer Berlin Heidelberg, 2007; Vol. 1.

(10) Smith, N. Classical Generalization of the Drude Formula for the Optical Conductivity. Phys. Rev. B 2001, 64 (15), 155106.

CHAPTER 3: CHEMISORPTION OF ATOMICALLY PRECISE 42-CARBON GRAPHENE QUANTUM DOTS ON METAL OXIDE FILMS GREATLY ACCELERATES INTERFACIAL ELECTRON TRANSFER

3.1 Introduction and aim of the work

Graphene quantum dots (GQDs) are nano-sized graphene fragments, which have non-zero, size-dependent energy gaps due to quantum confinement effects.[1–3] Moreover, GQDs are metal-free and hence potentially low-cost and environment-friendly. These features have motivated researchers to apply GQDs in solar energy conversion schemes (e.g. solar cells[4–7] and photocatalytic devices[8,9]). GQDs are typically prepared by hydrothermal treatment of graphene or small molecules[1-3]; although certain control of GQD size has been achieved following this synthesis protocol[2], samples are generally defined by broad absorption features induced by inhomogeneous broadening (i.e. samples does not consist of a narrow distribution of chemical structures), an aspect that is detrimental for optoelectronic applications.

Alternatively, large polycyclic aromatic hydrocarbons (PAHs) have been synthesized in the field of organic chemistry over the last decades, being hexa-*peri*-hexabenzocoronene (HBC), consisting of 42 sp^2 carbon atoms, a representative example [10,11]. Recently, Yan *et al*. reported the synthesis of large PAHs consisting of 132, 168, and 170 sp^2 carbon atoms and referred to them as colloidal GQDs.[12,13] Such PAHs, sometimes also called nanographenes, can indeed serve as atomically precise zero dimensional GQDs, owing to their well-defined size- and shape-dependent optoelectronic properties as predicted by theoretical predictions[14–16]. Yan *et al*. also reported the use of such well-defined GQDs as absorbers in a sensitized solar cell geometry.[17] However, these initial solar cell devices revealed low photo-conversion efficiencies, mainly linked with low short-circuit currents. The poor photocurrent produced in the cells was tentatively correlated with the low affinity of the employed GQDs sensitizers, which were

physisorbed onto the mesoporous oxide surface. In a follow-up report from the same group, functionalization of the colloidal GQDs by carboxylate groups was reported to allow better control on the interfacial bonding geometry on polar surfaces (specifically on mica) by chemisorption.[18] Furthermore, theoretical studies have shown that chemisorption – instead of physisorption - of sensitizers should favor donor-acceptor coupling and hence boost electron transfer at GQD/oxide interfaces[19,20]. Although all these works have suggested that chemisorption of GQDs onto metal oxides might improve photoconversion efficiencies in sensitized systems, there is at present no experimental evidence to support that claim. Here, we quantify interfacial electron transfer (ET) rates for atomically precise GQD_{C42} (HBC with 42 sp^2 carbon atoms) chemisorbed and physisorbed on mesoporous SnO_2 by optical pump-terahertz probe (OPTP) spectroscopy. We demonstrate that sensitizer chemisorption onto the oxide electrode substantially improves ET rates induced by strong overlap (hybridization) between donor and acceptor wavefunctions, which is triggered by the functionalization of the GQD_{C42} by a carboxylate group. This claim is directly evident from the OPTP data and is further supported by absorption spectroscopy, valence band X-ray photoelectron spectroscopy (VBXPS) and density functional theory (DFT) calculations.

3.2 Methods

3.2.1 Materials

The samples were provided by the group of Prof. Klaus Müllen and Dr. Akimitsu Narita at Max Planck Institute for Polymer Research. The molecular structures of the two GQD_{C42} samples used in this study are shown in Figure 3.1. For clarity, we name our samples as GQD_{C42} and GQD_{C42}-PhCOOH for the sensitizer without and with a phenyl carboxylic acid functional group respectively.

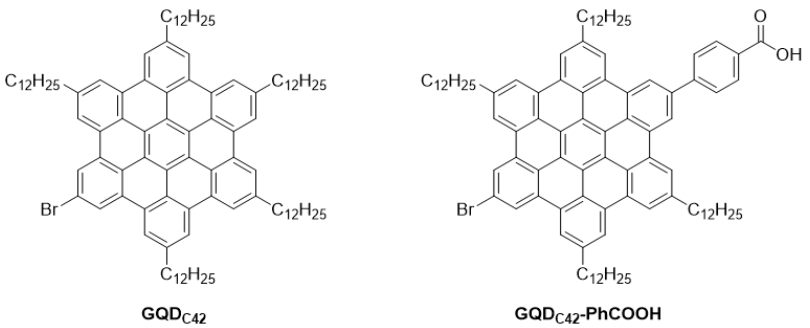

Figure 3.1. Chemical structures of the graphene quantum dots, GQD_{C42} and GQD_{C42}-PhCOOH, analyzed in this study; they differ on the presence of a carboxylate functional group which is expected to serve as a covalent link to the oxide electrode.

3.2.2 Synthesis

The GQD_{C42} sample was prepared by the same group mentioned above following a protocol described previously [21] and the synthesis of GQD_{C42}-PhCOOH is described in the Appendix. In brief, GQD_{C42}-PhCOOH was synthesized starting from a hexaphenylbenzene derivative bearing bromo- and iodo-groups through a Suzuki-coupling reaction to selectively introduce a phenyl ester moiety and subsequent cyclodehydrogenation reaction to convert the hexaphenylbenzene core into HBC. Finally, the ester group was hydrolyzed under basic conditions to the desired carboxylic acid anchoring group. The synthesized samples were diluted in toluene, and the obtained suspensions were employed for sensitizing the mesoporous oxide films (see appendix for sample preparation details).

3.2.3 Characterization

The functionalized films were subsequently characterized by OPTP spectroscopy introduced in Chapter 2; the measurements were performed under nitrogen conditions to prevent any potential sensitizer photo-oxidation. Apart from THz spectrosocpy, gas-phase density functional theory (DFT) calculation performed by Dr. Xiao-Ye Wang were employed in order to investigate the nature of interfacial electron transfer dynamics in those systems. The UV-VIS absorbance spectroscopy as well as valence band x-ray photoelectron spectroscopy (VBXPS) peformed and analyzed by Dr. Hao Lu were assisted for the same purpose but from the experimental perspective. For more details regarding these characterization techniques, please see the Apendix.

3.3 Results and discussion

3.3.1 OPTP characterization

OPTP spectroscopy is a powerful tool to investigate ultrafast interfacial dynamics for dye-[22–26] and QD-[27–29] sensitized oxide systems. As the employed THz probe (~1.5 THz bandwidth) is primarily sensitive to free carrier motion (i.e. photoconductivity), an OPTP measurement in a sensitized oxide neatly probes the emergence of photoconductivity in the oxide electrode after selective excitation of the sensitizer. As such, it resolves, in time, the arrival of electrons from the sensitizer's populated molecular orbitals (e.g. LUMO) into the oxide's conduction band (CB). Figure 3.2(a) shows normalized OPTP dynamics for GQD_{C42} and GQD_{C42}-PhCOOH sensitizing SnO_2 mesoporous films (blue diamonds and red circles respectively; 400nm pump excitation, 0.6 mJ/cm^2); these dynamics were collected in the linear single-exciton regime (see figure 3.5). The lack of response under 400 nm pump excitation of a bare SnO_2 mesoporous oxide film is also presented in figure 3.2(a) (black triangles). As evident from figure 3.2(a), the sensitization of mesoporous SnO_2 by the sensitizer functionalized with a phenyl carboxylate group (GQD_{C42}-PhCOOH, figure 3.1) – which is expected to chemisorb at the oxide surface – results in faster ET rates when compared with the sensitizer lacking functionalization (GQD_{C42} in figure 3.1), which is expected to physisorb at the oxide surface. Both traces can be well described phenomenologically by a bi-phasic exponential model (solid red lines in figure 3.2), providing time constants of $\tau_1 = 12 \pm 1$ ps and $\tau_2 = 2025 \pm 450$ ps for GQD_{C42} sensitized SnO_2 films; and $\tau_1 = 0.2 \pm 0.1$ ps and $\tau_2 = 51 \pm 3$ ps for GQD_{C42}-PhCOOH sensitized SnO_2 films. Biphasic ET dynamics are a common observable for dye- and QD- sensitized oxide systems that have been generally explained in terms of two distinct transfer channels towards the oxide electrode. They might be linked with "hot" and "cold" ET channels [30,31], or, alternatively, to "cold" ET channels induced by two donor-acceptor interfacial conformations (i.e., providing distinct donor-acceptor energetics) [32]. Biphasic dynamics have been also rationalized by considering effects induced by molecules loosely attached (physisorbed) to the surface or those present in form of the aggregates [29,33,34]. Even though it is difficult to rule out any of these scenarios from the current data, the fact that both ET components become faster when QDs are chemisorbed onto the oxide matrix supports the view that two ET channels define our interfacial dynamics. A deeper

analysis of the nature of the bi-phasic signals is underway and will be reported elsewhere.

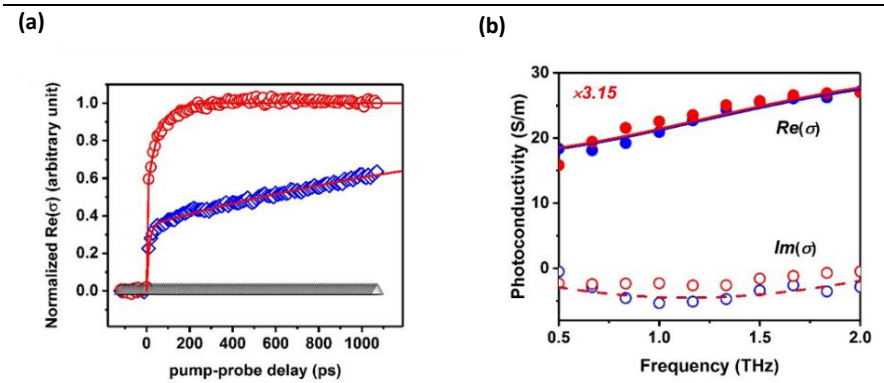

Figure 3.2. (a) OPTP dynamics of GQD_{C42} (open blue diamonds) and GQD_{C42}-PhCOOH (open red circles) sensitizing SnO_2 films (400nm pump excitation, 0.6mJ cm^{-2}). Traces are normalized to the plateau of the bi-exponential fits (solid red lines). Black open triangles are OPTP dynamics for a bare SnO_2 film. (b) Frequency-resolved complex photoconductivity for both sensitized systems (1ns after photoexcitation); solid and dashed lines correspond to Drude-Smith fits for the real and imaginary components of the frequency dependent conductivity.

To validate the conclusion of faster ET rates for the chemisorbed sensitizers inferred from the OPTP data, we analyze the frequency-resolved complex photoconductivity in the samples. This approach can tell whether OPTP dynamics indeed refer uniquely to electrons populating the oxide conduction band. Figure 3.2(b) presents the real and imaginary (closed and open symbols) components of the complex conductivity for GQD_{C42} (blue), and GQD_{C42}-PhCOOH (red) sensitized oxide films (1ns after excitation, 1.5 THz bandwidth). As evident from figure 3.2(b), the complex photoconductivity spectra for chemisorbed and physisorbed dots onto the oxide overlap quite well, indicating that the nature of the monitored photoconductivity for both samples is identical, as expected for electrons in SnO_2. The resolved complex spectra can be well described by Eqn.2.17 representing the phenomenological Drude-Smith (DS) model [35]. Within the DS model, the measurable frequency-resolved photoconductivity can be attributed to free carriers experiencing preferential backscattering at the boundaries of the nanocrystalline mesoporous oxide electrode [22,36]. The strength of the localization is parametrized by c, which ranges between 0 (free carrier -

Drude reponse) and -1 (representing full localization of charges). Best fit to the data using Eqn.2.17 for both samples provide the same fitting parameters within error; a scattering rate of $\tau_s = 46 \pm 2\ fs$ and localization factor of $c = -0.69 \pm 0.1$. These results are in good agreement with previous values inferred for nanostructured SnO_2 films [37–39], and hence demonstrate that the monitored signal in figure 3.2(a) refers uniquely to electrons populating the oxide conduction band. These results support our conclusion that the changes in the monitored interfacial ET rates can be traced uniquely to the presence of the phenyl carboxylate group functionalizing the GQD_{C42}-PhCOOH, allowing for chemisorption. Furthermore, these results reveal that electron transport within the analyzed SnO_2 electrode is unaffected by the type of functionalization (chemisorption or physisorption).

To check the generality of our observation that ET is accelerated for chemisorbed sensitizers, we also measured interfacial ET dynamics for both sensitizers onto mesoporous ZnO and TiO_2 films (figure 3.7). For ZnO samples we observed as well faster ET rates for the chemisorbed sensitizers, analogous to the case of SnO_2 based samples (figure 3.2). For titania, ET occurs faster than our experimental sub-ps time resolution for both sensitizers, so we are unable to determine changes in ET rates for this set of samples. The overall slower ET rates observed for ZnO and SnO_2 electrodes when compared to titania – generally explained in terms of larger density of states for the latter improving donor-acceptor coupling strength – agree qualitatively with those reported for organo-metallic dye sensitizers onto the same electrodes [40]. Overall, the results support the view that the presence of a phenyl carboxylate group facilitates ET transfer towards the electrode independently of its nature.

3.3.2 Gas-phase DFT calculations

To rationalize our finding of faster ET for chemisorbed GQD_{C42}, we investigate the nature of the interaction between sensitizer donor and oxide acceptor. Figure 3.3 presents the relative energy level alignments. For the SnO_2 electrode, the energy positions are obtained from ultraviolet photoelectron spectroscopy measured by Dr. Hao Lu (UPS, see figure 3.9) and absorbance. For the two molecules, the highest occupied molecular orbital (HOMO) and lowest unoccupied molecular orbital (LUMO) were obtained from gas-phase DFT calculations. When the interaction of the metal oxide with the molecules is not taken into account, upon sensitization, the slightly larger ΔG (the energy

difference between the LUMO of the sensitizer and the CB of the electron-accepting oxide, see figure 3.3) for the GQD_{C42} lacking a carboxylate group should lead to faster ET for the physisorbed sensitizers[29]. From the OPTP data shown in figure 3.2(a), it is clear that this is not the case, which shows that the chemical interaction between chemisorbed GQD_{C42}-PhCOOH and the oxide electrode affects donor-acceptor energetics (and hence coupling strength). The frontier orbitals obtained from DFT calculations offer some insight on this aspect. As shown in figure 3.3, the sensitizer expected to chemisorb to the oxide surface (GQD_{C42}-PhCOOH) reveals a substantial LUMO distribution on carboxylate group, which is expected to deprotonate and bond to the oxide surface. The localization of the LUMO nearer the oxide surface will provide enhanced donor-acceptor coupling strength (donor-acceptor wavefunction overlap) when compared with the physisorbed case, in line with the OPTP data shown in figure 3.2(a). Faster ET rates as a function of shorter donor-acceptor orbital distances between sensitizers and metal oxides have been demonstrated in quantum dot-oxide [41] and dye-oxide [40] systems.

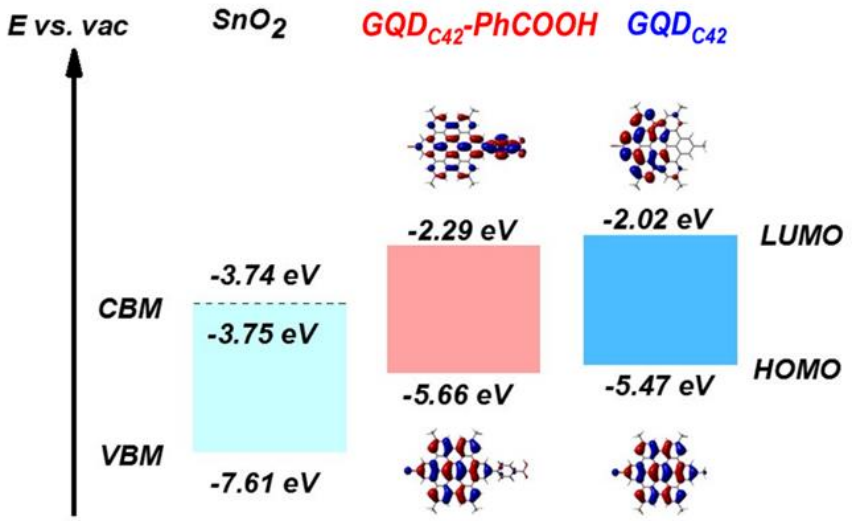

Figure 3.3. Interfacial donor-acceptor energetics derived from gas-phase DFT calculations for GQD_{C42} and GQD_{C42}-PhCOOH sensitizers and from UPS for tin oxide. Frontier orbital distributions of HOMO and LUMO for both sensitizers are also presented. The Fermi level for the tin oxide sample is within the oxide CB, indicating strong n-type character.

3.3.3 Absorbance & Valence Band XPS

To reveal a stronger interaction between chemisorbed GQD_{C42} orbitals and the oxide conduction band, we analyzed the samples by optical absorption and valence band X-ray photoelectron spectroscopy. In figure 3.4(a) we present the UV-VIS absorbance spectrum of both sensitized systems (solid red and blue lines for chemisorbed and physisorbed GQD_{C42} respectively) along with the bare oxide film (black line). Figure 3.4(a) also provides the spectra of the toluene solution of both sensitizers (dashed red and blue lines for chemisorbed and physisorbed GQD_{C42} respectively); the absorption profiles peak at 3.45 eV and 3.39 eV for GQD_{C42} and GQD_{C42}-PhCOOHs respectively. Whereas the peak absorbance for GQD_{C42} remains essentially identical upon sensitization, a clear blue shift is resolved for the peak absorbance of the GQD_{C42}-PhCOOH sensitizers after binding to the oxide electrode (dotted and solid red lines in figure 3.4(a)). A similar blue shift in the absorbance after sensitization has been previously reported for dye-sensitized films and explained in terms of the strong coupling induced by deprotonation of the dyes [42–45] induced by chemisorption; in good agreement with our expectations.

In figure 3.4(b) we present valence band X-ray photoelectron spectroscopy (VBXPS) data for a bare SnO_2 mesoporous film (solid black line) and oxide electrodes functionalized by GQD_{C42}-PhCOOH and GQD_{C42} sensitizers (red and blue line respectively). As evident from the plot, the physisorbed GQD_{C42} sensitized and the bare tin oxide electrodes reveal identical electron binding energies. However, the electron binding energy is reduced by approximately 2 eV upon chemisorption of GQD_{C42}-PhCOOHs, indicating significant/efficient modification/decoration of the surface of the oxide, which was absent upon the physisorption (the results were reproducible within ~50 meV for samples produced in three different batches). The observed change in electron binding energy can be explained by chemical modification at the oxide interface (e.g. deprotonation of COOH groups able to modify the Fermi energy at the oxide) and/or by dipolar effects (modifying vacuum levels induced by the presence of a surface electric field induced by sensitization) [46]. In any case, it reveals a strong donor-acceptor interaction for the chemisorbed GQD_{C42}, in qualitative agreement with absorbance spectra shown in figure 3.4(a) and the expected closer proximity of frontier orbitals inferred by DFT calculation (figure 3.3). All these results support qualitatively the experimentally resolved effect on interfacial OPTP

dynamics, i.e. the main conclusion of this work: chemisorption of GQD_{C42}, enabled by their functionalization with a carboxylate group, substantially enhances ET rates.

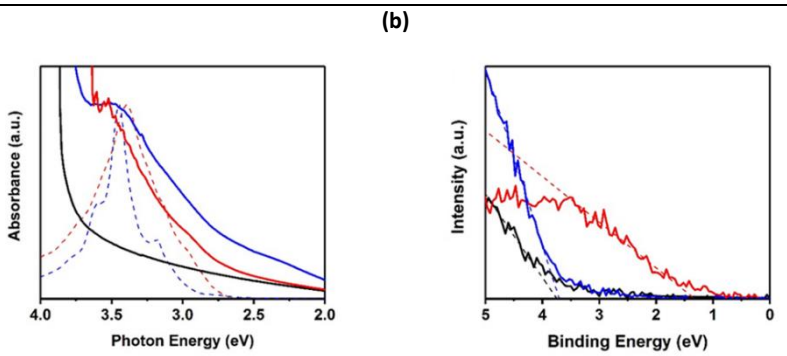

Figure 3.4. (a) UV-VIS absorbance spectrum of GQD_{C42} (blue) and GQD_{C42}-PhCOOH (red) sensitized SnO_2 films and for sensitizers dispersed in solution (dashed lines). The spectrum of bare SnO_2 film is also shown (solid black line). (b) Valence band X-ray spectra of GQD_{C42} (blue) and GQD_{C42}-PhCOOH (red) sensitized and bare (black) SnO_2 electrodes. The dashed lines are linear fits enabling binding energy estimates for the analyzed systems.

3.4 Summary

In summary, we investigated the rates of electron transfer from physisorbed and chemisorbed graphene quantum dot (GQD) sensitizers to metal oxides, using hexa-*peri*-hexabenzocoronene derivatives as atomically precise GQDs. An increase of ET rates as large as two orders of magnitude is observed for chemisorbed sensitizers when compared with physisorbed ones. Accelerated electron transfer is correlated with enhanced donor-acceptor coupling (i.e. wavefunction hybridization). These results demonstrate that functionalization of GQDs with anchoring head groups represents a potential path for improved photoconversion efficiencies in carbon-based sensitizer/oxide electrodes employed in solar energy conversion schemes.

3.5 Appendix

I acknowledge here the contribution of Prof. Klaus Müllen and Dr. Akimitsu Narita for preparing graphene quantum dots; Dr. Hao Lu for characterizing the GQDs sensitized metal oxide films with Ultraviolet Photoelectron Spectroscopy (UPS), Valence Band X-ray Photoelectron Spectroscopy (VBXPS), and X-ray Photoelectron Spectroscopy (XPS); Dr. Xiao-Ye Wang for the First-Principles Calculations.

3.5.1 Materials and methods

a) General methods

All reactions working with air- or moisture-sensitive compounds were carried out under argon atmosphere using standard Schlenk line techniques. Unless otherwise noted, all starting materials and reagents were purchased from commercial sources (such as Alfa Aesar, Sigma-Aldrich, Acros and TCI) and used without further purification. Thin layer chromatography (TLC) was performed on silica gel coated aluminum sheets with F254 indicator and silica gel column chromatography separation was performed with the 0.063–0.200 mm particle size. Nuclear Magnetic Resonance (NMR) spectra were recorded in deuterated solvents using Bruker AVANCE III 500 and Bruker AVANCE III 700 MHz NMR spectrometers. Chemical shifts (δ) were expressed in ppm relative to the residual of solvent (CD2Cl2 @ 5.32 ppm for 1H NMR, 54.00 ppm for 13C NMR, C2D2Cl4 @ 6.00 ppm for 1H NMR, 73.78 ppm for 13C NMR). Coupling constants (*J*) were recorded in Hertz (Hz) with multiplicities explained by the following abbreviations: s = singlet, d = doublet, t = triplet, q =quartet, dd = double of doublets, dt = doublet of triplets, m = multiplet, br = broad. The micro-FT-IR spectra were recorded through a diamond anvil cell (transmission mode) with a Nicolet Nexus FT-IR spectrometer coupled with a Thermo Electron Continuum IR microscope. The wavenumber (ν) is expressed in cm^{-1}. UV–VIS absorption spectra were measured on a Perkin-Elmer Lambda 900 spectrophotometer at room temperature. High-resolution mass spectra (HRMS) were recorded by matrix-assisted laser decomposition/ionization (MALDI) using 7,7,8,8-tetracyanoquinodimethane (TCNQ) as matrix on a Bruker Reflex II-TOF spectrometer (MALDI-TOF HRMS).

b) Sample preparation

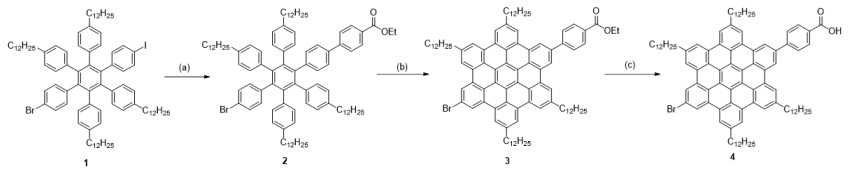

Scheme 3.1. The synthesis of GQD_{C42}-PhCOOH. Reagents and conditions: (a) $Pd(PPh_3)_4$, K_2CO_3, toluene/water/ethanol, 70 °C, 1 h. (b) $FeCl_3$, dichloromethane/nitromethane, rt, 1 h. (c) KO*t*Bu, H_2O (3 eq.), tetrahydrofuran, rt, overnight.

Synthesis of ethyl 5'-(4-bromophenyl)-4-dodecyl-3',4',6'-tris(4-dodecylphenyl)-[1,1':2',1'':4'',1'''-quaterphenyl]-4'''-carboxylate (2 in Scheme.3.1)

To a suspension of 4-bromo-4''-dodecyl-3',5',6'-tris(4-dodecylphenyl)-4'-(4-iodophenyl)-1,1':2',1''-terphenyl[3] (0.18 g, 0.12 mmol) and 4-ethoxycarbonylphenylboronic acid (77 mg, 0.40 mmol) in toluene (5 mL) was added a solution of K_2CO_3 (0.9 g, 7 mmol) in water (1 mL) and ethanol (1 mL). This mixture was degassed by freeze-pump-thaw technique (1 cycle). $Pd(PPh_3)_4$ (15 mg, 0.013 mmol) was then added to the mixture, which was further degassed by freeze-pump-thaw technique for another 2 cycles. The mixture was then heated at 70 °C under vigorous stirring and monitored by TLC until the starting material was consumed (about 1 h). After cooling to a room temperature, the mixture was diluted with diethyl ether and washed with water and brine. The organic layer was then dried over $MgSO_4$ and the solvent was removed in vacuo. The residue was purified by silica gel column chromatography (eluent: ethyl acetate/hexane = 1/6) to afford the title compound as pale yellow oil (0.14 g, 81%). ^{1}H NMR (700 MHz, CD_2Cl_2): δ 7.98 (d, J = 8.4 Hz, 2H), 7.49 (d, J = 8.4 Hz, 2H), 7.17 (d, J = 8.1 Hz, 2H), 6.98 (d, J = 8.4 Hz, 2H), 6.93 (d, J = 8.1 Hz, 2H), 6.76–6.69 (m, 14 H) 6.67 (d, J = 8.0 Hz, 4H), 4.33 (q, J = 7.1 Hz, 2H), 2.39 (t, J = 7.5 Hz, 4H), 2.35 (t, J = 7.5 Hz, 4H), 1.41 (quint, J = 7.9 Hz, 8H), 1.39–1.02 (m, 75 H), 0.92–0.85 (m, 12 H). ^{13}C NMR (126 MHz, CD_2Cl_2) δ 166.78, 145.49, 141.85, 141.06, 140.91, 140.86, 140.69, 140.50, 140.41, 139.84, 138.42, 138.32, 136.77, 133.81, 132.67, 131.78, 131.76, 130.34, 130.10, 129.61, 127.34, 127.26, 126.99, 125.66, 119.64, 61.41, 54.43,

54.22, 54.00, 53.79, 53.57, 35.81, 32.52, 31.84, 31.80, 30.34, 30.30, 30.27, 30.20, 30.10, 30.04, 29.97, 29.95, 29.39, 29.36, 23.28, 14.68, 14.46. HRMS (MALDI-TOF) calcd. for $C_{99}H_{133}BrO_2$ $[M]^+$, 1432.9489. Found $[M]^+$ 1432.9426.

Synthesis of ethyl 4-(11-bromo-5,8,14,17-tetradodecylhexa-peri-hexabenzocoronen-2-yl)benzoate (3 in Scheme.3.1)

A solution of **2** (0.17 g, 0.12 mmol) in unstabilized dichloromethane (50 mL) was degassed by argon bubbling for 5 min. The argon bubbling was continued for the whole reaction period. To this solution was added a solution of $FeCl_3$ (0.6 g, 4 mmol) in nitromethane (5 mL). The reaction mixture turned dark brawn immediately. The mixture was stirred at a room temperature for 1 h and then poured into methanol (400 mL). Two drops of brine was added to the mixture to facilitate precipitation. The precipitates were collected by vacuum filtration and purified by silica gel column chromatography (eluent: hot toluene) to afford the title compound as a bright yellow solid (161 mg, 95%). ^{1}H NMR (700 MHz, $C_2D_2Cl_4$, 373 K): δ 8.37 (d, J = 7.0 Hz, 2H), 8.17 (br, 2H), 7.92 (d, J = 7.0 Hz, 2H), 7.83 (br, 2H), 7.77 (br, 2H), 7.63 (br, 2H), 7.60 (br, 2H), 7.49 (br, 2H), 4.60 (q, J = 7.2 Hz, 2H), 2.78 (br, 4H), 2.70 (br, 4H), 1.90 (br, 4H), 1.83 (br, 4H), 1.73-1.18 (m, 75H), 1.02-0.87 (m, 12H). ^{13}C NMR (176 MHz, $C_2D_2Cl_4$, 373 K): δ 166.25, 145.96, 139.03, 138.99, 135.37, 135.25, 135.21, 130.25, 130.10, 129.46, 128.97, 128.19, 128.15, 127.03, 123.01, 122.58, 121.72, 121.70, 121.53, 121.47, 120.86, 120.52, 120.25, 120.04, 118.62, 118.00, 117.60, 117.48, 117.28, 60.79, 36.77, 36.67, 31.72, 31.56, 31.46, 29.95, 29.77, 29.74, 29.66, 29.63, 29.52, 29.14, 22.41, 14.33, 13.74. IR: ν = 3063, 2952, 2917, 2849, 1719, 1609, 1576, 1466, 1271, 1104, 1021, 861, 849, 771, 721, 705. HRMS (MALDI-TOF) calcd. for $C_{99}H_{121}BrO_2$ $[M]^+$, 1420.8550. Found $[M]^+$ 1420.8501.

Synthesis of 4-(11-bromo-5,8,14,17-tetradodecylhexa-peri-hexabenzocoronen -2-yl)benzoic acid (4 in Scheme.3.1)

To a solution of **3** (30 mg, 21 μmol) and water (1.1 mg, 62 μmol) in tetrahydrofuran (7 mL) was added a tetrahydrofuran solution of KO*t*Bu (0.19 mL, 1 M, 190 μmol) at a room temperature. The mixture was stirred overnight and poured into methanol (50 mL). The precipitates were collected by vacuum filtration and washed with water, methanol and acetone to afford the title compound as a brownish orange solid (29 mg, 99%). HRMS (MALDI-TOF) calcd. for $C_{97}H_{117}BrO_2$ $[M]^+$, 1392.8237. Found $[M]^+$ 1392.8180. IR: ν = 3062, 2952, 2919,

2849, 1687, 1609, 1576, 1464, 1414, 1367, 1181, 861, 849, 774, 719, 613, 553, 492. Because of the strong aggregation of **3** in solution, NMR spectra could not be resolved.

Preparation of GQDs sensitized metal oxide films

Mesoporous metal oxide films (SnO_2, ZnO, TiO_2) were prepared by doctor-blading method. After sintering at 450 °C for 2h, they were left to cool down to 80 °C. After this, we immersed the mesoporous films in an anhydrous toluene solution containing the graphene dots (1 mg/5 mL). To allow the sensitization, the samples remained in a N_2 purged glovebox overnight. The obtained sensitized films were rinsed in Toluene and dried under N_2 environment without applying any thermal treatment during the process.

c) Ultraviolet Photoelectron Spectroscopy (UPS), Valence Band X-ray Photoelectron Spectroscopy (VBXPS) , and X-ray Photoelectron Spectroscopy (XPS)

UPS and VBXPS measurements were conducted on a Kratos Axis Ultra^{DLD} spectrometer (Kratos, Manchester, England). In these measurements, the samples were transported from an inert-atmosphere glovebox (<1 ppm of O_2) to the vacuum system (2×10^{-7} mbar) immediately after they were prepared. In UPS measurement, electrical contact was always applied. The sample was held at a bias of –9 V with respect to the spectrometer. Illumination at 21.2 eV is provided by the He(I) emission line from a helium discharge lamp, and the chamber pressure increases from ~10^{-10} to ~10^{-7} mbar. Photoelectron emission was collected at 0° from the surface normal of the samples. The spectra were taken in three different spots to confirm the spectra reproducibility and irradiation exposure time was kept under one minute. VBXPS spectra were collected using an Al Kα excitation source with a photon energy of 1487 eV. Spectra were acquired in hybrid mode of the analyzer lens, using a 0° take-off angle, which is defined as the angle between the surface normal and the axis of the analyzer lens.

d) First-Principles Calculations

DFT calculations were performed using the Gaussian 09 software package.[47] The geometry and energies were calculated at the B3LYP/6-311+G(d,p) level. All alkyl chains were replaced with methyl groups for computational simplicity.

3.5.2 Supplementary figures

a) OPTP dynamics of GQDs Sensitized SnO_2 in Linear Single-Exciton Regime

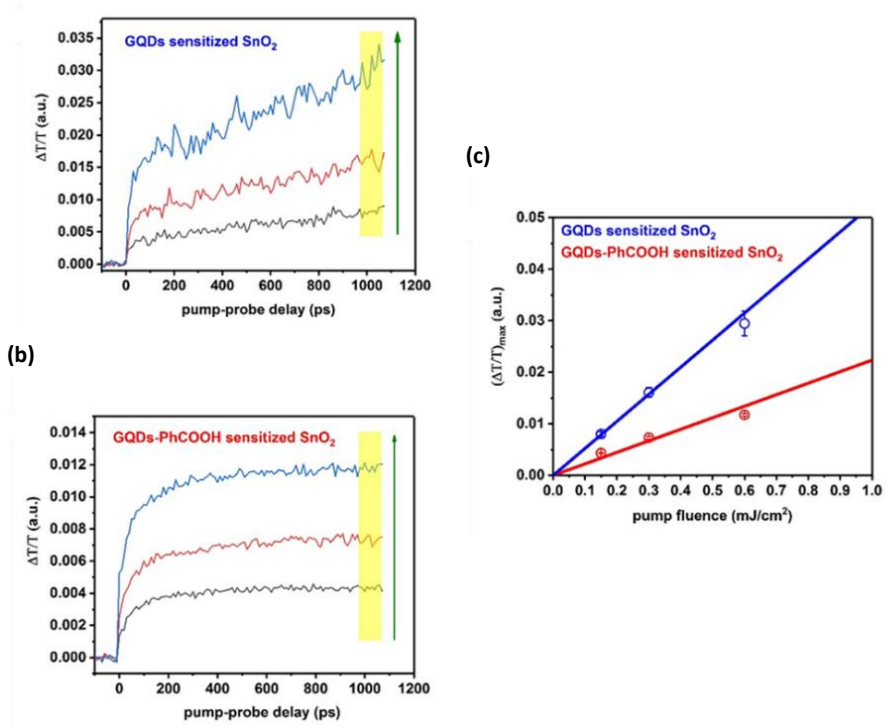

Figure 3.5. OPTP dynamics of (a) GQDs sensitized SnO_2 and (b) GQDs-PhCOOH sensitized SnO_2 as a function of 400 nm pump excitation fluence. The data demonstrate that excitation in the linear regime (i.e., the signals scale linearly with fluence, hence no change of oxide mobility in the oxide is resolved).

b) Oscillations in frequency-resolved photoconductivity spectra

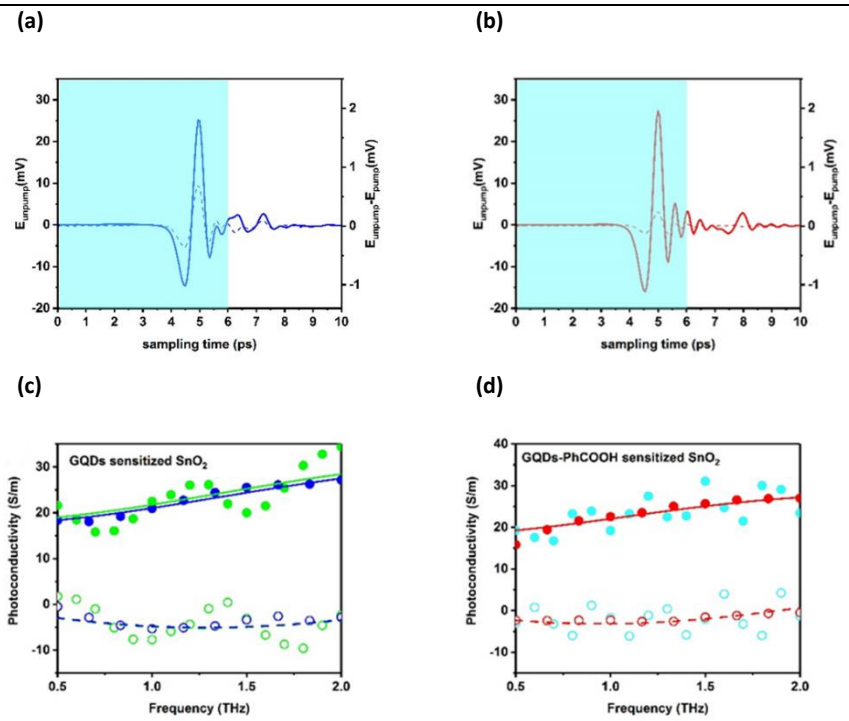

Figure 3.6. (Top figures) THz probe line shapes in the time domain for both samples. A series of oscillations appear at time delays above 6 ps that we tentatively correlate with multiple reflections of the pump excitation for our sample/substrate geometry (QD-oxide film/fused silica). Fourier transformation of bare data reveals oscillations in the complex conductivity line shape in the frequency domain (bottom panels). The oscillations can be filtered out by shorting the time spam (from 0 to 6ps) prior Fourier transformation. Fits to the Drude-Smith model for bare and filtered data in the frequency domain (solid and dashed lines in bottom panel) demonstrate that the filtering protocol is barely affecting the inferred photophysical response of the analyzed systems.

c) OPTP dynamics of GQDs Sensitized ZnO/TiO_2

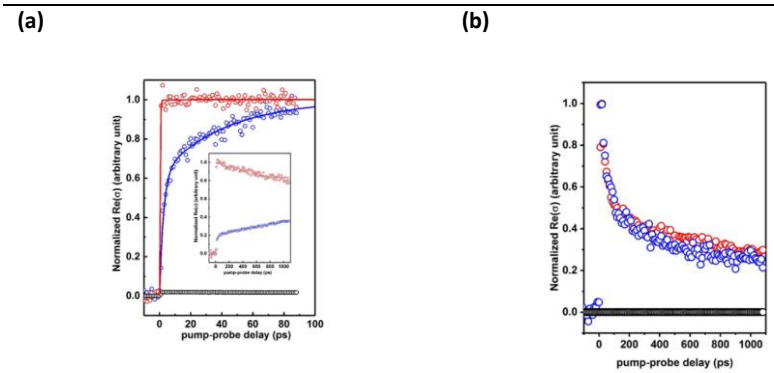

Figure 3.7. Normalized OPTP dynamics of GQDs sensitized ZnO films (a) and TiO_2 films (b) excited under the same conditions employed for sensitized SnO_2 films for fig 3.3(a) in the manuscript. Dynamics in bare ZnO and TiO_2 films are also shown (black open circles). Biphasic fits for the ZnO case provide ET time constant τ_1 = 3 ps, τ_2 = 42 ps for physisorbed case and τ_1 = 0.3 ps, τ_2 = 13 ps for chemisorbed case respectively. The ET components for TiO_2 are faster than our setup resolution (sub 100fs).

d) Frequency-Resolved Photoconductivity of GQDs Sensitized ZnO/TiO2

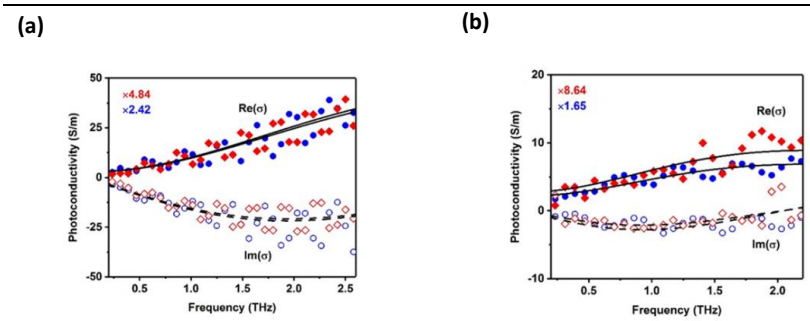

Figure 3.8. Frequency-resolved complex photoconductivity (solid and open dots for the real and imaginary components) for (a) sensitized ZnO systems and (b) TiO_2 system (1ns after excitation). Solid and dashed lines are best fits to the DS model. Best fit in mesoporous ZnO films provides a scattering rate and localization parameter of τ_s = 33.6 fs and c = -0.97, which agrees well with previous reports [48]. For titania, we obtain from the DS fits τ_s = 64.5 fs and c = -0.84, also in agreement with literature[22].

e) UPS data of Mesoporous SnO_2 Film

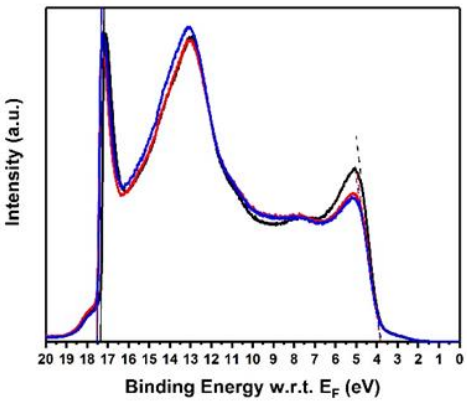

Figure 3.9. Ultraviolet photoelectron spectroscopy (UPS) data of three spots on the same SnO_2 film (solid lines). Two cutoffs were resolved for each spectrum: the one close to the Fermi level representing valence band edge (VBE) of SnO_2; the one far from the Fermi level representing vacuum level in each spot. From these cutoffs, we can obtain the workfunction of the system.

f) Absorption Spectrum of Mesoporous SnO_2 Film

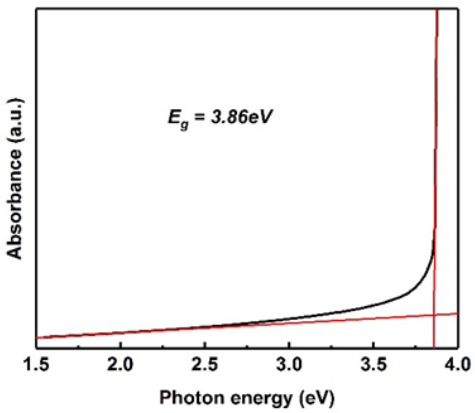

Figure 3.10. Absorption spectrum of bare SnO_2 film. A bandgap of 3.86 eV can be inferred by linear extrapolation.

g) Other characterizations

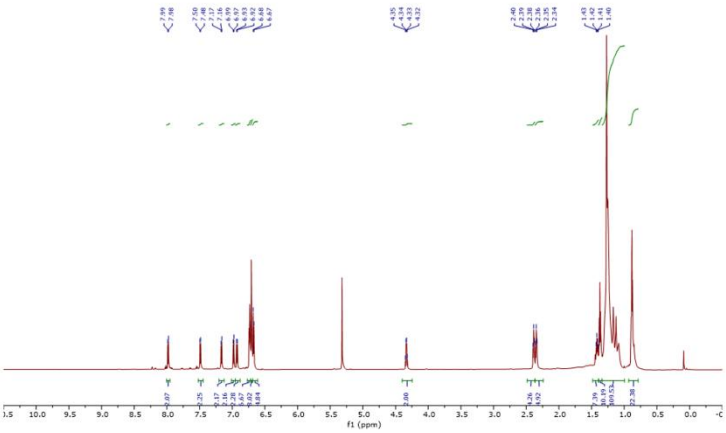

Figure 3.11. ^{1}H NMR spectrum of 2 in CD_2Cl_2 (700 MHz).

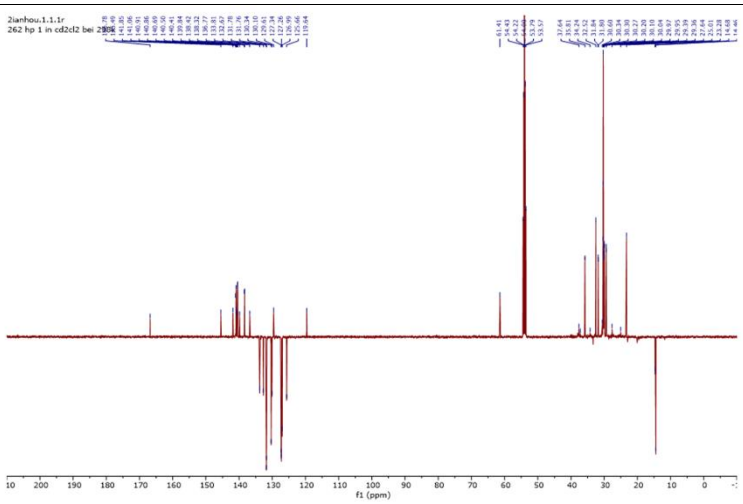

Figure 3.12. ^{13}C NMR spectrum of 2 in CD_2Cl_2 (126 MHz).

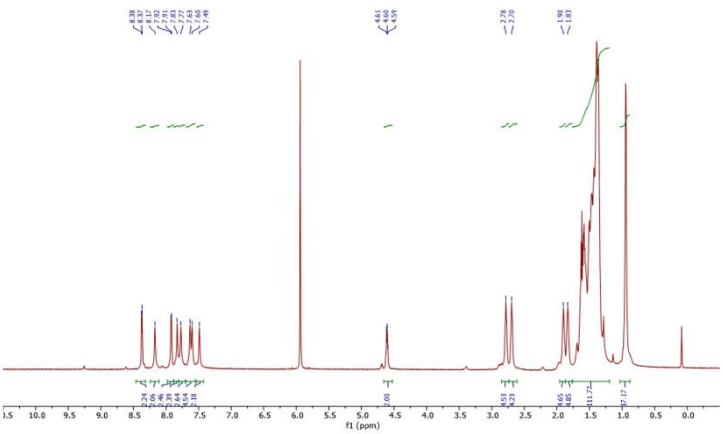

Figure 3.13. ^{1}H NMR spectrum of 3 in $C_2D_2Cl_4$ (700 MHz, 373 K).

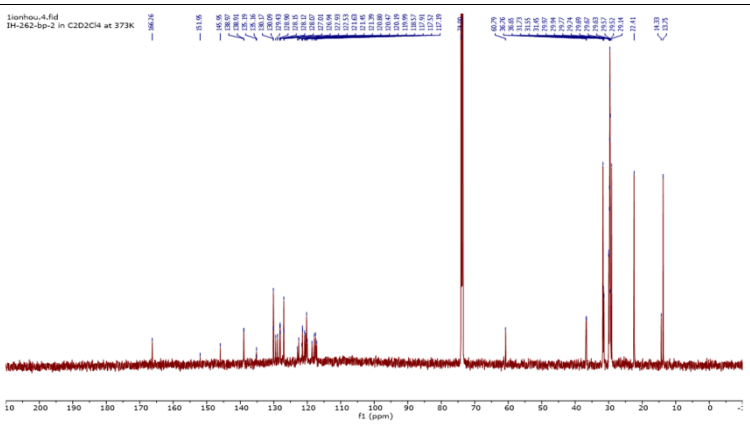

Figure 3.14. ^{13}C NMR spectrum of 3 in $C_2D_2Cl_4$ (176 MHz, 373 K).

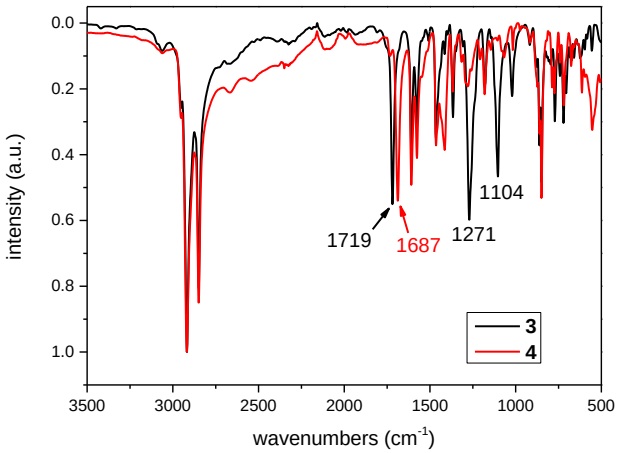

Figure 3.15. Infrared absorption spectra of 3 and 4. The complete transformation of ester functional group into carboxylic group is clearly demonstrated by the infrared absorption spectral change of carbonyl functional groups, which shifts from 1719 cm^{-1} (benzoic ester) to 1687 cm^{-1} (benzoic acid).

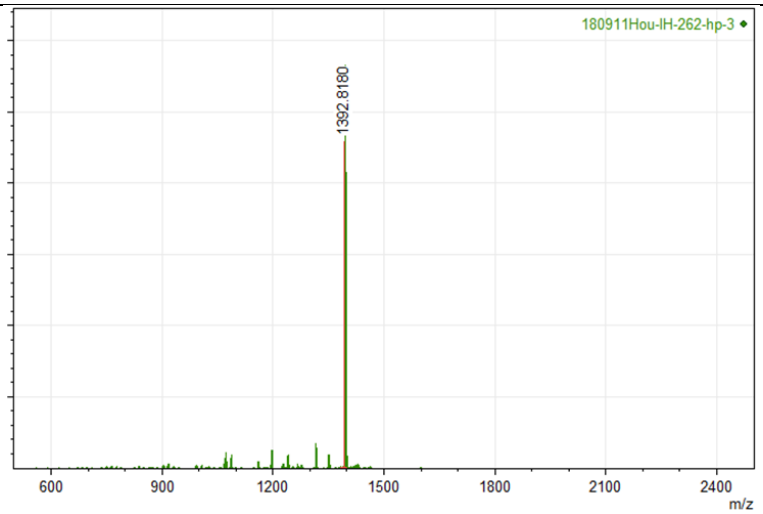

Figure 3.16. HRMS (MALDI-TOF) spectrum of 4 (matrix: TCNQ).

References

(1) Zheng, P.; Wu, N. Fluorescence and Sensing Applications of Graphene Oxide and Graphene Quantum Dots: A Review. Chem. - An Asian J. 2017, 12 (18), 2343–2353.

(2) Li, X.; Rui, M.; Song, J.; Shen, Z.; Zeng, H. Carbon and Graphene Quantum Dots for Optoelectronic and Energy Devices: A Review. Adv. Funct. Mater. 2015, 25 (31), 4929–4947.

(3) Li, L.; Wu, G.; Yang, G.; Peng, J.; Zhao, J.; Zhu, J.-J. Focusing on Luminescent Graphene Quantum Dots: Current Status and Future Perspectives. Nanoscale 2013, 5 (10), 4015.

(4) Zamiri, G.; Bagheri, S. Fabrication of Green Dye-Sensitized Solar Cell Based on ZnO Nanoparticles as a Photoanode and Graphene Quantum Dots as a Photo-Sensitizer. J. Colloid Interface Sci. 2018, 511, 318–324.

(5) Chen, L.; Guo, C. X.; Zhang, Q.; Lei, Y.; Xie, J.; Ee, S.; Guai, G.; Song, Q.; Li, C. M. Graphene Quantum-Dot-Doped Polypyrrole Counter Electrode for High-Performance Dye-Sensitized Solar Cells. ACS Appl. Mater. Interfaces 2013, 5 (6), 2047–2052.

(6) Dinari, M.; Momeni, M. M.; Goudarzirad, M. Dye-Sensitized Solar Cells Based on Nanocomposite of Polyaniline/Graphene Quantum Dots. J. Mater. Sci. 2016, 51 (6), 2964–2971.

(7) Mihalache, I.; Radoi, A.; Mihaila, M.; Munteanu, C.; Marin, A.; Danila, M.; Kusko, M.; Kusko, C. Charge and Energy Transfer Interplay in Hybrid Sensitized Solar Cells Mediated by Graphene Quantum Dots. Electrochim. Acta 2015, 153, 306–315.

(8) Bayat, A.; Saievar-Iranizad, E. Graphene Quantum Dots Decorated Rutile TiO_2 Nanoflowers for Water Splitting Application. J. Energy Chem. 2018, 27 (1), 306–310.

(9) Rajender, G.; Kumar, J.; Giri, P. K. Interfacial Charge Transfer in Oxygen Deficient TiO_2-Graphene Quantum Dot Hybrid and Its Influence on the Enhanced Visible Light Photocatalysis. Appl. Catal. B Environ. 2018, 224, 960–972.

(10) Narita, A.; Wang, X.-Y.; Feng, X.; Müllen, K. New Advances in Nanographene Chemistry. Chem. Soc. Rev. 2015, 44 (18), 6616–6643.

(11) Wu, J.; Pisula, W.; Müllen, K. Graphenes as Potential Material for Electronics. Chem. Rev. 2007, 107 (3), 718–747.

(12) Yan, X.; Li, B.; Li, L.-S. Colloidal Graphene Quantum Dots with Well-Defined Structures. Acc. Chem. Res. 2013, 46 (10), 2254–2262.

(13) Yan, X.; Cui, X.; Li, L.-S. Synthesis of Large, Stable Colloidal Graphene Quantum Dots with Tunable Size. J. Am. Chem. Soc. 2010, 132 (17), 5944–5945.

(14) Rieger, R.; Müllen, K. Forever Young: Polycyclic Aromatic Hydrocarbons as Model Cases for Structural and Optical Studies. J. Phys. Org. Chem. 2010, 23 (4), n/a-n/a.

(15) Tan, Y.-Z.; Yang, B.; Parvez, K.; Narita, A.; Osella, S.; Beljonne, D.; Feng, X.; Müllen, K. Atomically Precise Edge Chlorination of Nanographenes and Its Application in Graphene Nanoribbons. Nat. Commun. 2013, 4 (1), 2646.

(16) Wang, X.-Y.; Narita, A.; Müllen, K. Precision Synthesis versus Bulk-Scale Fabrication of Graphenes. Nat. Rev. Chem. 2017, 2 (1), 0100.

(17) Yan, X.; Cui, X.; Li, B.; Li, L.-S. Large, Solution-Processable Graphene Quantum Dots as Light Absorbers for Photovoltaics. Nano Lett. 2010, 10 (5), 1869–1873.

(18) Hamilton, I. P.; Li, B.; Yan, X.; Li, L. S. Alignment of Colloidal Graphene Quantum Dots on Polar Surfaces. Nano Lett. 2011, 11 (4), 1524–1529.

(19) Seyed-Talebi, S. M.; Beheshtian, J.; Neek-amal, M. Doping Effect on the Adsorption of NH_3 Molecule onto Graphene Quantum Dot: From the Physisorption to the Chemisorption. J. Appl. Phys. 2013, 114 (12), 124307.

(20) Long, R. Understanding the Electronic Structures of Graphene Quantum Dot Physisorption and Chemisorption onto the TiO_2 (110) Surface: A First-Principles Calculation. ChemPhysChem 2013, 14 (3), 579–582.

(21) Ito, S.; Wehmeier, M.; Brand, J. D.; Kübel, C.; Epsch, R.; Rabe, J. P.; Müllen, K. Synthesis and Self-Assembly of Functionalized Hexa-Peri-Hexabenzocoronenes. Chemistry (Easton). 2000, 6 (23), 4327–4342.

(22) Turner, G. M.; Beard, M. C.; Schmuttenmaer, C. A. Carrier Localization and Cooling in Dye-Sensitized Nanocrystalline Titanium Dioxide. J. Phys. Chem. B 2002, 106 (45), 11716–11719.

(23) Tiwana, P.; Docampo, P.; Johnston, M. B.; Snaith, H. J.; Herz, L. M. Electron Mobility and Injection Dynamics in Mesoporous ZnO, SnO_2 , and TiO_2 Films Used in Dye-Sensitized Solar Cells. ACS Nano 2011, 5 (6), 5158–5166.

(24) Karakus, M.; Zhang, W.; Räder, H. J.; Bonn, M.; Cánovas, E. Electron Transfer from Bi-Isonicotinic Acid Emerges upon Photodegradation of N3-Sensitized TiO_2 Electrodes. ACS Appl. Mater. Interfaces 2017, 9 (40), 35376–35382.

(25) Tiwana, P.; Parkinson, P.; Johnston, M. B.; Snaith, H. J.; Herz, L. M. Ultrafast Terahertz Conductivity Dynamics in Mesoporous TiO_2 : Influence of Dye Sensitization and Surface Treatment in Solid-State Dye-Sensitized Solar Cells. J. Phys. Chem. C 2010, 114 (2), 1365–1371.

(26) Brauer, J. C.; Moser, J.-E. Transient Photoconductivity of Dye-Sensitized TiO_2 Nanocrystalline Films Probed by Optical Pump-THz Probe Spectroscopy. Ultrafast Phenom. XVII 2011, 358–360.

(27) Wang, H.; Barceló, I.; Lana-Villarreal, T.; Gómez, R.; Bonn, M.; Cánovas, E. Interplay Between Structure, Stoichiometry, and Electron Transfer Dynamics in SILAR-Based Quantum Dot-Sensitized Oxides. Nano Lett. 2014, 14 (10), 5780–5786.

(28) Zhao, K.; Pan, Z.; Mora-Sero, I.; Canovas, E.; Wang, H.; Song, Y.; Gong, X.; Wang, J.; Bonn, M.; Bisquert, J.; et al. Boosting Power Conversion Efficiencies of Quantum-Dot-Sensitized Solar Cells Beyond 8% by Recombination Control. J. Am. Chem. Soc. 2015, 137 (16), 5602–5609.

(29) Cánovas, E.; Moll, P.; Jensen, S. A.; Gao, Y.; Houtepen, A. J.; Siebbeles, L. D. A.; Kinge, S.; Bonn, M. Size-Dependent Electron Transfer from PbSe Quantum Dots to SnO_2 Monitored by Picosecond Terahertz Spectroscopy. Nano Lett. 2011, 11 (12), 5234–5239.

(30) Wang, H. I.; Infante, I.; Brinck, S. ten; Cánovas, E.; Bonn, M. Efficient Hot Electron Transfer in Quantum Dot-Sensitized Mesoporous Oxides at Room Temperature. Nano Lett. 2018, 18 (8), 5111–5115.

(31) Benkö, G.; Kallioinen, J.; Korppi-Tommola, J. E. I.; Yartsev, A. P.; Sundström, V. Photoinduced Ultrafast Dye-to-Semiconductor Electron Injection from Nonthermalized and Thermalized Donor States. J. Am. Chem. Soc. 2002, 124 (3), 489–493.

(32) Furube, A.; Katoh, R.; Yoshihara, T.; Hara, K.; Murata, S.; Arakawa, H.; Tachiya, M. Ultrafast Direct and Indirect Electron-Injection Processes in a Photoexcited Dye-Sensitized Nanocrystalline Zinc Oxide Film: The Importance of Exciplex Intermediates at the Surface. J. Phys. Chem. B 2004, 108 (33), 12583–12592.

(33) Wenger, B.; Grätzel, M.; Moser, J.-E. Rationale for Kinetic Heterogeneity of Ultrafast Light-Induced Electron Transfer from Ru(II) Complex Sensitizers to Nanocrystalline TiO_2. J. Am. Chem. Soc. 2005, 127 (35), 12150–12151.

(34) Cánovas, E.; Wang, H.; Karakus, M.; Bonn, M. Hot Electron Transfer from PbSe Quantum Dots Molecularly Bridged to Mesoporous Tin and Titanium Oxide Films. Chem. Phys. 2016, 471, 54–58.

(35) Smith, N. Classical Generalization of the Drude Formula for the Optical Conductivity. Phys. Rev. B 2001, 64 (15), 155106.

(36) Ulbricht, R.; Hendry, E.; Shan, J.; Heinz, T. F.; Bonn, M. Carrier Dynamics in Semiconductors Studied with Time-Resolved Terahertz Spectroscopy. Rev. Mod. Phys. 2011, 83 (2), 543–586.

(37) Tsokkou, D.; Othonos, A.; Zervos, M. Carrier Dynamics and Conductivity of SnO_2 Nanowires Investigated by Time-Resolved Terahertz Spectroscopy. Appl. Phys. Lett. 2012, 100 (13), 133101.

(38) Regan, K. P.; Swierk, J. R.; Neu, J.; Schmuttenmaer, C. A. Frequency-Dependent Terahertz Transient Photoconductivity of Mesoporous SnO_2 Films. J. Phys. Chem. C 2017, 121 (29), 15949–15956.

(39) Zou, X.; Luo, J.; Lee, D.; Cheng, C.; Springer, D.; Nair, S. K.; Cheong, S. A.; Fan, H. J.; Chia, E. E. M. Temperature-Dependent Terahertz Conductivity of Tin Oxide Nanowire Films. J. Phys. D. Appl. Phys. 2012, 45 (46), 465101.

(40) Asbury, J. B.; Hao, E.; Wang, Y. Q.; Ghosh, H. N.; Lian, T. Q. Ultrafast Electron Transfer Dynamics from Molecular Adsorbates to Semiconductor Nanocrystalline Thin Films. J. Phys. Chem. B 2001, 105 (20), 4545.

(41) Wang, H.; McNellis, E. R.; Kinge, S.; Bonn, M.; Cánovas, E. Tuning Electron Transfer Rates through Molecular Bridges in Quantum Dot Sensitized Oxides. Nano Lett. 2013, 13 (11), 5311–5315.

(42) Hagberg, D. P.; Edvinsson, T.; Marinado, T.; Boschloo, G.; Hagfeldt, A.; Sun, L. A Novel Organic Chromophore for Dye-Sensitized Nanostructured Solar Cells. Chem. Commun. 2006, No. 21, 2245.

(43) Wang, Z.-S.; Sugihara, H. N3-Sensitized TiO_2 Films: In Situ Proton Exchange toward Open-Circuit Photovoltage Enhancement. Langmuir 2006, 22 (23), 9718–9722.

(44) Lin, L.-Y.; Tsai, C.-H.; Wong, K.-T.; Huang, T.-W.; Hsieh, L.; Liu, S.-H.; Lin, H.-W.; Wu, C.-C.; Chou, S.-H.; Chen, S.-H.; et al. Organic Dyes Containing Coplanar Diphenyl-Substituted Dithienosilole Core for Efficient Dye-Sensitized Solar Cells. J. Org. Chem. 2010, 75 (14), 4778–4785.

(45) Nazeeruddin, M. K.; Humphry-Baker, R.; Liska, P.; Grätzel, M. Investigation of Sensitizer Adsorption and the Influence of Protons on Current and Voltage of a Dye-Sensitized Nanocrystalline TiO_2 Solar Cell. J. Phys. Chem. B 2003, 107 (34), 8981–8987.

(46) Cahen, D.; Kahn, A. Electron Energetics at Surfaces and Interfaces: Concepts and Experiments. Adv. Mater. 2003, 15 (4), 271–277.

(47) Gaussian 09, Revision D.01, Frisch, M. J.; Trucks, G. W.; Schlegel, H. B.; Scuseria, G. E.; Robb, M. A.; Cheeseman, J. R.; Scalmani, G.; Barone, V.; Mennucci, B.; Petersson, G. A.; Nakatsuji, H.; Caricato, M.; Li, X.; Hratchian, H. P.; Izmaylov, A. F.; Bloino, J.; Zheng, G.; Sonnenberg, J. L.; Hada, M.; Ehara, M.; Toyota, K.; Fukuda, R.; Hasegawa, J.; Ishida, M.; Nakajima, T.; Honda, Y.; Kitao, O.; Nakai, H.; Vreven, T.; Montgomery, Jr., J. A.; Peralta, J. E.; Ogliaro, F.; Bearpark, M.; Heyd, J. J.; Brothers, E.; Kudin, K. N.; Staroverov, V. N.; Kobayashi, R.; Normand, J.; Raghavachari, K.; Rendell, A.; Burant, J. C.; Iyengar, S. S.; Tomasi, J.; Cossi, M.;Rega, N.; Millam, N. J.; Klene, M.; Knox, J. E.; Cross, J. B.; Bakken, V.; Adamo, C.; Jaramillo, J.; Gomperts, R.; Stratmann, R. E.; Yazyev, O.; Austin, A. J.; Cammi, R.; Pomelli, C.; Ochterski, J. W.; Martin, R. L.; Morokuma, K.; Zakrzewski, V. G.; Voth, G. A.; Salvador, P.; Dannenberg, J. J.; Dapprich, S.; Daniels, A. D.; Farkas, Ö.; Foresman, J. B.; Ortiz, J. V.; Cioslowski, J.; Fox, D. J. Gaussian, Inc., Wallingford CT, 2013.

(48) Baxter, J. B.; Schmuttenmaer, C. A. Conductivity of ZnO Nanowires, Nanoparticles, and Thin Films Using Time-Resolved Terahertz Spectroscopy. J. Phys. Chem. B 2006, 110 (50), 25229-25239.

CHAPTER 4: SIZE-DEPENDENT ELECTRON TRANSFER FROM ATOMICALLY DEFINED NANOGRAPHENES TO METAL OXIDE NANOPARTICLES

4.1 Introduction and aim of the work

Sensitized metal oxides (MOs) represent a very relevant geometry for the development of solar energy conversion schemes (e.g. solar cell and fuel devices). In these architectures, the sensitizers, acting as photon absorbers, enable the metal oxide to harvest photogenerated charge carriers below its generally wide insulating bandgap. In sensitized systems, an exciton is generated within the sensitizer after the absorption of a photon. The photogenerated exciton can then be dissociated at the sensitizer/MO interface following an electron transfer (ET) process from the sensitizer donor to the MO acceptor. Once the electron is populating the MO oxide, it can either be extracted to an external circuit (in solar cells) or trigger chemical reactions at the MO surface (in solar fuels). From this simple description, it is clear that kinetic competition at the sensitizer/MO interfaces determines photoconversion efficiency in related devices, an aspect that has been readily and widely acknowledged for MOs sensitized by molecular dyes[1–3] and colloidal inorganic QDs[4,5]. The choice of a sensitizer for functionalizing a given MO is critical towards photoconversion efficiency and must fulfill, generally speaking, several requirements; the absorption onset for the sensitizer should maximize charge carrier generation upon light irradiation (e.g. an absorption onset of ~1.4eV under broadband solar irradiation[6,7]); the sensitizer/MO interfacial energetics should allow for efficient donor-to-acceptor charge transfer[8]; the sensitizer should be unaffected by photodegradation[9], and should ideally be made of abundant and non-toxic elements[7]. To date, the most widely analyzed sensitizers exploited in solar cell and fuel geometries are ruthenium-based organometallic dyes[10] and colloidal inorganic quantum dots (CQDs)[11,12]. CQDs are characterized by larger extinction coefficients when

compared with Ru-based dyes, enabling thinner devices and hence reducing device costs. Importantly, and unique to CQDs, their optoelectronic properties can be readily tuned by controlling their morphology and chemistry[13] (e.g. absorption onset and workfunction). A drawback of CQDs, contrasting molecular dyes, is the requirement for surface passivation schemes[13], complicating sensitizer/MO interfacial chemistry and introducing non-radiative recombination pathways within the sensitizer, which lower the photo-conversion efficiency. An ongoing difficult-to-bypass issue regarding both sensitizers (Ru-based dyes and CQDs) refer to the employment of toxic and scarce materials on their synthesis, an aspect with a direct impact on their cost and their eventual commercialization. Relatively recently, nano-graphenes (NGRs), polycyclic aromatic hydrocarbons, also referred to as graphene quantum dots, have been introduced as an appealing alternative to conventional sensitizers[14–16]. NGRs, while being metal-free molecular sensitizers, display larger extinction coefficients when compared with conventional dyes[17]. Notably NGRs, defined by atomically precise structures, feature finite size-dependent energy gaps induced by quantum confinement effects[18–20] (as in inorganic CQDs). Furthermore, apart from the exquisite control that can be achieved over their sizes, edge structures of NGRs can be also tailored and even functionalized[18,19]; factors that further allow for fine-tuning of their optoelectronic properties. [21–24]. These combined features make NGRs very appealing candidates as sensitizers of MO electrodes.

Despite the prominent relevance of NGR/MO interfaces for developing novel solar energy conversion architectures, to date, little information is available regarding the fundamentals of ET process from NGR donors to MO acceptors (that, as stated previously, do determine the photoconversion efficiency in related devices). In this communication, we analyze the interplay between the size of atomically precise NGRs and related ET dynamics at NGR/MO interfaces. We resolve that as the size of NGR decreases, the ET rates between the NGR donor and MO acceptor become faster, a result that is rationalized within the Marcus theory framework. These results demonstrate that the selection of a given size of NGR sensitizer (with a given absorption onset) does have a critical role on ET process efficiency, the latter being determined by the kinetic competition between ET towards the oxide electrode and competing decay channels at the NGR/MO interface (e.g. NGR radiative recombination).

4.2 Methods

4.2.1 Materials

The set of molecular NGRs structures used in this study are summarized in Figure 4.1. The samples are labeled as *C#/R* (where *C#* denotes the number of carbons contained in the core structure and *R* the number of fused rings).

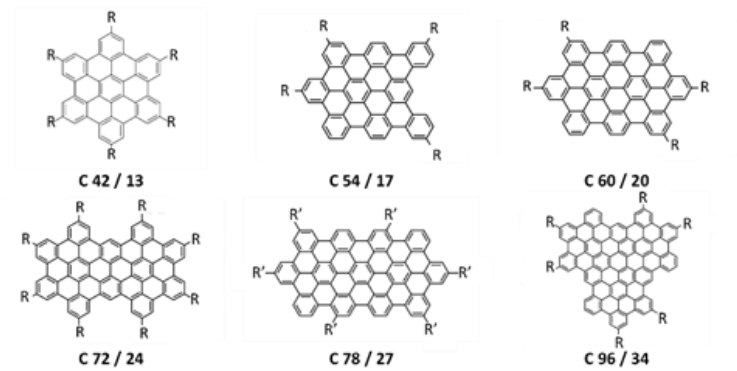

Figure 4.1. Chemical structures of the NGRs analyzed in this work. The samples are labeled as C#/R, where # denotes the number of carbons contained in the core structure and R the number of fused rings. –R and –R' refer to $–C_{12}H_{25}$ and $–C(CH_3)_3$ respectively.

4.2.2 Synthesis

These NGRs were synthesized through oxidative cyclodehydrogenation of corresponding, tailor-made polyphenylene precursors, following our previous procedures[19,25–29].

Mesoporous metal oxide films (~10 µm thick) consisting of SnO_2 nanopowders (≤100 nm average particle size, Sigma-Aldrich ref# 549657) deposited onto 1 mm thick fused silica substrates were prepared by the doctor blading technique and sintered at 450 ℃ for 3 h. The resulting MO films were sensitized with NGRs with different sizes by immersing them for 12 h in dispersions of NGRs in toluene. The films were subsequently rinsed several times in toluene to remove excess of NGRs not adsorbed to the MO surface.

4.2.3 Characterization

ET rates in these films were characterized by OPTP spectroscopy introduced in Chapter 2; the measurements were performed under nitrogen conditions to prevent any potential sensitizer photo-oxidation. Apart from THz spectroscopy, UV-VIS absorbance spectroscopy, photoluminescence spectroscopy as well as gas-phase density functional theory (DFT) calculation were employed in order to estimate the size dependent HOMO-LUMO energy gap in the set of NGRs as well as the driven forces for electron injection via two ET channels. For more details regarding these characterization techniques, please see the Appendix.

4.3 Results and discussion

4.3.1 Size-dependent HOMO-LUMO gaps in NGRs

Figure 4.2 shows as square open dots, the dependence of HOMO-LUMO gaps ($\Delta E_{H\text{-}L}$) as a function of NGR number of fused rings (i.e. NGR size), inferred from absorption measurements for the analyzed set of samples dispersed in toluene (see Appendix), Figure 4.2 also presents, as blue open stars, the theoretical estimates calculated from ZINDO/S on NGRs with 100% compactness[18]. The results are consistent with the dependence expected for a quantum-mechanical particle in a two-dimensional box, where the energies scale with the area of the box; in this case the number of fused rings *R*. A global fit to all the data (including open stars and squares) provides an overall relationship between PAH HOMO-LUMO gap and number of fused carbon rings of $\Delta E_{H\text{-}L}=5.46(\pm0.2)R^{-0.30(\pm0.01)}$, in very good agreement with theoretical estimates[18,30–32].

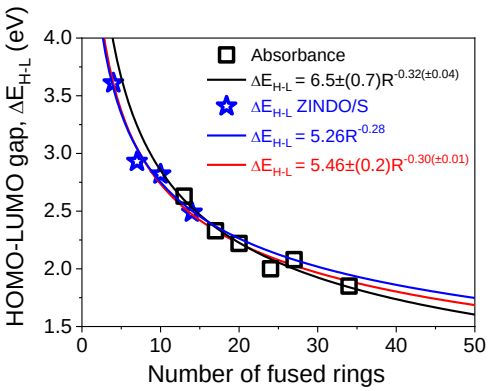

Figure 4.2. HOMO-LUMO gap inferred from absorption spectra, as black open squares, as a function of number of fused carbon rings for the samples sketched in panel a (dispersed in toluene). The theoretical estimates calculated from ZINDO/S on NGRs with 100% compactness[18] are shown as blue open stars. The fits for data inferred from absorption spectra, that estimated by calculation as well as a global fit for all the data are demonstrated as solid lines in black, blue and red respectively.

4.3.2 OPTP characterization

We and others have previously demonstrated the unique suitability of OPTP spectroscopy to quantify ultrafast interfacial ET dynamics in dye-[9,33–36] and QD-[37–39] sensitized oxide systems. OPTP is capable of time-resolving the evolution of the photoconductivity of a given system following above-bandgap optical excitation with sub-ps resolution and in a contactless fashion[40]. The ~2 THz bandwidth probe pulse is primarily sensitive to free carrier motion (i.e. photoconductivity, $\sigma = q \cdot N \cdot \mu$, where q is the electron charge, N the number of absorbed photons and μ the mobility of photogenerated carriers). The OPTP signal is insensitive to excitons in NGRs and therefore neatly probes the emergence of photoconductivity in the MO electrode after selective optical excitation of the sensitizer: OPTP traces the arrival of electrons from the sensitizer's populated molecular orbitals (e.g. LUMO) into the oxide's conduction band (CB); that is, it resolves unambiguously the ET process from the NGR donor to the MO acceptor.

Figure 4.3(a) shows normalized OPTP dynamics for the samples analyzed in this study. The samples were excited at 400 nm with a fluence of 40 μJ/cm^2. This fluence ensured single excitation in NGRs; the wavelength ensured selective excitation of NGRs. No OPTP response was observed for a bare mesoporous SnO_2

film, demonstrating that the signal presented in figure 4.3(a) only reflects ET from the NGR donor to the MO acceptor. As evident from figure 4.3(a), the sensitization of mesoporous SnO_2 by the NGRs sensitizers - physisorbed at the oxide surface [41] – provides biphasic dynamics in all the cases. As such, all the OPTP line traces can be very well described by a bi-exponential ET model (solid lines in figure 4.3(a)). A summary of the inferred ET rate constants as a function of NGR number of fused carbon rings is shown in figure 4.3(b) (black open circles and blue open diamonds representing the fast and slow ET rate constants for each sensitizer). From the plot it is clear that ET dynamics are slowed down as the NGR size increases; this applies to both rate constants (the fast and slow components). Qualitatively, this result can be rationalized by taking into account that reduced NGR sizes are characterized by larger optical energy gaps, this feature promotes larger excess energy offsets between donating and accepting states at the NGR/MO interface (that is larger driving energy for ET, generally denoted as ΔG). Such dependence, which has been previously reported in other MO systems sensitized with dyes[42–44] and inorganic colloidal quantum dots[39,45], can be modeled using the Marcus theory framework (see below). On the other hand, biphasic ET dynamics has been as well widely reported for dye- and QD-sensitized oxide systems[43,46–51], and in a recent paper by us analyzing the role of physisorption and chemisorption at NGRs/MO interfaces [41]. Biphasic dynamics indicate two distinct transfer channels from the NGRs towards the oxide electrode. In the following, we discuss the bi-phasic nature of the process.

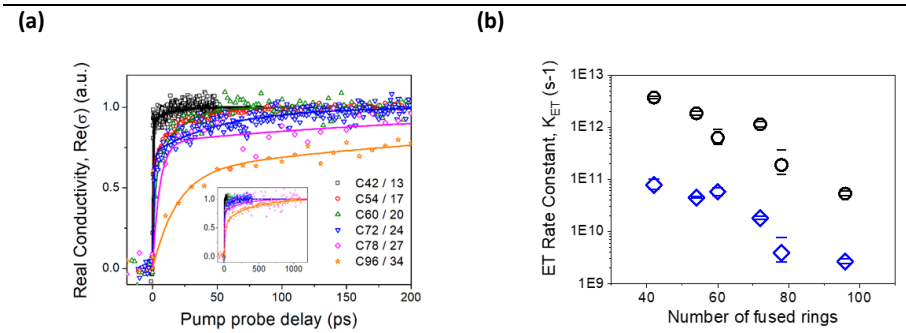

Figure 4.3. (a) Normalized OPTP dynamics from different sized NGRs to the MO electrode. Solid lines are bi-exponential fits. The inset show the same kinetics over a 1 ns time window. (b) ET rate constants vs the number of NGR fused rings for the fast (black dots) and slow (blue dots) kinetic components.

Our previous work analyzing ET rates on colloidal inorganic quantum dots (CQDs) sensitizing the same MO electrode (Sigma-Aldrich, ref# 549657) revealed that ET from the CQD LUMO to the MO was always well-characterized by a monophasic ET component for systems where intra-band CQD relaxation within the sensitizer was kinetically faster than ET towards the oxide[39,52]. When CQD hot-electron intra-band relaxation was kinetically competing with ET, biphasic ET dynamics were obtained from, respectively, hot and cold electrons populating the sensitizer[37,53]. The relative weight of hot and cold ET was shown to be determined by CQD intra-band relaxation kinetics. Beyond inorganic CQDs, hot and cold ET has also been reported in dye/MO systems[44,54], and has been related by several authors, in first approximation, with the presence of a frequency offset between dye absorption and emission. [55,56]. An energy onset between absorption and emission implies that, after photon absorption in the NGR, there is substantial energy relaxation within the sensitizer prior to radiative emission; the relative speed of this intramolecular relaxation process vs ET towards the oxide will determine whether hot ET towards the MO is possible in a given system. All NGRs in this work exhibit a large Stokes shift (see Appendix). This aspect alone supports the scenario where ET toward the MO is taking place from hot and cold states in the analyzed NGRs. Furthermore, this hypothesis is consistent with previous reports analyzing carrier dynamics on NGRs, where carrier cooling has been reported to be rather slow (with hot-electron lifetimes as long as ~100 ps for C132 / 48 NGRs[57]). Hot electrons in NGRs do have a large probability of relaxing into triplet states and emitting both phosphorescence and fluorescence at room temperature[57–59]. Indeed, the long lifetimes of hot carriers in NGRs have allowed researchers to demonstrate efficient sub-ps hot-electron transfer in C132 NGR sensitizing a planar TiO_2(110) rutile surface[60].

Taking into account the above discussion, we rationalize the presence of slow and fast components in NGR/MO interfacial OPTP dynamics with cold and hot ET components inherently linked to each NGR sensitizer. That is, cold ET can take place from the LUMO state and hot ET from higher-lying electronic states in the NGR.

4.3.3 Marcus theory interpretation

Assuming that the bi-phasic nature of the process is linked with hot and cold ET channels, we model our results within the Marcus theory framework.

Following this model, the rate constant (k_{ET}) between a localized donor state towards an accepting continuum of states can be expressed as Eqn.1.2[43]: where the ET rate for a given temperature (T) is defined by : 1) ΔG, the energy difference between donating state and the bottom of the accepting MO conduction band, commonly referred as the ET driven force; 2) $|\widehat{H}(E)|^2$, the coupling strength, which reflects the wavefunction overlap between donor and acceptor states; 3) $\rho(E)$, the density of states in the conduction band of the acceptor; and 4) λ, the reorganizational energy that accounts for energy fluctuations in the systems due to charge transfer. To model the kinetic data presented in figure 4.3(b) by Eqn.1.2, we make some approximations. The density of MO accepting states is assumed to follow an $E^{1/2}$ dependence. The wave function overlap $|\widehat{H}(E)|^2$ between donating and accepting states is assumed to follow a quadratic relationship with energy. This assumption, previously employed in inorganic CQDs sensitizing MOs[39], takes into account that the electron wave function leakage outside the sensitizer follows a quadratic relationship with energy[39]. Finally, for the NGR/MO systems analyzed in this work, ΔG can be obtained as the difference in workfunction of the donating NGR orbital and the bottom of the MO CB. Assuming that our bi-phasic ET dynamics refer to hot and cold ET channels, we need then to define ΔG_{cold} and ΔG_{hot} for each sensitizer. For the fast component, ΔG_{hot} is inferred as the energy difference between NGR LUMO ground state absorption (inferred from gas phase DFT, see Appendix) and the SnO_2 CB workfunction (estimated from ultraviolet photoelectron spectroscopy[41]). For the slow component, we infer ΔG_{cold} as ΔG_{hot}-E_{em}^{onset}, where E_{em}^{onset} refers to the energy onset where radiative emission takes place for each given NGR size (see inset in figure 4.4 and Appendix). Figure 4.4 summarizes the resolved ET rate constants (for hot and cold components) as a function of inferred ΔGs.

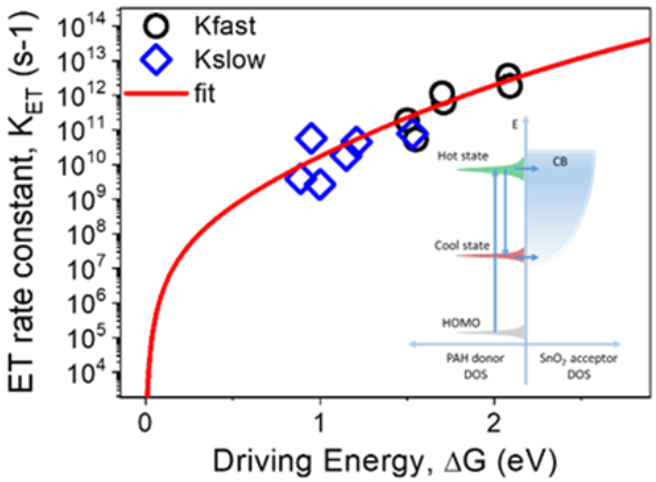

Figure 4.4. ET rate constants as a function of the driving energy -ΔG, the energy difference between donating an accepting state: fast component (black dots); slow component (red dots). A schematic of injecting electron from hot and cold ET channels respectively in this system is shown in the inset.

The red line in figure 4.4 represents the best fit to the data by Eqn.1.2. Apart from a scaling factor, the only fitting parameter in Eqn.1.2 is the reorganizational energy, which is found to be λ=1±50 meV for the analyzed system. This small figure is in good agreement with the results obtained from similar results for inorganic CQDs sensitizing MOs[39,48], and implies that vibronic and solvation effects under our experimental conditions do have a negligible effect on ET. Overall, and taking into account the approximations made, we conclude that the obtained fit describes the experimental data fairly well, suggesting the validity of Marcus model for describing ET at NGR/MO interfaces.

4.4 Summary

In summary, size-dependent ET rates from nanographenes to metal oxide nanoparticles reveals two ET channels, which are rationalized by hot and cold ET channels. The dependence of ET rates on NGR size can be reasonably well described by Marcus theory, where ET rates become faster as NGR size is reduced (i.e. as the energy gap of the NGRs become larger). Regarding the exploitation of

NGR/MO interfaces in photocatalytic and photovoltaic devices, it is worth commenting that faster ET processes enabled by smaller NGRs (larger bandgaps and then ΔG over-potentials) will not necessarily be the best recipe. First, in order to boost charge carrier collection under solar illumination, one should select larger NGR sizes which are defined by smaller gaps, with an optimum of 1.4eV following the Shockley-Queisser limit (that is for NGRs made of ~50 fused rings, see fig.4.1). However, as evident from our results, larger NGRs exhibit lower ET rates (K_{ET}) that might eventually compete with radiative relaxation (K_{rad}) within the NGRs, thereby reducing the electron collection efficiency. Clearly, a compromise between absorption onset and NGR/MO interfacial ET must be found; the optimum will be defined by the NGR revealing the narrowest HOMO-LUMO gap while keeping $K_{ET} >> K_{rad}$.

4.5 Appendix

I acknowledge here the contribution of Prof. Klaus Müllen and Dr. Akimitsu Narita for NGR sample preparation, UV-VIS absorption measurement, Fluorescence measurement as well as first-principle calculation.

4.5.1 Extracting HOMO-LUMO gaps from absorption measurements of nPAHs dispersed in the Toluene

For each analyzed PAH sample, the difference of LUMO and HOMO levels, i.e. $\Delta E_{H\text{-}L}$ was extracted from the onset of absorption spectrum for corresponding size dispersed in the toluene as shown as black lines in Fig.4.5. A summary of all extracted results was listed in Table 4.1. Those results were plotted as data points in Fig.4.2.

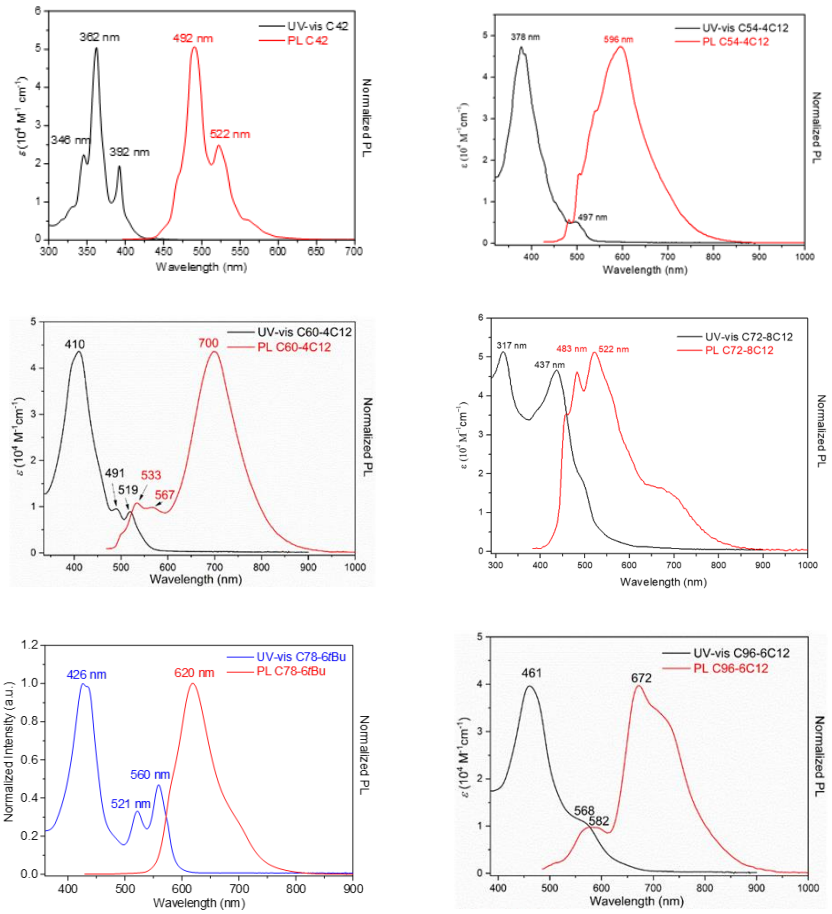

Figure 4.5. Absorption and Fluorescence spectrum for all analyzed set of PAH samples dispersed in toluene. See details of the molecular formulae in the context of manuscript. For all analyzed PAHs a strong Stokes shift is revealed while comparing their absorption and emission spectra.

Table 4.1. Absorption onset energy (E_{abs}^{onset}), emission onset energy (E_{emi}^{onset}), energy of stoke shift (E_{stoke}) and HOMO-LUMO gap ($\Delta E_{H\text{-}L}$) of PAH sample with all analyzed sizes inferred from the corresponding absorption spectrum

	C42	**C54**	**C60**	**C72**	**C78**	**C96**
$\boldsymbol{E_{abs}^{onset}}$**(eV)**	2.63	2.33	2.22	2	2.08	1.85
$\boldsymbol{E_{emi}^{onset}}$**(eV)**	2.08	1.45	1.46	1.43	1.47	1.3
$\boldsymbol{E_{stoke}}$**(eV)**	0.55	0.88	0.76	0.57	0.61	0.55
$\boldsymbol{\Delta E_{H\text{-}L}}$ **(eV)**	2.63	2.33	2.22	2	2.08	1.85

4.5.2 Extracting driven force for hot ET process as the difference of LUMO PAH levels (inferred from gas phase DFT) and SnO_2 CB edge level

The energy difference between hot donating state and the bottom of the accepting MO conduction band, i.e. ET driven force for hot process, ΔG_{hot} was extracted by subtracting from the energy of LUMO level for each analyzed PAH determined from the DFT calculation in the gas phase (see Fig. 4.6 and Table. 4.2), the energy of CB edge level for SnO_2 determined from the ultraviolet photoelectron spectrum of pure SnO_2 mesoporous film measured previously (see supporting information of reference 41). This was done by assuming the change of ΔG_{hot} is negligible to affect the ET rate constants before and after sensitization. Given the weaker coupling induced by the physical absorption of those PAHs onto the surface of oxides this is most likely valid. Inputting E_{CBM} = -3.74 eV for SnO_2, our estimated ΔG_{hot} for all analyzed sets of PAH samples were listed in Table 4.2.

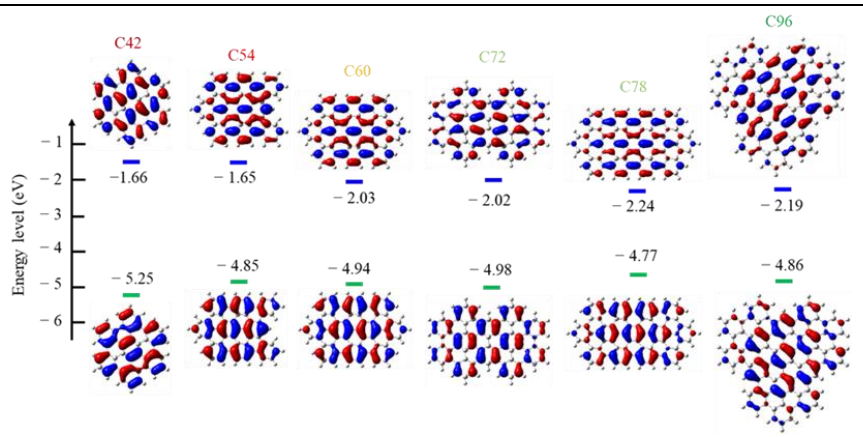

Figure 4.6. Energy and the conformation of frontier orbitals for all analyzed set of PAH samples calculated from the DFT in the gas phase. The blue and green lines represent the states of LUMO and HOMO respectively. All energy values employ vacuum energy as the reference, i.e. E_{vac}=0 eV.

Table 4.2. Calculated energy of LUMO (E_{LUMO}), HOMO (E_{HOMO}) levels, HOMO-LUMO gap ($\Delta E_{H\text{-}L}$) and hot ET driven force (ΔG_{hot}) for all analyzed sets of PAH samples evaluated from the DFT in the gas phase

	C42	**C54**	**C60**	**C72**	**C78**	**C96**
Δ_{LUMO}(eV)	-1.66	-1.65	-2.03	-2.02	-2.24	-2.19
Δ_{HOMO}(eV)	-5.25	-4.85	-4.94	-4.98	-4.77	-4.86
$\Delta E_{H\text{-}L}$ (eV)	3.59	3.20	2.91	2.96	2.53	2.67
ΔG_{hot} (eV)	2.08	2.09	1.71	1.72	1.50	1.55

4.5.3 Extracting driven force for cool ET process by considering the stokes shift for PAHs combining absorption and emission spectrum

The energy difference between cold donating state and the bottom of the accepting MO conduction band, i.e. ET driven force for cool process, ΔG_{cold} was estimated by subtracting from ΔG_{hot} the energy of corresponding stokes shift, E_{stokes} for each analyzed PAH (see Table 4.1). E_{stokes} was difference of energy between the onset of absorption and emission spectrum for each PAH in Fig.4.5, i.e. $E_{stokes} = E_{abs}^{onset} - E_{emi}^{onset}$. Resulting ΔG_{cold} for all analyzed sets of PAH samples were listed in Table 4.3.

Table 4.3. Calculated cool ET driven force (ΔG_{cold}) for all analyzed sets of PAH samples

	C42	**C54**	**C60**	**C72**	**C78**	**C96**
ΔG_{cold} (eV)	1.53	1.21	0.95	1.15	0.89	1

References

(1) Bangle, R. E.; Meyer, G. J. Factors That Control the Direction of Excited-State Electron Transfer at Dye-Sensitized Oxide Interfaces. J. Phys. Chem. C 2019, 123 (42), 25967–25976.

(2) Soroush, M.; Lau, K. K. S. Dye-Sensitized Solar Cells : Mathematical

Modelling, and Materials Design and Optimization; 2019.

(3) Nazeeruddin, M. K.; Baranoff, E.; Grätzel, M. Dye-Sensitized Solar Cells: A Brief Overview. Sol. Energy 2011, 85 (6), 1172–1178.

(4) Sargent, E. H. Colloidal Quantum Dot Solar Cells. Nat. Photonics 2012, 6 (3), 133–135.

(5) Dong, H.; Xu, F.; Sun, Z.; Wu, X.; Zhang, Q.; Zhai, Y.; Tan, X. D.; He, L.; Xu, T.; Zhang, Z.; et al. In Situ Interface Engineering for Probing the Limit of Quantum Dot Photovoltaic Devices. Nat. Nanotechnol. 2019, 14 (10), 950–956.

(6) Walter, M. G.; Warren, E. L.; McKone, J. R.; Boettcher, S. W.; Mi, Q.; Santori, E. A.; Lewis, N. S. Solar Water Splitting Cells. Chem. Rev. 2010, 110 (11), 6446–6473.

(7) Hagfeldt, A.; Boschloo, G.; Sun, L.; Kloo, L.; Pettersson, H. Dye-Sensitized Solar Cells. Chem. Rev. 2010, 110 (11), 6595–6663.

(8) Listorti, A.; O'Regan, B.; Durrant, J. R. Electron Transfer Dynamics in Dye-Sensitized Solar Cells. Chem. Mater. 2011, 23 (15), 3381–3399.

(9) Karakus, M.; Zhang, W.; Räder, H. J.; Bonn, M.; Cánovas, E. Electron Transfer from Bi-Isonicotinic Acid Emerges upon Photodegradation of N3-Sensitized TiO_2 Electrodes. ACS Appl. Mater. Interfaces 2017, 9 (40), 35376–35382.

(10) Qin, Y.; Peng, Q. Ruthenium Sensitizers and Their Applications in Dye-Sensitized Solar Cells. Int. J. Photoenergy 2012, 2012, 1–21.

(11) Kramer, I. J.; Sargent, E. H. Colloidal Quantum Dot Photovoltaics: A Path Forward. ACS Nano 2011, 5 (11), 8506–8514.

(12) Konstantatos, G.; Sargent, E. H. Colloidal Quantum Dot Optoelectronics and Photovoltaics; Konstantatos, G., Sargent, E. H., Eds.; Cambridge University Press: Cambridge, 2013; Vol. 9780521198.

(13) Zhong, H.; Bai, Z.; Zou, B. Tuning the Luminescence Properties of Colloidal I–III–VI Semiconductor Nanocrystals for Optoelectronics and Biotechnology Applications. J. Phys. Chem. Lett. 2012, 3 (21), 3167–3175.

(14) Majumder, T.; Dhar, S.; Debnath, K.; Mondal, S. P. Role of S, N Co-Doped

Graphene Quantum Dots as a Green Photosensitizer with Ag-Doped ZnO Nanorods for Improved Electrochemical Solar Energy Conversion. Mater. Res. Bull. 2017, 93, 214–222.

(15) Kundu, S.; Sarojinijeeva, P.; Karthick, R.; Anantharaj, G.; Saritha, G.; Bera, R.; Anandan, S.; Patra, A.; Ragupathy, P.; Selvaraj, M.; et al. Enhancing the Efficiency of DSSCs by the Modification of TiO_2 Photoanodes Using N, F and S, Co-Doped Graphene Quantum Dots. Electrochim. Acta 2017, 242, 337–343.

(16) Zhang, Y.; Qi, F.; Li, Y.; Zhou, X.; Sun, H.; Zhang, W.; Liu, D.; Song, X.-M. Graphene Oxide Quantum Dot-Sensitized Porous Titanium Dioxide Microsphere: Visible-Light-Driven Photocatalyst Based on Energy Band Engineering. J. Colloid Interface Sci. 2017, 498, 105–111.

(17) Yan, X.; Cui, X.; Li, B.; Li, L.-S. Large, Solution-Processable Graphene Quantum Dots as Light Absorbers for Photovoltaics. Nano Lett. 2010, 10 (5), 1869–1873.

(18) Ruiz-Morales, Y. HOMO-LUMO Gap as an Index of Molecular Size and Structure for Polycyclic Aromatic Hydrocarbons (PAHs) and Asphaltenes: A Theoretical Study. I. J. Phys. Chem. A 2002, 106 (46), 11283–11308.

(19) Dötz, F.; Brand, J. D.; Ito, S.; Gherghel, L.; Müllen, K. Synthesis of Large Polycyclic Aromatic Hydrocarbons: Variation of Size and Periphery. J. Am. Chem. Soc. 2000, 122 (32), 7707–7717.

(20) Malloci, G.; Cappellini, G.; Mulas, G.; Mattoni, A. Electronic and Optical Properties of Families of Polycyclic Aromatic Hydrocarbons: A Systematic (Time-Dependent) Density Functional Theory Study. Chem. Phys. 2011, 384 (1–3), 19–27.

(21) Song, S. H.; Jang, M.-H.; Chung, J.; Jin, S. H.; Kim, B. H.; Hur, S.-H.; Yoo, S.; Cho, Y.-H.; Jeon, S. Highly Efficient Light-Emitting Diode of Graphene Quantum Dots Fabricated from Graphite Intercalation Compounds. Adv. Opt. Mater. 2014, 2 (11), 1016–1023.

(22) Wang, Z.; Yuan, F.; Li, X.; Li, Y.; Zhong, H.; Fan, L.; Yang, S. 53% Efficient Red Emissive Carbon Quantum Dots for High Color Rendering and Stable Warm White-Light-Emitting Diodes. Adv. Mater. 2017, 29 (37), 1702910.

(23) Dutta, M.; Sarkar, S.; Ghosh, T.; Basak, D. ZnO/Graphene Quantum Dot

Solid-State Solar Cell. J. Phys. Chem. C 2012, 116 (38), 20127–20131.

(24) Zhang, B. Y.; Liu, T.; Meng, B.; Li, X.; Liang, G.; Hu, X.; Wang, Q. J. Broadband High Photoresponse from Pure Monolayer Graphene Photodetector. Nat. Commun. 2013, 4.

(25) Tomović, Ž.; Watson, M. D.; Müllen, K. Superphenalene-Based Columnar Liquid Crystals. Angew. Chemie Int. Ed. 2004, 43 (6), 755–758.

(26) Böhme, T.; Simpson, C. D.; Müllen, K.; Rabe, J. P. Current–Voltage Characteristics of a Homologous Series of Polycyclic Aromatic Hydrocarbons. Chem. - A Eur. J. 2007, 13 (26), 7349–7357.

(27) Wasserfallen, D.; Kastler, M.; Pisula, W.; Hofer, W. A.; Fogel, Y.; Wang, Z.; Müllen, K. Suppressing Aggregation in a Large Polycyclic Aromatic Hydrocarbon. J. Am. Chem. Soc. 2006, 128 (4), 1334–1339.

(28) Iyer, V. S.; Yoshimura, K.; Enkelmann, V.; Epsch, R.; Rabe, J. P.; Müllen, K. A Soluble C60 Graphite Segment. Angew. Chemie Int. Ed. 1998, 37 (19), 2696–2699.

(29) Stabel, A.; Herwig, P.; Müllen, K.; Rabe, J. P. Diodelike Current–Voltage Curves for a Single Molecule–Tunneling Spectroscopy with Submolecular Resolution of an Alkylated,Peri-Condensed Hexabenzocoronene. Angew. Chemie Int. Ed. English 1995, 34 (15), 1609–1611.

(30) Li, H.; He, X.; Kang, Z.; Huang, H.; Liu, Y.; Liu, J.; Lian, S.; Tsang, C. H. A.; Yang, X.; Lee, S. T. Water-Soluble Fluorescent Carbon Quantum Dots and Photocatalyst Design. Angew. Chemie - Int. Ed. 2010, 49 (26), 4430–4434.

(31) Güçlü, A. D.; Potasz, P.; Hawrylak, P. Excitonic Absorption in Gate-Controlled Graphene Quantum Dots. Phys. Rev. B 2010, 82 (15), 155445.

(32) Eda, G.; Lin, Y. Y.; Mattevi, C.; Yamaguchi, H.; Chen, H. A.; Chen, I. S.; Chen, C. W.; Chhowalla, M. Blue Photoluminescence from Chemically Derived Graphene Oxide. Adv. Mater. 2010, 22 (4), 505–509.

(33) Turner, G. M.; Beard, M. C.; Schmuttenmaer, C. A. Carrier Localization and Cooling in Dye-Sensitized Nanocrystalline Titanium Dioxide. J. Phys. Chem. B 2002, 106 (45), 11716–11719.

(34) Tiwana, P.; Docampo, P.; Johnston, M. B.; Snaith, H. J.; Herz, L. M. Electron Mobility and Injection Dynamics in Mesoporous ZnO, SnO_2 , and

TiO_2 Films Used in Dye-Sensitized Solar Cells. ACS Nano 2011, 5 (6), 5158–5166.

(35) Tiwana, P.; Parkinson, P.; Johnston, M. B.; Snaith, H. J.; Herz, L. M. Ultrafast Terahertz Conductivity Dynamics in Mesoporous TiO_2 : Influence of Dye Sensitization and Surface Treatment in Solid-State Dye-Sensitized Solar Cells. J. Phys. Chem. C 2010, 114 (2), 1365–1371.

(36) Brauer, J. C.; Moser, J.-E. Transient Photoconductivity of Dye-Sensitized TiO_2 Nanocrystalline Films Probed by Optical Pump-THz Probe Spectroscopy. Ultrafast Phenom. XVII 2011, 358–360.

(37) Wang, H.; Barceló, I.; Lana-Villarreal, T.; Gómez, R.; Bonn, M.; Cánovas, E. Interplay Between Structure, Stoichiometry, and Electron Transfer Dynamics in SILAR-Based Quantum Dot-Sensitized Oxides. Nano Lett. 2014, 14 (10), 5780–5786.

(38) Zhao, K.; Pan, Z.; Mora-Sero, I.; Canovas, E.; Wang, H.; Song, Y.; Gong, X.; Wang, J.; Bonn, M.; Bisquert, J.; et al. Boosting Power Conversion Efficiencies of Quantum-Dot-Sensitized Solar Cells Beyond 8% by Recombination Control. J. Am. Chem. Soc. 2015, 137 (16), 5602–5609.

(39) Cánovas, E.; Moll, P.; Jensen, S. A.; Gao, Y.; Houtepen, A. J.; Siebbeles, L. D. A.; Kinge, S.; Bonn, M. Size-Dependent Electron Transfer from PbSe Quantum Dots to SnO_2 Monitored by Picosecond Terahertz Spectroscopy. Nano Lett. 2011, 11 (12), 5234–5239.

(40) Ulbricht, R.; Hendry, E.; Shan, J.; Heinz, T. F.; Bonn, M. Carrier Dynamics in Semiconductors Studied with Time-Resolved Terahertz Spectroscopy. Rev. Mod. Phys. 2011, 83 (2), 543–586.

(41) Han, P.; Hou, I. C.-Y.; Lu, H.; Wang, X.-Y.; Müllen, K.; Bonn, M.; Narita, A.; Cánovas, E. Chemisorption of Atomically Precise 42-Carbon Graphene Quantum Dots on Metal Oxide Films Greatly Accelerates Interfacial Electron Transfer. J. Phys. Chem. Lett. 2019, 1431–1436.

(42) Anderson, N. A.; Lian, T. Ultrafast Electron Transfer At the Molecule-Semiconductor Nanoparticle Interface. Annu. Rev. Phys. Chem. 2005, 56 (1), 491–519.

(43) Asbury, J. B.; Hao, E.; Wang, Y.; Ghosh, H. N.; Lian, T. Ultrafast Electron Transfer Dynamics from Molecular Adsorbates to Semiconductor

Nanocrystalline Thin Films. J. Phys. Chem. B 2001, 105 (20), 4545–4557.

(44) Ziółek, M.; Cohen, B.; Yang, X.; Sun, L.; Paulose, M.; Varghese, O. K.; Grimes, C. A.; Douhal, A. Femtosecond to Millisecond Studies of Electron Transfer Processes in a Donor-(π-Spacer)-Acceptor Series of Organic Dyes for Solar Cells Interacting with Titania Nanoparticles and Ordered Nanotube Array Films. Phys. Chem. Chem. Phys. 2012, 14 (8), 2816–2831.

(45) Robel, I.; Kuno, M.; Kamat, P. V. Size-Dependent Electron Injection from Excited CdSe Quantum Dots into TiO_2 Nanoparticles. J. Am. Chem. Soc. 2007, 129 (14), 4136–4137.

(46) Žídek, K.; Zheng, K.; Ponseca, C. S.; Messing, M. E.; Wallenberg, L. R.; Chábera, P.; Abdellah, M.; Sundström, V.; Pullerits, T. Electron Transfer in Quantum-Dot-Sensitized ZnO Nanowires: Ultrafast Time-Resolved Absorption and Terahertz Study. J. Am. Chem. Soc. 2012, 134 (29), 12110–12117.

(47) Yang, Y.; Rodríguez-Córdoba, W.; Xiang, X.; Lian, T.; Rodriguez-Cordoba, W.; Xiang, X.; Lian, T. Strong Electronic Coupling and Ultrafast Electron Transfer between PbS Quantum Dots and TiO_2 Nanocrystalline Films. Nano Lett. 2012, 12 (1), 303–309.

(48) Tvrdy, K.; Frantsuzov, P. A.; Kamat, P. V. Photoinduced Electron Transfer from Semiconductor Quantum Dots to Metal Oxide Nanoparticles. Proc. Natl. Acad. Sci. 2011, 108 (1), 29–34.

(49) Milot, R. L.; Moore, G. F.; Crabtree, R. H.; Brudvig, G. W.; Schmuttenmaer, C. A. Electron Injection Dynamics from Photoexcited Porphyrin Dyes into SnO_2 and TiO_2 Nanoparticles. J. Phys. Chem. C 2013, 117 (42), 21662–21670.

(50) Dibbell, R. S.; Youker, D. G.; Watson, D. F. Excited-State Electron Transfer from CdS Quantum Dots to TiO_2 Nanoparticles via Molecular Linkers with Phenylene Bridges. J. Phys. Chem. C 2009, 113 (43), 18643–18651.

(51) Blackburn, J. L.; Selmarten, D. C.; Nozik, A. J. Electron Transfer Dynamics in Quantum Dot/Titanium Dioxide Composites Formed by in Situ Chemical Bath Deposition. J. Phys. Chem. B 2003, 107 (51), 14154–14157.

(52) Wang, H.; McNellis, E. R.; Kinge, S.; Bonn, M.; Cánovas, E. Tuning Electron Transfer Rates through Molecular Bridges in Quantum Dot Sensitized

Oxides. Nano Lett. 2013, 13 (11), 5311–5315.

(53) Wang, H. I.; Infante, I.; Brinck, S. ten; Cánovas, E.; Bonn, M. Efficient Hot Electron Transfer in Quantum Dot-Sensitized Mesoporous Oxides at Room Temperature. Nano Lett. 2018, 18 (8), 5111–5115.

(54) Ardo, S.; Meyer, G. J. Photodriven Heterogeneous Charge Transfer with Transition-Metal Compounds Anchored to TiO_2 Semiconductor Surfaces. Chem. Soc. Rev. 2009, 38 (1), 115–164.

(55) Iwai, S.; Hara, K.; Katoh, R.; Murata, S.; Sugihara, H.; Arakawa, H. Ultrafast Interfacial Charge Separation from the Singlet and Triplet MLCT States of Ru(Bpy)2(Dcbpy) Adsorbed on Nanocrystalline SnO_2 under Applied Bias. In Springer Series in Chemical Physics; 2001; Vol. 66, pp 447–449.

(56) Bräm, O.; Cannizzo, A.; Chergui, M. Ultrafast Fluorescence Studies of Dye Sensitized Solar Cells. Phys. Chem. Chem. Phys. 2012, 14 (22), 7934.

(57) Mueller, M. L.; Yan, X.; Dragnea, B.; Li, L. Slow Hot-Carrier Relaxation in Colloidal Graphene Quantum Dots. Nano Lett. 2011, 11 (1), 56–60.

(58) Mueller, M. L.; Yan, X.; McGuire, J. A.; Li, L.-S. Triplet States and Electronic Relaxation in Photoexcited Graphene Quantum Dots. Nano Lett. 2010, 10 (7), 2679–2682.

(59) Riesen, H.; Wiebeler, C.; Schumacher, S. Optical Spectroscopy of Graphene Quantum Dots: The Case of C132. J. Phys. Chem. A 2014, 118 (28), 5189–5195.

(60) Williams, K. J.; Nelson, C. A.; Yan, X.; Li, L.-S.; Zhu, X. Hot Electron Injection from Graphene Quantum Dots to TiO_2. ACS Nano 2013, 7 (2), 1388–1394.

CHAPTER 5: HIGH-MOBILITY BAND-LIKE CHARGE TRANSPORT IN A SEMICONDUCTING TWO-DIMENSIONAL METAL–ORGANIC FRAMEWORK

5.1 Introduction and aim of the work

Metal-Organic Frameworks (MOFs) represent a class of hybrid materials consisting of metal ions connected by organic ligands[1,2]. The large degree of structural and chemical tunability and long range crystalline order have made MOFs promising materials for a large variety of applications (prominently gas storage[3-7] and separation[8-10] and catalysis[11-13]); however, the insulating character of most MOFs developed to date has prevented these materials to be considered for applications requiring long-range charge transport. The recent discovery of electrically conductive MOFs has hence opened yet other broad areas of potential applications of MOFs in optoelectronics and chemiresistive sensing[14-17].

Since the first report of conductive (0.1 S/cm), π-conjugated, two-dimensional (2D) MOFs based on triphenylene-fused metal-catecholates by Yaghi et al.[18], improved electrical conductivities have been reported. Recently, Dincă et al. reported a novel conductive 2D MOF in which the oxygen atoms in metal-catecholates were replaced with nitrogen atoms, thereby giving rise to triphenylene-fused Ni-bis(diimine) complexes with electrical conductivity as high as ~40 S/cm at room temperature[19,20]. Nishihara and Zhu et al. demonstrated electrical conductivity values of 160 S/cm and 1580 S/cm in 2D MOF films comprising benzene-fused metal-bis(dithiolene) based on Ni[21,22] and Cu[23] complexes, respectively. These conductivities were measured at room temperature using two-probe, four-probe, and van der Pauw methods[24]. In all cases, reducing the temperature of the sample resulted in a decrease of the conductivity, an effect that can be tentatively attributed to a hopping-type thermally activated transport. A recent report by Marinescu et al.[25] revealed an increase in conductivity with decreasing temperature for a Co-based 2D-MOF, albeit only at cryogenic temperatures (<170 K) and for samples lacking a bandgap, i.e., a metal. For temperatures above 170 K, where the sample was

semiconducting, the conventional exponential rise in the resistivity versus temperature was observed and attributed to a hopping-type thermally activated transport mechanism. From these conventional conductivity measurements, it is challenging to address the nature of the transport in semiconducting MOFs. This is primarily because these electrical probes measure the conductivity, which is defined by the product of charge carrier density and mobility that can both vary with temperature. As such, the true nature of charge transport in semiconducting MOFs, e.g. whether a hopping or band-like transport mechanism is operative, has remained unresolved[15,16]. Addressing the fundamentals of charge transport in semiconducting MOFs is essential for furthering MOF design as well as for allowing this class of materials to be exploited in optoelectronic applications.

In this chapter we report a study of MOF conductivity using time-resolved Terahertz spectroscopy (TRTS), an all-optical, contact-free method capable of addressing the nature of charge transport. TRTS provides the high-frequency (0.6-1.6 THz) complex photo-conductivity, which directly reflects the mechanism of charge transport[26]. We study a newly developed, *π-d* conjugated, semiconducting $Fe_3(THT)_2(NH_4)_3$ (THT=2,3,6,7,10,11-hexathioltriphenylene) 2D MOF film made of van der Waals stacked layers. We show that free-standing, porous (surface area of 526 m^2 g^{-1}) thin films of $Fe_3(THT)_2(NH_4)_3$ support band-like charge carrier transport, directly demonstrated from the observed Drude-type complex photo-conductivity. A room temperature mobility of ~220 cm^2/Vs is estimated from TRTS, which represents, to the best of our knowledge, a record mobility in MOFs[15,16]. Notably, this mobility value is independently verified using Hall effect measurements on $Fe_3(THT)_2(NH_4)_3$ 2D MOF samples. The quantitative agreement between inferred THz and Hall mobilities demonstrates that band-like charge carrier transport is operative in the samples in both, the AC and DC limit. The analysis of the temperature dependence for the conductivity from both methods reveals that scattering rates and hence mobilities are primarily limited by impurity scattering so that the inferred mobilities constitute lower limits.

5.2 Methods

5.2.1 Materials

The ligand, 2,3,6,7,10,11-triphenylenehexathiol (THT), was synthesized according to a previously reported protocols[27].

5.2.2 Synthesis of $Fe_3(THT)_2(NH4)_3$ 2D MOF film

$Fe_3(THT)_2(NH4)_3$ 2D MOF film was synthesized by the procedure described below. The metal coordination reactions between THT and iron acetylacetonate ($Fe(acac)_2$) took place at the oil/water interface. An 80-ml cylindrical glass vial (5 cm in diameter) was used as the reaction container. A volume of 20 mL of $Fe(acac)_2/CHCl_3$ solution (0.5 mM) was poured into the vial. Then, 10 mL of water was dropped onto the organic phase to form oil/water interface. THT monomers (1 mM) were dissolved in water along with NH_4OH (0.01 M), and 20 mL of the stocking solution was injected into the top water phase. The reaction system was left undisturbed under Ar for 72 h to obtain a black film at the liquid/liquid interface. After further filtration by Nylon membrane (0.45 μm in pore size) under vacuum, the films were washed by water, dilute HCl, water, chloroform, and acetone. All of the above solutions were bubbled by Ar firstly. The as-prepared thick film (~2 μm in thickness) was then peeled off and transferred onto various substrates (such as a SiO_2/Si wafer), and dried at 60 °C under Ar overnight.

Thinner films were synthesized using the same procedure, where the reaction time was controlled to tune the film thickness from 20 nm to hundreds of nanometers. Once the film appeared at the liquid/liquid interface, the two-phase solution was carefully poured onto the surface of 200 mL water. Then the thin films floated on the water surface and were transferred onto different substrates.

5.2.3 AC conductivity measurements by THz spectroscopy

TRTS techniques introduced in Chapter 2 were employed to study the OPTP dynamics as well as freuquency resolved complex photoconductivity in the $Fe_3(THT)_2(NH_4)_3$ 2D MOF film. To prevent any photo-oxidation of the samples during the measurements, all samples have been measured under nitrogen or vacuum conditions (1.4×10^{-4} mbar).

5.2.4 Hall bar fabrication

The fabrication of Hall-bars on the 2D MOF layer (1.7 μm thick $Fe_3(THT)_2(NH_4)_3$ film) on Si/SiO_2 (300 nm) wafer was performed using cold ablation (Hall geometry shown in Fig. 3.18 and Appendix) via ultrafast laser pulses (LPKF ProtoLaser R, picosecond laboratory micromachining system). The metallic contacts to the Hall-bars were fabricated by electron beam lithography (Raith150 Two), using a

commercially available double layer resist (EL 11 + 950 PMMA A4). The resists were spin coated on the samples at 3000 rpm for 60 seconds, followed by post-baking at 180 °C for 10 minutes. The contacts were defined on the samples with an electron dose of 100 μC/cm^2 at an acceleration voltage of 10 kV and an aperture of 30 μm. The samples were then developed by immersing first in isopropanol (IPA): water (70:30) solution for 45 seconds, followed by 15 seconds dip in IPA and N_2 blow dry. The patterned contacts were deposited with Cr (5 nm) as the adhesive layer at a rate of 2 Å/s and Au (150 nm) at a rate of 5 Å/s using thermal evaporation. After metallization, the lift off process was done using acetone with subsequent washing with IPA and drying in a stream of N_2.

5.2.5 Four-probe conductivity and Hall effect measurements

For Hall Effect measurements we used a cryogenic probe station (Lakeshore Model CPX-VF), equipped with a superconducting magnet system (Lakeshore Model 625) with a vertical magnetic field reaching ±2.5 T. All electrical and Hall measurements were carried out in the dark at a pressure < 6 x 10^{-8} mbar using a parameter analyzer (Agilent 4156C).

5.2.6 DFT modeling

Density-functional theory calculations on the crystal structure of $Fe_3(THT)_2(NH_4)_3$ 2D MOF were carried out within the plane-wave pseudo-potential VASP code. For more information, please see the "Modeling of $Fe_3(THT)_2(NH_4)_3$ layers" section in the Appendix.

5.3 Results and discussion

5.3.1 Synthesis and sample characterization

2D MOF $Fe_3(THT)_2(NH_4)_3$ films was synthesized by an interfacial method[21,27,28] where aqueous and $CHCl_3$ phases host THT and iron precursors, respectively. A spontaneous reaction at the $CHCl_3$/water interface under argon at room temperature results in the formation of large-area free-standing multilayer film, free of steps or cracks (Fig. 5.4). The film thickness is tunable by the reaction time (~2 μm for 72 reaction hours as shown in Fig. 5.1(a)). Transmission electron

microscopy (TEM) reveals that the samples are composed of 10-100's of nm crystalline domains (Fig. 5.5(a) and (b)). A honeycomb structure with a pore size of ~1.9 nm was observed by high-resolution TEM (Fig. 5.1(b) and Fig. 5.5(c)); the in-plane periodicity was also evident from selected area electron diffraction (Fig. 5.5(d)), which shows an ordered network with a ~1.97 nm unit cell dimension. Powder X-ray diffraction (PXRD) displays (100) and (200) peaks at 2ϑ = 4.5º and 9.1º, respectively, demonstrating a hexagonal packing within the *ab* planes. The (001) reflection (peak at 2ϑ = 27.3º) suggests an ordered stacking along the *c* direction with an inter-layer distance of ~0.33 nm. As shown in Fig. 5.1(c), the experimental PXRD pattern agrees well with the simulated inclined and eclipsed AA stacking models (Fig. 5.6 and Appendix), where the inclined structure is energetically favored (similar to the findings made in layered covalent organic frameworks[29]). The porosity of $Fe_3(THT)_2(NH_4)_3$ 2D MOF films was evaluated based on the nitrogen sorption isotherms measured at 77 K (Fig. 5.7); The Brunauer-Emmett-Teller (BET) specific surface area was calculated to be 526±5 m^2/g.

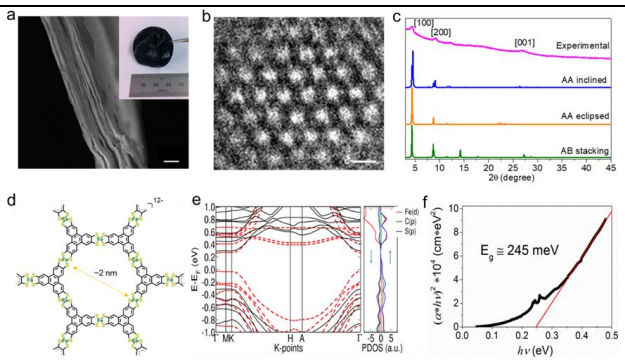

Figure 5.1. Morphology, crystalline structure and band gap of $Fe_3(THT)_2(NH_4)_3$ 2D MOFs. (a) SEM image from cross-side view. Scale bar: 1 µm. Inset in a: photo of large-area, free-standing film. (b) high resolution TEM image of the 2D honeycomb structures. Scale bar: 2 nm. (c) experimental and calculated PXRD patterns from DFT optimized structures. (d) structural schematics of the $Fe_3(THT)_2(NH_4)_3$ 2D MOF. Green, yellow, and grey spheres represent Fe, S, and C atoms, respectively. (e) Calculated electronic structure of inclined AA-stacked $Fe_3(THT)_2(NH_4)_3$ with explicit consideration of ammonium counter ions. The calculated band structure is displayed on the left panel and indicates a direct band gap of 350 meV. The corresponding projected density of states (PDOS) for two spin states are plotted on the right panel for Fe(d), C and S (p) states. (f) Tauc plot indicating a direct band gap of ~245 meV for $Fe_3(THT)_2(NH_4)_3$ 2D MOF films.

X-ray photoelectron spectroscopy characterization demonstrated a high degree of coordination between Fe ions and thiol groups (with Fe:S ratio of 0.97:4; close to Fe:S = 1:4 expected for Fe-bis(dithiolene) linkers, see Appendix, Fig. 5.8). This large degree of iron-sulfur coordination was consistent with SEM-energy dispersed X-ray spectroscopy (EDS) mapping, showing Fe:S ratios of 0.9:4 across the films (Fig. 5.9) and ATR-FTIR characterization (showing a full vanishing of SH- modes from THT monomers upon coordination, Fig. 5.10). Moreover, Mössbauer spectroscopy revealed trivalent iron centers in $Fe_3(THT)_2$ consistent with a square planar coordination geometry (see Appendix, Fig. 5.11 and Table 5.1)[30-33]; based on the detection limit of both setups, Fe(II)/Fe(III) ratios ≤1/1000 where inferred from XPS and Mössbauer spectroscopy in the samples. Elemental analysis confirms the chemical formula $Fe_3(THT)_2(NH_4)_3$ (see Table 5.2), where each FeS_4 unit in the linkages carries one negative charge, which is compensated by one NH_4^+ cation. Taken together, the above measurements show the formation of *π-d* conjugated, porous 2D MOF films with in-plane honeycomb structure and inclined AA-stacked pattern (Fig. 5.1(c) and (d)), as a result of the high degree of complexation between Fe ions and thiol groups.

DFT calculations within the GGA+U approach (see Appendix for details) confirmed the conclusion from XRD data (see Fig. 5.1(c) and Appendix) that inclined AA-stacked $Fe_3(THT)_2(NH_4)_3$ is the most stable structure. The calculated band structure, containing ammonium counterions, including the projected density of states, is summarized in Fig. 5.1(e), and reveals semiconducting behavior with a band gap of ~350 meV (see also Fig. 5.12). The calculations reveal π electrons that are fully delocalized over the conjugated plane (see Fig. 5.13). For a monolayer $Fe_3(THT)_2(NH_4)_3$, the calculated bandgap reduces to 300 meV (see Fig. 5.14), while for eclipsed AA stacks the band gap increases to ~650 meV (Fig. 5.15). The carrier effective masses inferred from the energy band diagram[34] for inclined AA-stacked samples are $m_h^*=0.78m_0$ and $m_e^*=0.98m_0$ for holes and electrons respectively (see Appendix and Table 5.3). Infrared optical transmission measurements confirm that the electronic structure of the $Fe_3(THT)_2(NH_4)_3$ 2D MOF is defined by a direct bandgap, with an absorption onset of ~250 meV (see Tauc plot in Fig. 5.1(f)). A distinct below-bandgap tail is evident from the plot, which can be tentatively attributed to deviations from the perfect periodicity of the lattice (see Appendix).

5.3.2 Photoconductivity of $Fe_3(THT)_2(NH4)_3$ 2D MOF by THz spectroscopy

To understand the charge transport nature of the $Fe_3(THT)_2(NH_4)_3$ 2D MOF, we performed time-resolved THz spectroscopy (TRTS)[26] on the films. In these experiments, charges are injected optically into the material, with a femtosecond laser pulse and the change in the conductivity is measured on ultrafast timescales with a ~1 picosecond THz pulse. TRTS provides the time-dependent complex photo-conductivity, i.e., its real and imaginary parts, over a wide frequency range (0.6-1.6 THz).

Fig. 5.2(a) shows the frequency-integrated real part of the photo-conductivity as a function of pump-probe delay (80 μJ/cm^2 800 nm pump and ~1 THz probe bandwidth). The plot reveals an ultrafast rise of the pump-induced real conductivity which is followed by a bi-phasic deactivation mechanism; the resolved bi-phasic nature for the relaxation process can be tentatively attributed to electron and hole contributions to the photo-conductivity. To elucidate the nature of the photo-conductivity presented in Fig. 5.2(a), we analyzed the frequency-resolved complex photo-conductivity of the sample. Fig. 5.2(b) shows the real and imaginary conductivity components as a function of frequency (0.3 ps after pump excitation). The photo-conductivity is characterized by positive real and imaginary components that are decreasing and increasing with frequency, respectively, in the probed THz window. This spectral response is consistent with the measured photo-conductivity arising from free, delocalized charges[26] in the analyzed $Fe_3(THT)_2(NH_4)_3$ samples and, accordingly, the Drude model provides a suitable description.

The best fit to Eqn.2.14 is shown as red lines in Fig. 5.2(b); from the fit a scattering time of τ_S = 62±6 fs and a plasma frequency of ω_P = 3.2±0.2 THz are directly obtained; assuming that both electrons and holes contribute equally to the TRTS signal - since their effective masses obtained from DFT are very similar - allows inferring a THz mobility of μ_{THz} = 125±9 cm^2/Vs ($\mu = e\,\tau_S/m_{avg}{}^*$); where m_{avg}*=0.88m_0 represents the average effective mass of electrons and holes for $Fe_3(THT)_2(NH_4)_3$ AA inclined stacking; see Table 5.3). The excellent agreement between Drude model and experimental data demonstrates that, upon light absorption, freely moving delocalized carriers (obeying band-like transport) are generated in the analyzed $Fe_3(THT)_2(NH_4)_3$ 2D MOF samples; these free carriers

are impeded in their motion only by momentum-randomizing scattering events, every ~60 fs.

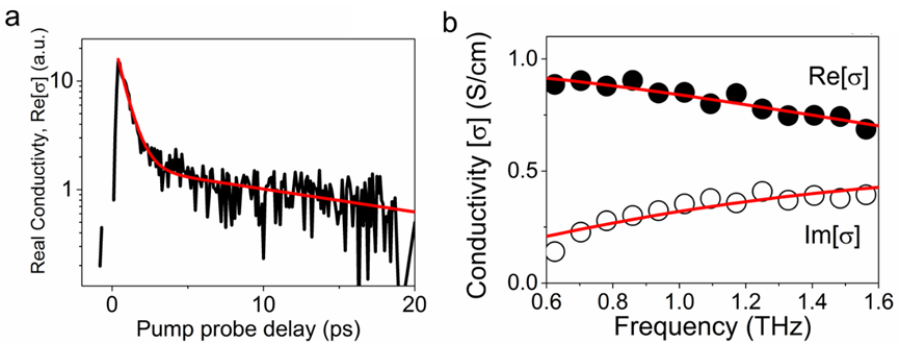

Figure 5.2. Room temperature photoconductivity of $Fe_3(THT)_2(NH_4)_3$ 2D MOFs measured by THz spectroscopy. (a) real part of photoconductivity as a function of pump-probe delay (800 nm excitation wavelength 80 μJ/cm^2 and ~1 THz bandwidth probe; under nitrogen environment). Red lines represents best fit to a bi-exponential decay function; (b) real (solid circle) and imaginary (open circle) components of the frequency-resolved complex conductivity (measured 0.3 ps after photoexcitation); red lines represent a Drude fit to the data.

To reveal the nature of the scattering mechanisms limiting the charge mobility, we analyzed the evolution of the photo-conductivity with temperature (Fig. 5.3(a); temperature range 300-100 K; under vacuum). Drude fits to the data following Eqn.2.14 are shown as red lines in Fig. 5.3(a); from the fits, we infer THz mobilities and carrier densities (see Fig. 5.16) as a function of temperature as summarized in Fig. 5.3(b) (solid black and open white circles in the top and bottom panels respectively). A room temperature mobility of μ_{THz} = 211±7 cm^2/Vs (scattering rate of τ_S = 104±5 fs) is obtained by TRTS for this particular $Fe_3(THT)_2(NH_4)_3$ 2D MOF sample. The increased scattering time for the sample presented in Fig. 5.3(b) (τ_S= 104±5 fs; mobility μ_{THz} = 211±7 cm^2/Vs) compared to that shown in Fig. 5.2(b) (τ_S = 62±6 fs; μ_{THz} = 125±9 cm^2/Vs) is likely associated with sample-to-sample variations in local carrier concentrations (e.g. induced by doping). Results for a sample exhibiting an even shorter scattering time are shown in Fig. 5.3(b) (Fig. 5.16).

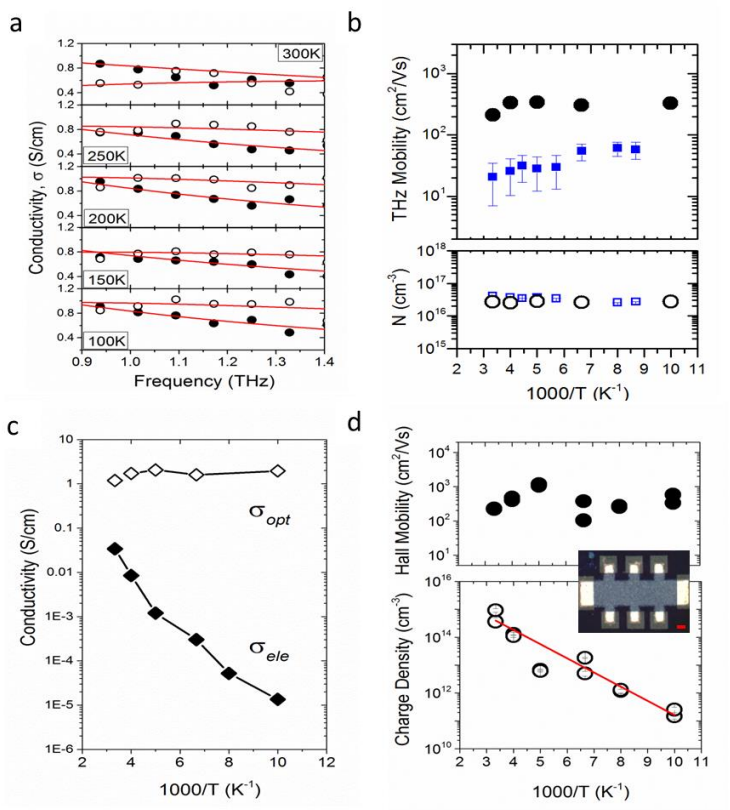

Figure 5.3. Temperature dependence of photoconductivity of $Fe_3(THT)_2(NH_4)_3$ 2D MOFs measured by THz spectroscopy and Hall effect DC conductivity. (a) real (solid circles) and imaginary (open circles) components for the frequency-resolved complex photo-conductivity as a function of temperature (0.3 ps after photoexcitation; under vacuum). Red lines represent Drude fits to the data. (b) THz mobility and charge carrier density (N) dependence vs. temperature (upper and lower panel respectively) for two samples displaying different room temperature mobilities as discussed in the text. Error bars represent the standard deviation (c) logarithmic dependence for the optical (σ_{opt}, open diamonds) and electrical (σ_{ele}, closed diamonds) DC conductivities versus reciprocal temperature inferred from THz spectroscopy and 4-probe measurements, respectively. (d) DC Hall charge mobility and charge carrier density vs. temperature obtained from Hall Effect measurements, each temperature contains 2 values obtained for positive and negative magnetic fields. The inset displays the Hall bar geometry; the scale bar represents 100 μm.

The sample-to-sample variability of the scattering times (and hence mobilities), along with the temperature independence of those times, shown in

Fig. 5.3(b), both point to impurity scattering as the primary mechanism limiting charge transport[35]; the small increase in sample's mobility between 300 and ~250 K can be tentatively attributed to an additional contribution from phonon scattering. The primary role of impurity scattering on limiting charge carrier transport found in our samples agrees well with the conclusions obtained for other 2D materials such as graphene[36] and MoS_2[37-39]. In our 2D MOF sample, ionized metal centers (e.g., Fe(III)) could represent intrinsic sources for impurity scattering. The important role of Fe(III) centers as acceptor states (inducing p-type doping) in iron-based MOFs have been discussed in detail recently[40]. For our samples, the dominant presence of Fe(III) centers is indeed evident from XPS and Mössbauer spectroscopy (see Figs. 5.8 and 5.11; an analysis of iron oxidation state is presented in the Appendix). Strong p-type doping is apparent from the Hall effect measurements as discussed below (see also Appendix). Furthermore, it is conceivable that FeS_4 nodes (carrying one negative charge compensated by a NH_4^+ cation) are the locations in the 2D lattice more prone to suffer deviations from crystal perfection – as such, they could represent locations where free electron motion is impeded by scattering; this suggestion agrees well by noting that we infer a mean free path for the free carriers of ~1.5 nm (see Appendix), a value which is commensurate with the in-plane spacing between FeS_4 nodes. However, several other types of defect are expected to be present in the material, all with the potential to contribute to the averaged carrier scattering.

It is instructive to compare the optical and electrical conductivities of the 2D MOF, plotted together in Fig. 5.3(c). The optical DC conductivity (σ_{opt}, open diamonds) is obtained from TRTS by extrapolating the real photoconductivity Drude fit component to zero frequency. σ_{opt} reflects the conductivity of this material for a given carrier density *N,* defined by the number of photo-generated carriers. Since both the scattering time and carrier effective mass are largely temperature independent, so is σ_{opt}. In contrast, the electrical DC conductivity (σ_{ele}; closed diamonds) measured using 4-probe method on the Hall bars shows a strong temperature dependence, decreasing by almost four orders of magnitude from 300 to ~100 K (see Fig. 5.3(c) and Fig. 5.18-5.19). For temperatures below ~100 K, the response of the samples becomes non-ohmic (see Fig. 5.20).

As the TRTS results unequivocally reveal that the local mobility of photo-generated free charge carriers is temperature independent, the simultaneous observation of a strong variation of σ_{ele} with temperature therefore suggests a thermally-activated carrier density population in the samples and/or a reduction

in sample's DC mobility induced by e.g. grain boundary scattering[41,42]; the former and the latter being consistent with the low bandgap of the analyzed MOFs (Fig. 5.1(e),(f)) and the polycrystalline nature of our samples (Fig. 5.5(a) and (b)), respectively. To disentangle the potential contribution of these two effects on the DC conductivity, temperature-dependent Hall effect measurements were conducted on 1.7 µm-thick $Fe_3(THT)_2(NH_4)_3$ 2D MOFs films. In Fig. 5.3(d) we plot the DC Hall charge carrier mobility and the charge carrier density inferred from Hall effect measurements (see also Fig. 5.21-5.22 and Table 5.4). Fig. 5.3(d) shows that the Hall DC mobility is barely affected over the analyzed temperature range, while a clear correlation between the temperature and the carrier density (Fig. 5.3(d)) is found, which accounts for the temperature-dependent 4-probe conductivity results (σ_{ele}, in Fig. 5.3(c)). The Hall effect measurements demonstrate that thermally-excited carriers are responsible for the temperature dependence of the 4-probe conductivity, as opposed to a reduction in the DC mobility of carriers (Fig. 5.3(d) and Fig. 5.23-5.27). Assuming that $\sigma_{ele}(T)$ is proportional to the thermally activated carrier concentration in the samples($\sigma_{ele}(T) \propto N(T) \propto \exp[-E_g/2k_BT]$) we obtain an estimate of the bandgap of E_g = 201 ± 20 meV, in reasonable agreement with the bandgap inferred optically and theoretically (see Fig. 5.1(e), (f)). Furthermore, and quite remarkably, the resolved room temperature Hall DC mobility (μ_{Hall} = 229±33 cm^2/Vs) agrees within error with the one inferred by THz spectroscopy (μ_{THz} = 211±7 cm^2/Vs). The temperature independence of both the terahertz and Hall mobilities points to impurity scattering as the common scattering mechanism impeding both AC and DC mobilities in $Fe_3(THT)_2(NH_4)_3$ 2D MOFs films. Apparently, grain boundaries do not constrain long-range transport of free charge carriers in our samples; an observable that we rationalize by the strong doping in the samples[43].

5.4 Summary

In this work we have demonstrated band-like transport in a semiconducting porous 2D MOF by resolving a Drude response from the frequency resolved photoconductivity spectra via TRTS measurement at the room temperature. This new material exhibits a direct infrared bandgap of ~0.25eV and supports record charge carrier mobilities up to ~220 cm^2/Vs. Moreover the temperature dependent complex photoconductivity results revealed that impurity scattering is

the dominating mechanism limiting scattering rates and thus mobilities. Last but not the least, we compared the optical and electrical conductivities of this material and found a quantitative agreement between the mobilities measured from TRTS and that measured from Hall conductivity measurement. This strongly suggested that grain boundaries in our 2D MOFs did not impede the long-range charge transport. Our findings opened new avenues to conductive 2D MOFs for the applications where long-range charge transport is required.

5.5 Appendix

I acknowledge here the contribution of Prof. Xinliang Feng and Dr. Renhao Dong at TU Dresden for providing, characterizing samples as well as fabricating Hall bar; Prof. Artur Erbe at Helmholtz-Zentrum Dresden-Rossendorf & Center for Advancing Electronics Dresden for conducting four-probe conductivity and Hall effect measurements; Prof. Thomas Heine at Wilhelm-Ostwald-Institute of Physical and Theoretical Chemistry, Leipzig University for DFT calculations; Prof. Claudia Felser at Max Planck Institute for Chemical Physics of Solids for performing Mössbauer spectroscopy.

5.5.1 Materials

Starting materials (e.g., iron, bromine, triphenylene, benzyl mercaptan, sodium, sodium hydride, DMI, $Fe(acac)_2$) were purchased from Sigma-Aldrich. Liquid ammonium (purity >99.999 Vol.%) was purchased from Air Liquid GmbH (Germany). Unless otherwise stated, the commercially available reagents and dry solvents were used without further purification. Water was purified using a Milli-Q purification system (Merck KGaA). The reactions were performed using standard vacuum-line and Schlenk techniques. Work-up and purification of all compounds were performed in air and with reagent-grade solvents. Column chromatography was performed with silica gel (particle size 0.063-0.200 mm; obtained from Macherey-Nagel), and silica-coated aluminum sheets with a fluorescence indicator (obtained from Macherey-Nagel) were used for thin-layer chromatography.

The ligand, 2,3,6,7,10,11-triphenylenehexathiol (THT), was synthesized following our previous reported protocols[28].

5.5.2 General characterization

UV-visible spectra were measured on a Cary 5000 UV-Vis-NIR (Agilent Technologies) spectrophotometer at room temperature using a 10-mm quartz cell and a 3*3 cm^2 quartz wafer. Infrared spectra were recorded on a FT-IR Spectrometer Tensor II (Bruker) with an ATR unit. ^{1}H NMR and ^{13}C NMR spectra for the synthesis of the ligands were recorded in deuterated solvents on a Bruker DPX 250 spectrometer. High resolution MALDI-TOF mass spectra were recorded on a Bruker Reflex II-TOF spectrometer using a 337-nm nitrogen laser with TCNQ as the matrix.

The morphology and structure of the samples were investigated by transmission electron microscopy (TEM, Zeiss, Libra 200 KV), scanning electron microscopy (SEM, Zeiss Gemini 500), and optical microscopy (Zeiss) with a Hitachi KP-D50 color digital CCD camera. Energy dispersed X-ray spectroscopy (EDS) was performed using a monochromatic Al Kα radiation source (1486.6 eV). Atomic force microscopy (AFM) measurements were performed using a Veeco Dimension 3100 scanning probe microscope operating in tapping mode. All AFM images were recorded on a 300-nm SiO_2/Si substrate to facilitate height determination near cracks. X-ray powder diffraction (XRD) was carried out on Siemens D5000 X-ray diffractometer using Cu Kα (1.5406 Å) radiation at room temperature. X-ray photoelectron spectroscopy (XPS) measurements were carried out using an AXIS Ultra DLD system from Kratos with Al Kα radiation. Both survey and high-resolution spectra were collected using a beam diameter of 100 μm. The instrument was calibrated following the ISO 15472 protocol, and spectra were referred to the Au47/2 peak at 84 eV. The spectra were processed with CasaXPS software (version 2.3.15, Casa Software Ltd, Wilmslow, Cheshire, UK). Nitrogen sorption measurements were conducted at 77K on a Quantachrome volumetric analyser. All samples were degassed at 120 ºC for at least 4 h before every measurement. Specific surface areas were determined by the standard BET method based on the relative pressure between 0.05 and 0.20. The pore size distribution was calculated using the non-local density functional theory method.

5.5.3 ^{57}Fe Mössbauer spectroscopy measurements

Mössbauer spectra of $Fe_3(THT)_2(NH_4)_3$ were collected between 5.2 and 292 K with a standard WissEl spectrometer, which was operated in the constant acceleration mode and which was equipped with a ^{57}Co/Rh source. The sample

(55 mg) was ground and filled into a Plexiglass sample container with inner diameter of 13 mm. Spectra were obtained at various temperatures using a Janis-SHI-850-5 closed cycle refrigerator (CCR). The isomer shifts are given relative to α-iron. The data were evaluated with the program MossWinn[44] within the thin absorber approximation. Spectra in the paramagnetic phase were described by doublets with Lorentzian line shapes. The low temperature spectra (T = 5.5-8 K) were evaluated by diagonalizing the full Hamiltonian for combined electric quadrupole and magnetic hyperfine interaction and by assuming a hyperfine field distribution which was extracted using the Hesse-Rübartsch method implemented in MossWinn.

5.5.4 First-principle calculations of $Fe_3(THT)_2(NH_4)_3$ layers

Density-functional theory (DFT) calculations on the crystal structure of $Fe_3(THT)_2(NH_4)_3$ 2D MOF were carried out within the plane-wave based DFT implementation in the VASP code[45]. PBE exchange-correlation functional[46] with D2 dispersion correction[47] was employed. The ions were modeled with the projector augmented-wave (PAW) method.[48,49] Coulomb and exchange interactions of the localized d orbitals in Fe ions were treated within the framework of the self-interaction corrected DFT+U method[50], using the Dudarev approach[51]. The effective Coulomb (U) and exchange (J) parameters in DFT+U are U = 4 eV and J = 1 eV. This set of (U, J) parameters for TM d orbitals have been tested extensively in metallo phthalocyanine based systems[52-56].

Monolayer with explicit NH_4^+ counter ions was modeled as a slab with 10 Å vacuum space between the layers. Geometry optimization of the investigated 3D structures was performed for several types of 3D stacking (AA eclipsed, AB, and AA-inclined) with presence of explicit NH_4^+ counter ions. The number of counter ions was chosen to be one NH_4^+ ion per one Fe center, as suggested by the results obtained by the Mössbauer spectroscopy measurements, which indicate that the oxidation state of the Fe ions was 3+. Thus, one FeS_4 unit in the linkages carries one negative charge, which was compensated by one NH_4^+ cation. For geometry optimization, a kinetic-energy cutoff of 500 eV was used to define the plane-wave basis set. In all calculations spin polarization was considered. The ion positions, cell shape, and volume were relaxed using ISIF-tag 3. To obtain the electronic structures, a single point calculation with a kinetic-energy cutoff of 800 eV was used to define the plane-wave basis, and the electronic Brillouin zone was

integrated using Γ-centered automatic k-mesh generation with 2×2×15 subdivision. Gaussian smearing with a width, σ, of 0.05 eV was used to broaden the density of states in the plots, and band structures were obtained by calculating eigenvalues non-self consistently at strings of *k*-points along the high-symmetry paths through the Brillouin zone.

5.5.5 Structural characterization of the $Fe_3(THT)_2(NH_4)_3$ 2D MOF film

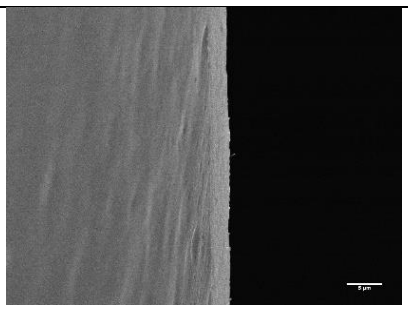

Figure 5.4. SEM image of the top surface of the $Fe_3(THT)_2(NH_4)_3$ 2D MOF film with the thickness of 1.7±0.1 μm. The film surface is flat and compact without any cracks within large area. Scale bar: 5 μm.

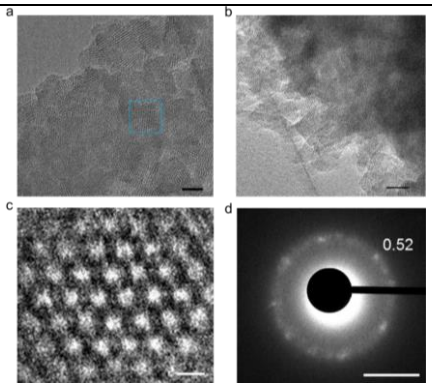

Figure 5.5. TEM analysis of the $Fe_3(THT)_2(NH_4)_3$ 2D MOF film. (a,b) TEM image of the fragments of the 2D MOF film after long-time sonication in ethanol. Scale bar: 20 nm. The crystal domain can be evaluated with the size ranging from tens to hundreds of nanometers. (c) high resolution TEM image of the honeycomb structure (scale bar: 2 nm). (d) selected area electron diffraction shows polycrystalline diffraction ring. The ring size reveals an ordered network with a ~1.97 nm cell size.

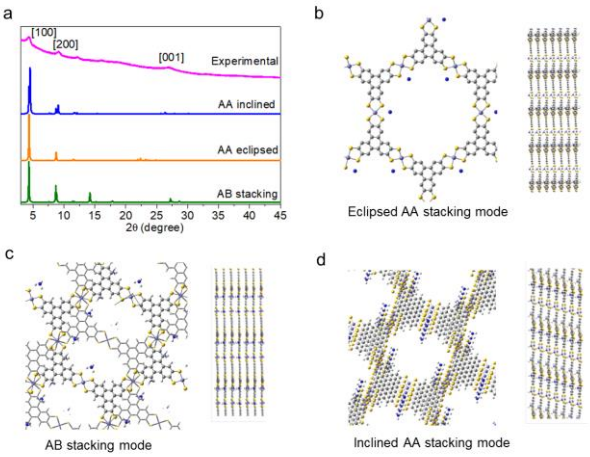

Figure 5.6. Crystal structure analysis of the $Fe_3(THT)_2(NH_4)_3$ 2D MOF film by powder XRD. (a) experimental and simulated PXRD patterns. (b-d) DFT calculated stacking arrangements for the layers of $Fe_3(THT)_2$, including AA (eclipsed and inclined), AB, respectively. After comparison, the $Fe_3(THT)_2(NH_4)_3$ 2D MOFs are determined to present inclined AA stacking model.

The relative stability per unit cell $Fe_3(THT)_2(NH_4)_3$, for the different stacking types was determined. The most stable stacking is inclined AA (0.0 eV), followed by eclipsed AA eclipsed (0.10 eV higher in energy), and AB-stacking (0.37 eV higher in energy).

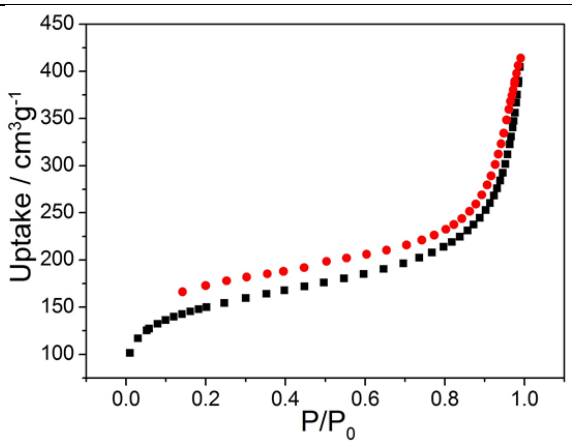

Figure 5.7. N_2 sorption isotherms of $Fe_3(THT)_2(NH_4)_3$ 2D MOFs at 77 K reveal a Brunauer-Emmett-Teller surface area of 526±5 $m^2 g^{-1}$. Black dots: adsorption. Red dots: desorption

5.5.6 Compositional analysis of the $Fe_3(THT)_2(NH_4)_3$ 2D MOF film

X-ray photoelectron spectroscopy (XPS) measurements were conducted to further probe the chemical composition of the $Fe_3(THT)_2(NH_4)_3$ films. The spectrum reveals the presence of Fe 2p, C 1s, N 1s, S 2s and S 2p core levels (Fig. 5.8(a)). The high-resolution Fe 2p photoemission spectrum shows two sets of peaks (Fig. 5.8(b)), with binding energies of 710.9 and 723.9 eV, which are assigned to the 2p3/2 and 2p1/2 levels, respectively, indicating the presence of Fe(III) species in $Fe_3(THT)_2$ MOFs. The S 2p peak in the XPS spectrum occurs at a binding energy of ~162 eV. Deconvolution of the S 2p signal generates high-intensity dual peaks at 163.8 and 165.1 eV derived from the Fe-S units, indicating efficient complexation between Fe ions and thiol groups (Fig. 5.8(c)). Quantitative analysis of the Fe and S signals suggests a Fe:S ratio of approximately 0.97:4, which is in consistence with the $Fe_3(THT)_2$ model. The N 1s signal results from the counter ions of NH_4^+, which balance the charges of this MOF material.

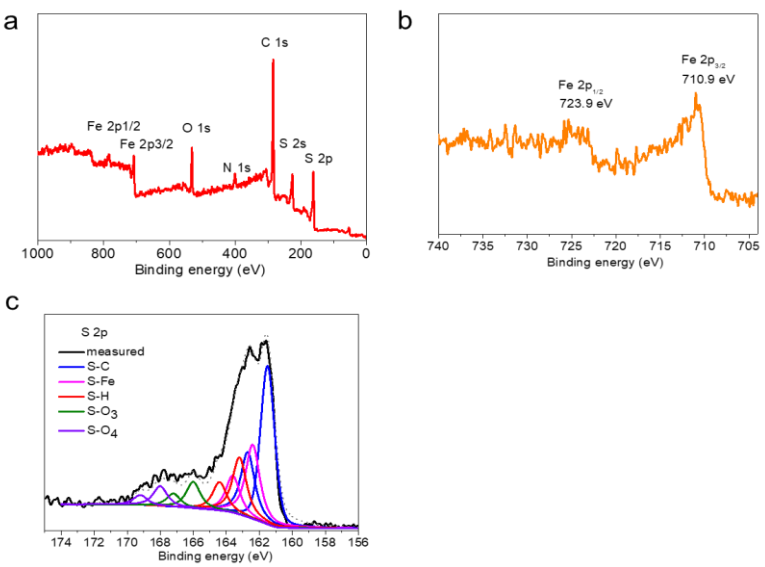

Figure 5.8. XPS analysis of $Fe_3(THT)_2(NH_4)_3$ 2D MOF film. (a) Energy survey spectrum. (b) high-resolution spectrum in the Fe 2p region. (c) high-resolution spectrum in the S 2p region. The doublet peaks with an intensity ratio of 1:2 are due to spin orbit coupling, with Δ=1.2 eV, and are characteristic of the S 2p3/2 and 2p1/2 orbitals.

5.5.7 Analysis of Fe(II)/Fe(III) ratio from XPS data

Only peaks arising from Fe(III) species were resolved form high-resolution XPS Fe 2p photoemission spectrum. These peaks were resolved at binding energies of 710.9 and 723.9 eV (Fig. 5.8(b)) and assigned to the 2p3/2 and 2p1/2 levels of Fe(III) species in $Fe_3(THT)_2$ MOFs[57,58]. We were unable to distinctly resolve any peak arising from Fe(II) species; these are expected to be detected at binding energies of ~709.0-709.9 eV [59-61]. We conclude that Fe(II)/Fe(III) ≤ 1/1000 (XPS detection limit ~0.1%).

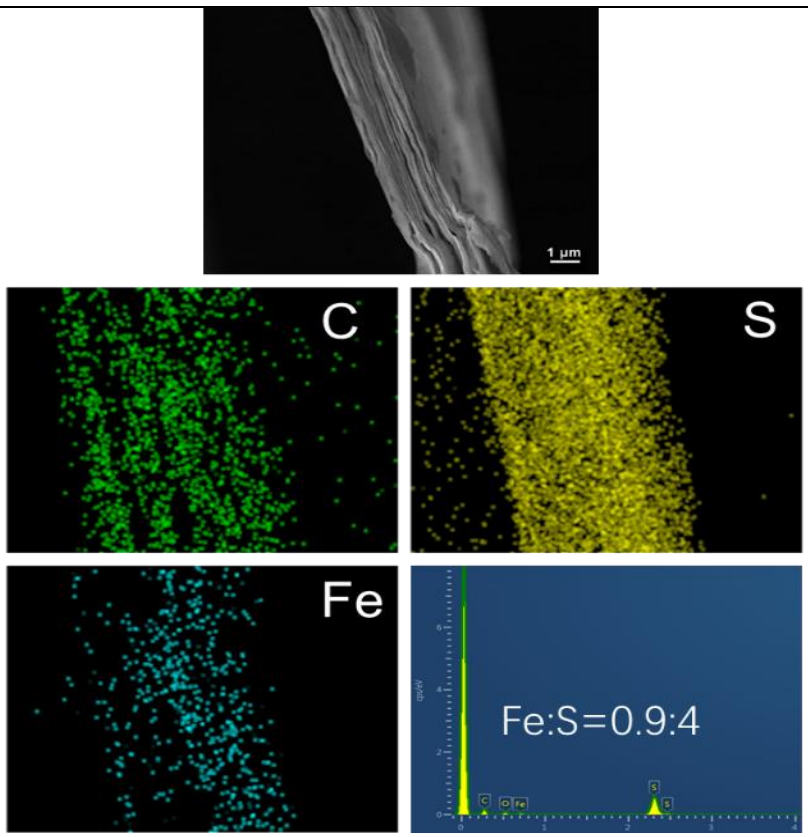

Figure 5.9. SEM-energy dispersed X-ray spectroscopy (EDS) analysis of the cross section of the $Fe_3(THT)_2(NH_4)_3$ 2D MOF film with the thickness of 1.7±0.1 µm. A homogeneous element distribution of Fe, S, and C was observed in the film with the Fe:S ratio of approximately 0.9:4, which agrees with the expected composition of iron bis(dithiolene) linkers (Fe:S = 1:4) and thus suggests a high degree of coordination between Fe ions and thiol groups throughout the films.

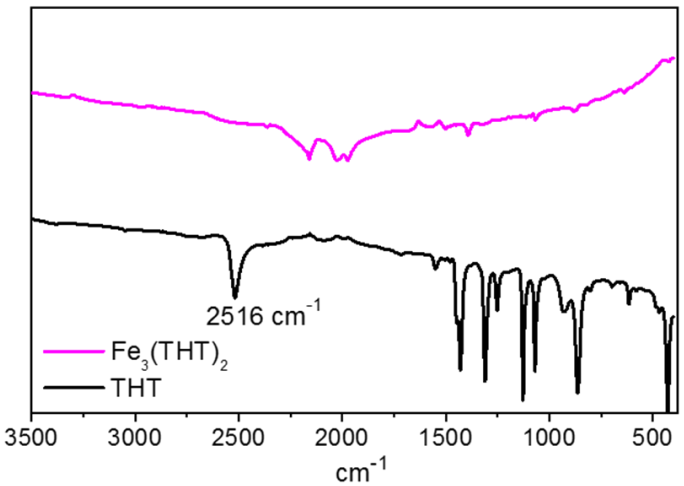

Figure 5.10. FT-IR analysis of the $Fe_3(THT)_2(NH_4)_3$ 2D MOF film. The attenuated total reflection IR (ATR-IR) spectra of the $Fe_3(THT)_2$ films and THT monomer are compared. Whereas the THT monomer exhibited a strong signal at 2516 cm^{-1} attributable to the S-H stretching vibrations, this peak vanished in the $Fe_3(THT)_2$ films, suggesting that the thiol groups were efficiently coordinated to Fe ions to form iron bis(dithiolene) linkers.

5.5.8 ^{57}Fe Mössbauer spectra measurement

In order to investigate the iron coordination, local electronic structure, and magnetic properties, ^{57}Fe Mössbauer spectra were measured between 5 and 292 K (Fig. 5.11, Table 5.1). Down to about 20 K two sets of quadrupole doublets are observed. The Mössbauer parameters of the major component (isomer shift *IS* = 0.18 (0.29) mm/s and quadrupole splitting *QS* = 2.80 (2.78) mm/s at *T* = 292 (40) K) are comparable to those of Fe(III) complexes with thiolate ligands and square planar coordination geometry[30-32], which is in agreement with the anticipated Fe-bis(dithiolene) coordination in $Fe_3(THT)_2(NH_4)_3$. The square planar ligand environment is known to stabilize an intermediate spin S = 3/2 state, and the large quadrupole splitting reflects the unequal electron population of the Fe 3d orbitals split by the ligand field. Corresponding Fe(II) complexes with an intermediate spin S = 1 state are expected to show somewhat larger isomer shifts[31]. Therefore, the observations from XRD (Fig. 5.1(c)), XPS and ^{57}Fe Mössbauer spectra led to the assignment of MOF as $Fe^{III}_3(THT)_2(NH_4)_3$ with a square planar coordination geometry; expected from the spontaneous one electron transfer from Fe(II) to the ligands during the synthesis. Ignoring the possibility of ligand-based redox non-

innocence, the ligands in $Fe_3(THT)_2(NH_4)_3$ were assumed to be a combination of one-electron redox couples with the ratio of 1:1[62]. The charges of the system are compensated by NH_4^+ resulted from the ammonia. The temperature dependence of *IS* reflects the usual second-order Doppler shift. The minority doublet (*IS* = 0.36 (0.48) mm/s, *QS* = 0.70 (0.73) mm/s at *T* = 292 (40) K) is ascribed to a low field gradient at iron, characteristic of a doping with oxide (or hydroxide) on the Fe-bis(dithiolene) linkers[30-32]. The persistence of a quadrupole doublet down to ~10 K verifies that $Fe_3(THT)_2$ is paramagnetic for T > 10 K (Fig. 5.11). In the low temperature range (T ≤ 10 K, Fig. 5.11(b)) drastic changes in the shape of the spectra indicate the onset of magnetic ordering or spin freezing. The 5-K spectrum was modelled by a magnetic hyperfine pattern with a broad distribution of hyperfine fields (Fig. 5.11(b)). Concomitant with the assignment of the iron centers as trivalent is the assumption that Fe-bis(dithiolene) coordination sites are spontaneously reduced by Fe(II) during the synthesis in order to generate a charge-balanced material[30,33].

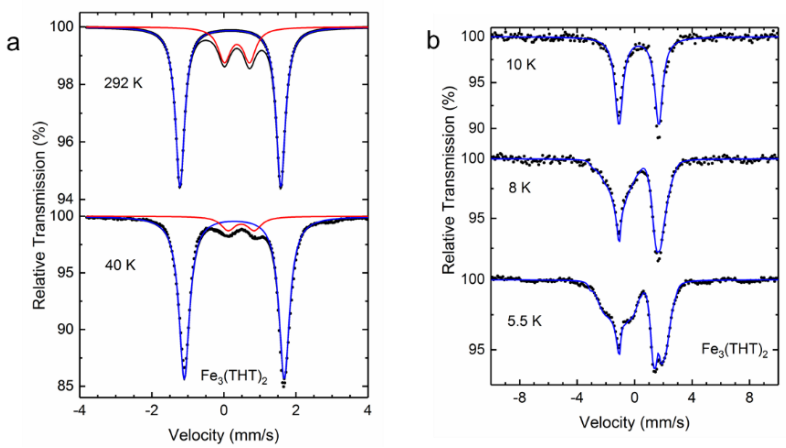

Figure 5.11. ^{57}Fe Mössbauer spectra of $Fe_3(THT)_2(NH_4)_3$ at the indicated temperatures. (a) spectra at 292 and 40 K feature a quadrupole doublet (blue) for $Fe_3(THT)_2(NH_4)_3$ which verifies a paramagnetic state in this temperature range. The minor (red) doublet is assigned to an oxide/hydroxide doping. Note the drastic decrease in the transmission scale between 40 and 292 K which reflects the strong decrease of the Lamb Mössbauer factor of the metal-organic component with increasing temperature. (b) spectra for *T* ≤ 10 K signal the evolution of a magnetic hyperfine pattern for $Fe_3(THT)_2(NH_4)_3$. The spectra at 5.5 and 8 K were fitted by using the full Hamiltonian for combined electric quadrupole and magnetic hyperfine interaction and a broad hyperfine field distribution.

5.5.9 Analysis of Fe(II)/Fe(III) ratio from ^{57}Fe Mössbauer spectra

Isomer shift and quadrupole splitting from ^{57}Fe Mössbauer spectra can be used to determine the oxidation state of iron[30-33]. The Mössbauer parameters of the major component (isomer shift IS = 0.18 (0.29) mm/s and quadrupole splitting QS = 2.80 (2.78) mm/s at T = 292 (40) K) are consistent to those of Fe(III) complexes with thiolate ligands and square planar coordination geometry (Fig. 5.11). Corresponding Fe(II) complexes with an intermediate spin S = 1 state are expected to show larger isomer shifts. In this case, Fe(II) was not detectable from ^{57}Fe Mössbauer spectra (resolution < 0.1%)[64]). We conclude that Fe(II)/Fe(III) ≤ 1/1000 (^{57}Fe Mössbauer detection limit ~0.1%).

Table 5.1. Fitting parameters of the Mössbauer spectra of $Fe_3(THT)_2(NH_4)_3$. The spectra in Fig. 5.11 are described by the following parameters: isomer shift *IS*, quadrupole splitting *QS*, line width *Γ*, the magnetic hyperfine field B_{hf} (here average of the B_{hf} distribution), the asymmetry parameter η ($0 \le \eta \le 1$) of the electric field gradient (efg), the polar angle Ω describing the relative orientation between the principal component V_{ZZ} of the efg and B_{hf}. For the magnetic hyperfine patterns *QS* is obtained as $QS = eQV_{ZZ}/2(1 + \eta^2/3)^{1/2}$, where *Q* is the quadrupole moment of the excited ^{57}Fe nucleus. Note that $\eta = 0$ is in agreement with a square planar coordination and Ω ~ 90° indicates that the spins are oriented in the FeS_4 plane.

T(K)	*IS*(mm/s)	*QS*(mm/s)	*η*	B_{hf}(T)	Ω(°)	*Γ*(mm/s)	Area(%)
292	0.181(1)	2.797(1)				0.305(2)	77.8
	0.364(4)	0.700(6)				0.419(10)	22.2
40	0.288(2)	2.776(1)				0.354(1)	90.1
	0.481(3)	0.726(5)				0.477(8)	9.9
8	0.298(4)	+2.72(1)	0.0(1)	av. 5.2	95(2)	distr.	
5.5	0.305(2)	+2.68(1)	0.0(1)	av. 6.5	89(2)	distr.	

5.5.10 Element analysis of MOF sample

In order to check the validity of our $Fe_3(THT)_2(NH_4)_3$ formula (where THT refers to $C_{18}S_6H_6$), and following reviewer's suggestion, we have performed elemental analysis by a combination of inductively coupled plasma optical emission spectrometry (ICP-OES) and C, H, S and N combustion method; the results (in percentage) are presented in the table below:

Table 5.2. Element analysis of $Fe_3(THT)_2(NH_4)_3$.

	Fe(%)	C(%)	H(%)	N(%)	S(%)
Found	15.57	41.20	2.41	3.80	36.92
Calculated	15.98	41.14	2.30	4.00	36.61

From these estimates, and taking into account the formula $Fe_3(C_{18}S_6H_6)_2(NH_4)_3$, we can obtain the following elemental ratios: Fe/C ≈3/36; Fe/S ≈ 3/12; Fe/H ~ 3/24; Fe/N ≈ 3/3. The latter figure demonstrates that each FeS_4 unit in the linkages carries one negative charge which is compensated by one NH_4^+ cation. Furthermore, the element analysis validates the suggested $Fe_3(THT)_2(NH_4)_3$ chemical formula for the 2D MOF that we have developed.

5.5.11 Analysis of electron transfer during the MOF synthesis

The electron transfer mechanism - the reduction of Fe(II) (in the precursor) to Fe(III) (in the product) - during the synthesis is shown in the following scheme.

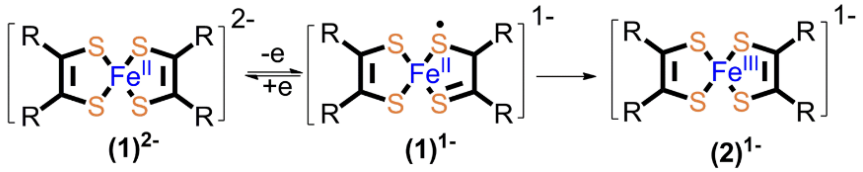

Scheme 5.1. electron transfer mechanism for the reduction of Fe(II) to Fe(III)

As mentioned in the main text, the observations from XRD, XPS and ^{57}Fe Mössbauer spectra led to Fe(III) centers in the MOF with a square planar coordination geometry. This can be rationalized and is expected from the spontaneous one-electron-transfer process taking place from Fe(II) to the ligands in $\mathbf{(1)^{2-}}$, resulting in the formation of $\mathbf{(1)^{1-}}$ with a combination of dithiolate and dithioketone as well as one radical. Due to the bond resonance, $\mathbf{(1)^{1-}}$ can further convert into $\mathbf{(2)^{1-}}$ with the oxidation of Fe(II) to Fe(III). Normally, the $\mathbf{(1)^{1-}}$ and $\mathbf{(2)^{1-}}$ coexist in the complex. However, from our experimental results, we resolve that Fe(III) centers are dominant (Fe(II)/Fe(III) ratio ≤ 1/1000). The trace amount of dissolved [O] in aqueous solution could accelerate the oxidation as Fe(II) is extremely [O]-sensitive.

5.5.12 Electronic structure of $Fe_3(THT)_2$ 2D MOFs with NH_4^+ counter ions

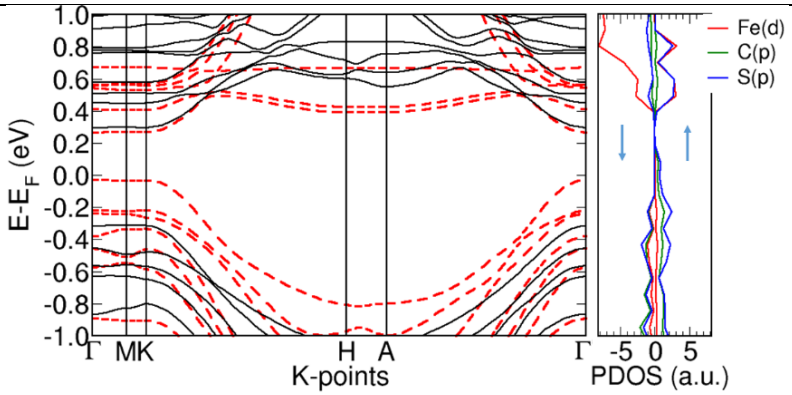

Figure 5.12. Calculated electronic structure of inclined AA-stacked $Fe_3(THT)_2(NH_4)_3$ multilayers with ammonium counter ions. Band structure within the GGA+U approach is displayed. The corresponding projected density of states (PDOS) is shown on the right panel for Fe(d), C and S (p) states, respectively. The red dashed lines denote the bands with spin up, the solid black lines denote the bands with spin down. The inclined AA-stacked multilayered MOF is a semiconductor with a direct band gap of ~0.35 eV.

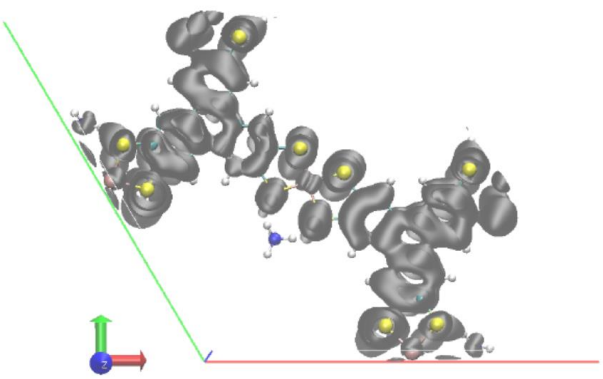

Figure 5.13. Visualization of the two highest occupied molecular orbitals (HOMOs) of $Fe_3(THT)_2(NH_4)_3$ by charge density iso-surfaces along all k-points. Strong hybridization is evidenced between the *d* orbitals of Fe and the orbitals of triphenylene building blocks and bis(dithiolene) moieties.

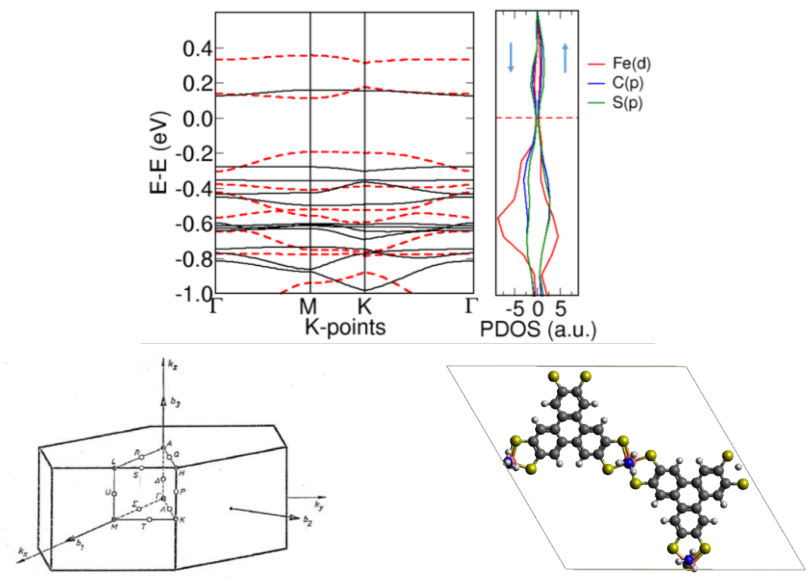

Figure 5.14. Calculated electronic structure of $Fe_3(THT)_2(NH_4)_3$ monolayer with ammonium counter ions. Spin polarized band structure of a monolayer, calculated using the GGA+U approach, is shown on the top left panel. The red dashed lines denote the bands with spin up, the solid black lines denote the bands with spin down. The corresponding projected density of states (PDOS) for Fe(d), C and S (p) states for spin up and spin down are displayed on the top right panel. The high symmetry k-points in the Brillouin zone are shown on the middle panel. The structure of the $Fe_3(THT)_2(NH_4)_3$ unit cell with NH_4^+ counter ions is shown on the bottom panel. The monolayer is a semiconductor with a direct band gap of ~0.3 eV.

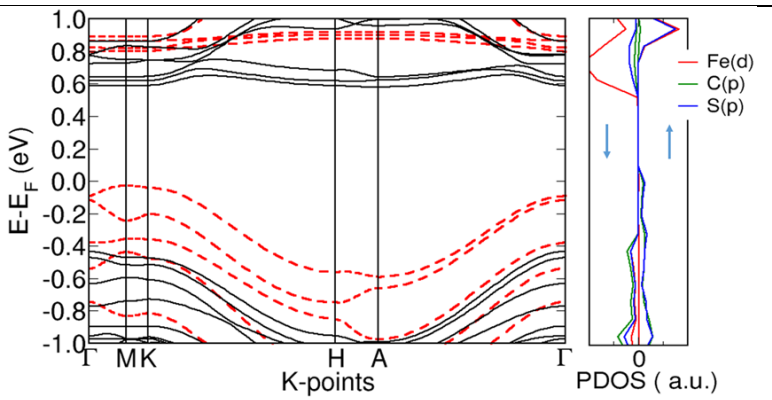

Figure 5.15. Calculated electronic structure of eclipsed AA-stacked $Fe_3(THT)_2(NH_4)_3$ multilayers with ammonium counter ions. Conventions are as in Figure 5.14. The eclipsed AA stacked MOF is a semiconductor with a wider direct band gap of ~0.65 eV.

The carrier effective masses *m** were calculated using the finite difference method on a five-point stencil[34]. A summary of the results is shown in the table below.

Table 5.3. The effective masses from band structure calculations

	m_h^*/m_0	m_e^*/m_0
$Fe_3(THT)_2$ monolayer	0.45	1.34
$Fe_3(THT)_2$ AA eclipsed stacking	1.07	2.08
$Fe_3(THT)_2$ AA inclined stacking	0.78	0.98

5.5.13 Rational for the origin of the Urbach tail resolved by absorbance and its potential impact on THz spectroscopy

We have been able to infer the photo-generation quantum yield in the samples to be 1.5%. This estimate reveals that most of the photo-generated charge carriers get localized on time scales faster than 100fs in the samples (either trapped and/or in form of excitons); in the following we briefly discuss the expected effect of these possible factors on the frequency resolved complex conductivity resolved from THz spectroscopy.

The origin of the Urbach tail has been debated in depth in the literature, one school of thought states that several factors related with "disorder" can contribute to it, including lattice vibrations, impurities, and other deviations from perfect periodicity of the lattice. Specifically for our 2D MOFs factors as sample's inter-plane distance and relative inter-layer alignment; strain and metal substitution have been reported to be able to substantially modulate the 2D MOF bandgap[25,63,64]. Any of these effects related to disorder-induced-localization of charged-carriers could, in principle, provide signatures of localization in the THz frequency resolved conductivity. However, if, e.g. there are 2 independent subpopulations of charge carriers displaying high (Drude-like in crystalline phase) and low (hopping-like in disorder phase) mobilities in the samples, the relative amplitude of both conductivity signals will be dominated by the high mobility phase (the Drude-like response). Another school of thought has modelled the Urbach tail giving rise to exponential band tails from the presence of excitons[65,66]; these features contributing to the below-gap tail have been claimed to be specifically relevant in molecular crystals and polar semiconductors. Excitons can

potentially produce a Lorentz-type line-shape in the frequency-resolved complex conductivity. Excitons being neutral quasiparticles, their contribution to the resolved real part of the <2 THz frequency resolved complex conductivity is expected to be null. For the probed frequencies, excitons could be only traceable by their THz polarizability, which might affect to some extent the line shape of the imaginary conductivity component inferred from THz data. However, the absence of such a feature in our data does not serve as a proof for stating a lack of excitons in the samples, as it can simply mean that their polarizability is not recordable in the samples (under our probing conditions).

At present, with our current data and understanding on the samples, we cannot rule out any of the scenarios proposed above ; however, from the agreement of DC and AC mobilities we can confidently state that a large fraction of photo-generated charge carriers is 'lost' in the samples on timescales <100 fs (either trapped and/or in the form of excitons). These 'lost' carriers do not dominate the observed conductivity in the analyzed samples. Further work is required to understand both the fate of photo-generated carriers and the nature of the Urbach tail resolved in the samples.

5.5.14 Photoconductivity of $Fe_3(THT)_2(NH_4)_3$ 2D MOFs by THz spectroscopy

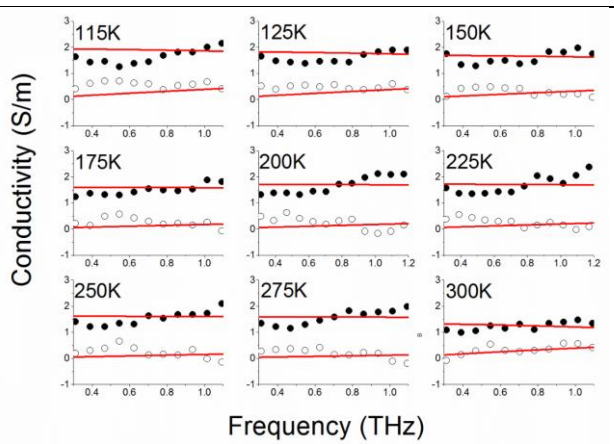

Figure 5.16. Temperature dependence for the THz photoconductivity of for a $Fe_3(THT)_2(NH_4)_3$ sample displaying low mobility. Real (solid circle) and imaginary (open circle) components of the complex conductivity measured as a function of pump-probe delay (at 0.3 ps after 800 nm photo-excitation). Solid red lines represent Drude fits to the data.

5.5.15 Calculation of charge carrier density, quantum yield and mean free path

First, we calculate the number of impinging photons from the excitation density. The 1.7-micron thick sample investigated using THz spectroscopy is characterized by an O.D.=2.6 at the excitation wavelength, implying transmission losses under the pump wavelength excitation (800 nm) below 1% (see figure 5.17 for sample-to-sample variations). Specular reflection losses at 800 nm were measured to be 5%±1%. The observed sample-to-sample variability is likely related to variations in the nominal thickness and/or local doping of the samples. From these numbers, considering a sample thickness of 1.7-micron, and homogeneous excitation of the film, we infer a density of absorbed photons in the sample of N_{hv} = 1.7·10^{18} photons/cm^3.

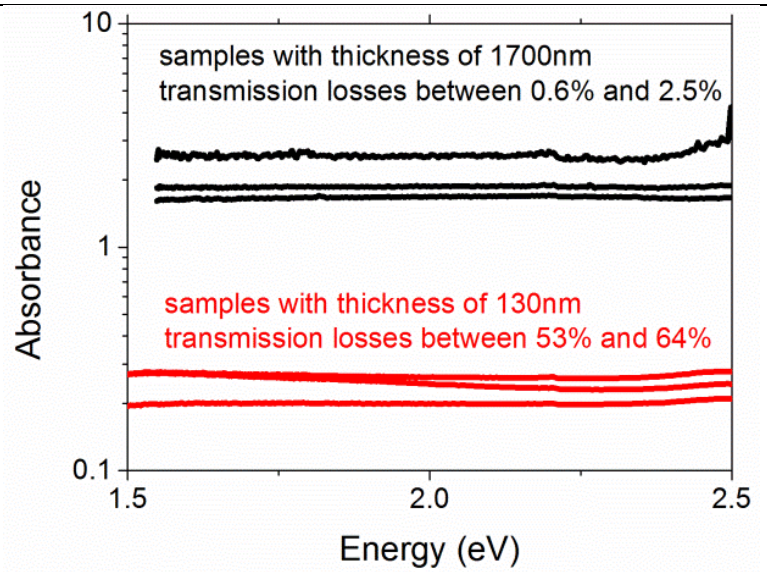

Figure 5.17. Absorbance of $Fe_3(THT)_2(NH_4)_3$ samples with nominal thickness ~1700 (top) and ~130 nm.

The number of photo-generated carriers generated in the samples upon excitation can be calculated as follows. Taking into account the effective mass estimate from DFT ($m_{avg}*/m_0$=0.88) and the plasma frequency independently obtained from Drude fits (ω_P^2) we obtain a carrier density estimate of 2.8·10^{16} cm^{-3}. Comparing the carrier density calculated from the plasma frequency and the

incident photon density in the medium, we find a quantum yield (ξ) for free carrier generation of about 1.5% in the analyzed samples.

Using the Fermi velocity for parabolic discretion relation ($v_F = \sqrt{\frac{2E_F}{m^*}} = \frac{\hbar}{m^*}(3\pi^2 n)^{\frac{1}{3}}$; where m^* is the effective mass of the charge carrier and n is the electron density) together with the scattering time τ_s extracted independently from Drude fits to THz measurements allows us to estimate a mean free path for the carriers of ~1.5 nm. This value is commensurate with the in-plane spacing between iron centers, and hence may indicate that FeS_4 nodes (carrying one negative charge compensated by an NH_4^+ cation) are the locations in the 2D lattice more prone to suffer deviations from crystal perfection – as such, they could represent locations where free electron motion is impeded by scattering.

5.5.16 4-probe DC conductivity measurements

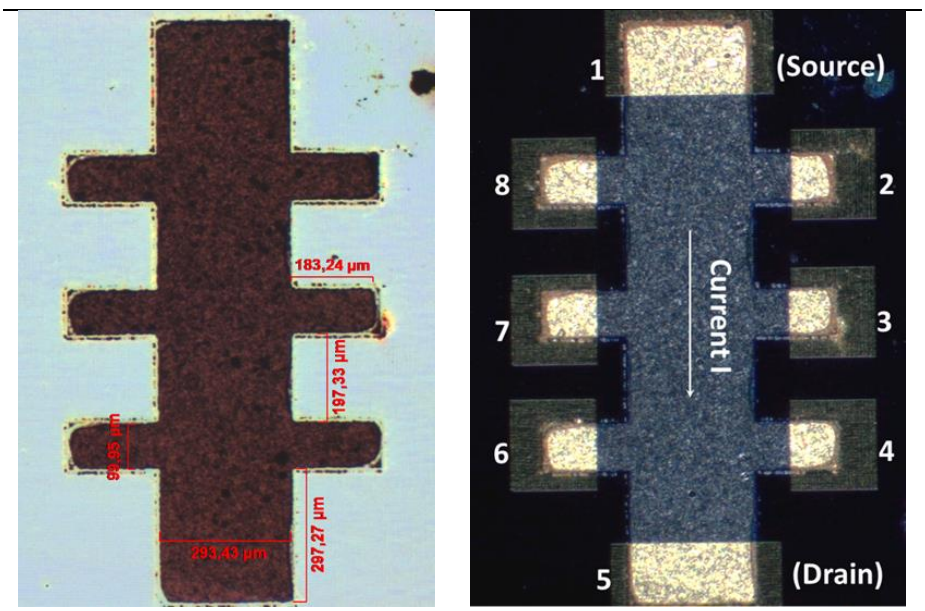

Figure 5.18. Hall-bar geometry by laser ablation of 1.7-micron thick $Fe_3(THT)_2(NH_4)_3$ MOF films (left) followed by deposition of gold contacts (right).

The four-probe conductance (G_{4p}) was obtained by measuring the voltage difference (V_{xx}) across parallel contact pairs i.e. 2-3, 3-4, 6-7, 7-8 in absence of the magnetic field by using the following relation –

$$G_{4p} = \frac{I}{V_{xx}}$$

Where *I* is the current flowing from source to drain i.e. from contact 1 to 5 and V_{xx} is the voltage difference measured between contacts 2-3, 3-4, 6-7 or 7-8.

Four-probe conductivity (σ_{4p}) is calculated using following equation –

$$\sigma_{4p} = \frac{G_{4p} * L}{W * t}$$

Where L is channel length, W (channel width) = 300 µm and t (thickness) = 1.7 µm. The channel length is generally considered center to center distance between the two probes where the V_{xx} is measured.

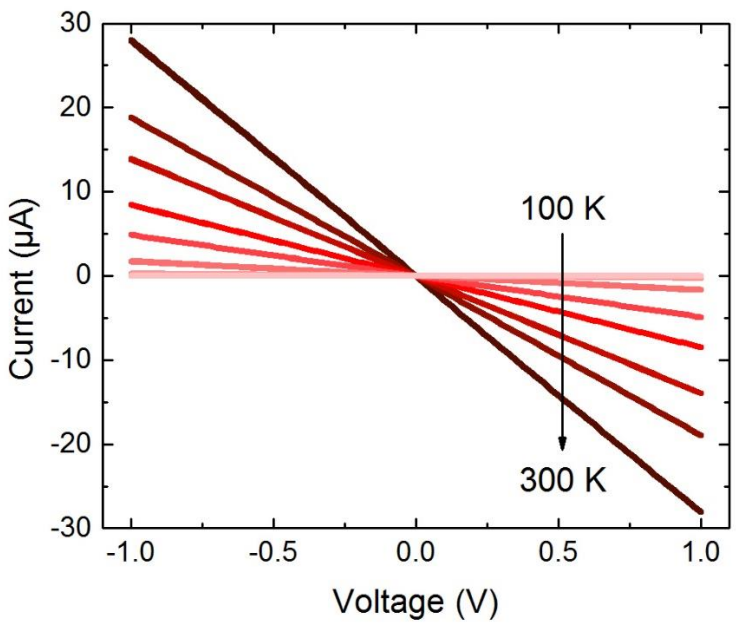

Figure 5.19. Temperature dependent I-V characteristics of the Hall-bar device shown in Fig. 5.18, demonstrating ohmic behavior in the temperature range of 300 K to 100 K.

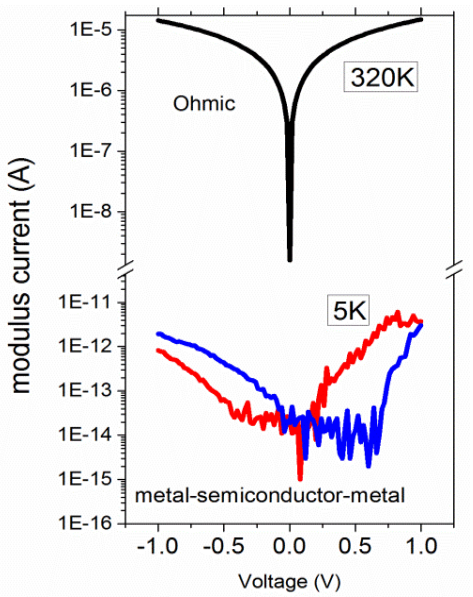

Figure 5.20. Temperature dependent I-V characteristics demonstrating non-ohmic behavior for temperatures <100 K. For temperatures below 100 K the response of the sample becomes increasingly non-ohmic. Revealing a distinct metal-semiconductor-metal behavior with hysteresis on current flow direction (red and blue traces for forward and backward bias, respectively).

5.5.17 Hall Effect measurements

The Hall measurements were performed by sourcing the current from contact 1 to 5 and measuring the Hall voltage (V_{xy}) between the opposite contacts i.e. 2-8, 3-7, 4-6 (Fig. 5.18) in the presence of a vertical magnetic field. The sample was measured from 300 K down to 100 K at regular temperature steps for a magnetic field ranging from 0 to ±0.8 T.

In our experiments, we measured Hall voltage w.r.t current flowing through the circuit at various magnetic fields to extract Hall resistance (R_{xy}). This procedure was repeated at different temperatures until to obtain Hall coefficient ($R_H=dR_{xy}/dB$) as shown in Fig. 5.21 and 5.22.

The charge density (n) and Hall mobility (μ_H) are extracted using the following relation –

$n = \frac{1}{R_H de}$, where d is the thickness of the layer = 1.7 µm

$$\mu_H = \frac{1}{ne\rho_{xx}}$$

We assume a Hall factor equaling 1; appropriate for the description of degenerate intrinsic semiconductor with small bandgap.

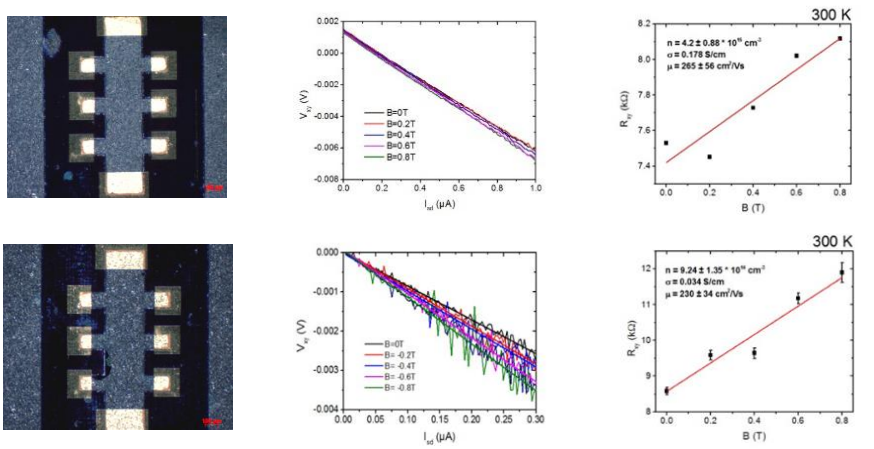

Figure 5.21. Hall Effect measurements on two $Fe_3(THT)_2(NH_4)_3$ samples. Ohmic responses were resolved as a function for the analyzed range of magnetic fields (middle).

The slope obtained from the R_{xy} vs B curve provides a measure of charge density in the samples

$$n = \frac{1}{(dR_{xy}/dB) * d * e}$$

where d = 1.7 µm is the sample thickness and e is electron charge. Mobility (hall) is then inferred from the formula –

$$\mu_H = \frac{1}{\rho_{xx} * n * e}$$

where ρ_{xx} is longitudinal 4-probe resistivity, n is the charge density and e is electron charge.

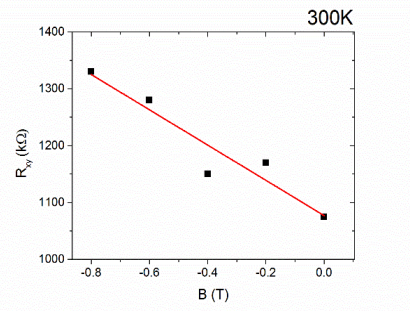
300K
R_{xy} (kΩ)
B (T)

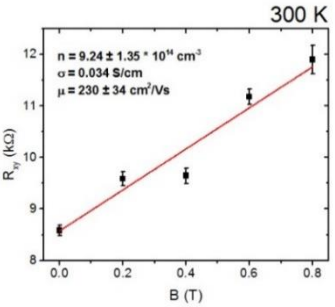
300 K
n = 9.24 ± 1.35 * 10^14 cm^-3
σ = 0.034 S/cm
μ = 230 ± 34 cm^2/Vs
R_{xy} (kΩ)
B (T)

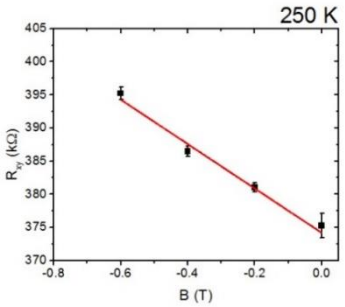
250 K
R_{xy} (kΩ)
B (T)

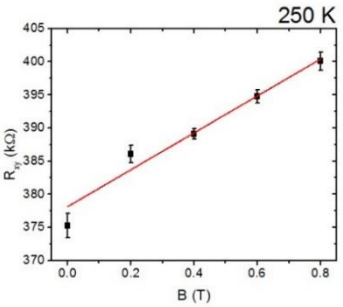
250 K
R_{xy} (kΩ)
B (T)

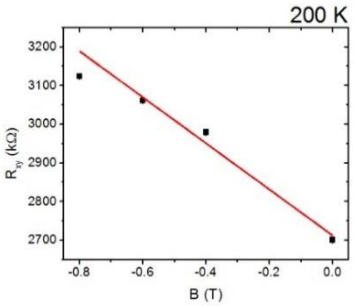
200 K
R_{xy} (kΩ)
B (T)

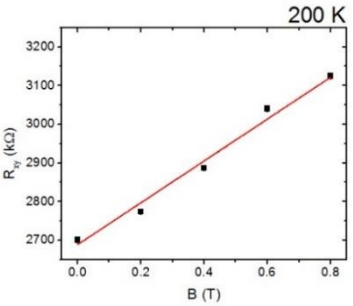
200 K
R_{xy} (kΩ)
B (T)

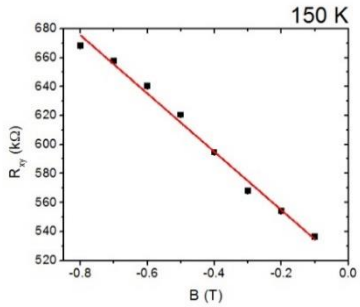
150 K
R_{xy} (kΩ)
B (T)

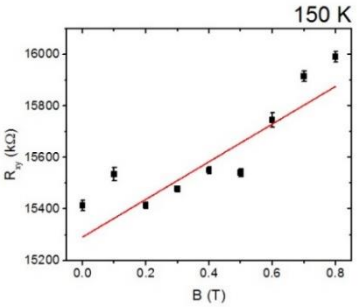
150 K
R_{xy} (kΩ)
B (T)

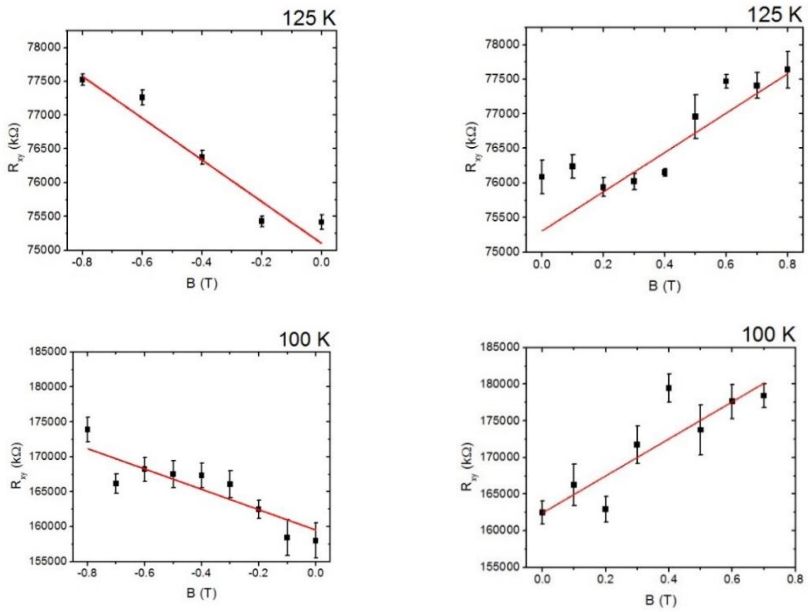

Figure 5.22. Linear dependence of R_{xy} on B at different temperatures for Sample 1, thus showing Hall Effect. The linearity can be seen in both positive and negative magnetic fields in the temperature range of 300 K to 100 K. The offset or the residual resistance obtained at B = 0 T is attributed to misalignment of the opposite voltage probes or asymmetries in the probe element and voltage measurement contacts.

Table 5.4 Summary of Hall data

Temperature (K)	4-probe conductivity (S/cm)	Charge density (cm^{-3})	Mobility (cm^2/Vs)
300 (+B)	$3.400 \cdot 10^{-2}$	$9.24 \pm 1.35 \cdot 10^{14}$	229± 33
300 (-B)		$3.16 \pm 0.86 \cdot 10^{14}$	222 ± 37
250 (+B)	$8.500 \cdot 10^{-3}$	$1.32 \pm 0.15 \cdot 10^{14}$	402 ± 46
250 (-B)		$1.10 \pm 0.11 \cdot 10^{14}$	482 ± 47
200 (+B)	$1.200 \cdot 10^{-3}$	$6.79 \pm 0.45 \cdot 10^{12}$	1067 ± 71
200 (-B)		$6.17 \pm 0.77 \cdot 10^{12}$	1175 ± 147
150 (+B)	$3.023 \cdot 10^{-4}$	$5.03 \pm 0.99 \cdot 10^{12}$	375 ± 75
150 (-B)		$1.83 \pm 0.07 \cdot 10^{13}$	104 ± 4
125 (+B)	$5.236 \cdot 10^{-5}$	$1.29 \pm 0.35 \cdot 10^{12}$	253 ± 69
125 (-B)		$1.19 \pm 0.18 \cdot 10^{12}$	274 ± 40
100 (+B)	$1.351 \cdot 10^{-5}$	$1.50 \pm 0.30 \cdot 10^{11}$	581 ± 119
100 (-B)		$2.52 \pm 0.56 \cdot 10^{11}$	334 ± 74

5.5.18 Analysis of reduced activation energy

A Zabrodskii plot[67] is presented in the right side of Fig. 5.23 for 2-probe conductivity data (see also Fig. 5.25-5.27) in the temperature range from 320 K to 70 K (left panel).

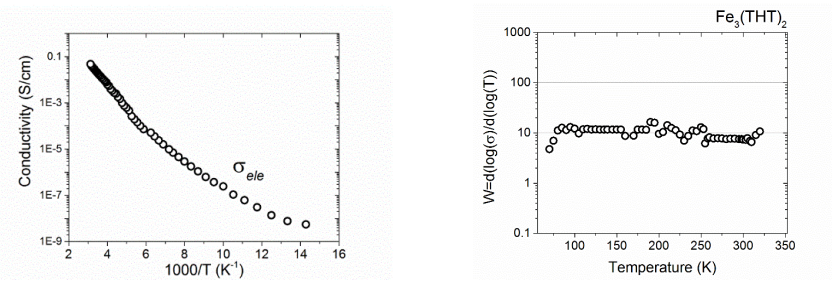

Figure 5.23. (left) conductivity vs. temperature estimated from 2-probe on 70 nm $Fe_3(THT)_2(NH_4)_3$ thick films. (right) Zabrodskii plot for the 2-probe data displayed in the left panel.

As discussed in the paper, Hall measurements as a function of temperature demonstrate that the decay in conductivity is linked to a thermally activated population of carriers for temperatures as low as 100 K. This is supported by fitting the carrier concentration to $N(T) \propto \exp[-E_g/2KT]$; from which we can obtain an estimate of the bandgap of E_g=201±20 meV; this figure is in reasonable agreement with the bandgap inferred optically (~245 meV) and theoretically (~350 meV, see Fig. 5.1(e),(f) in the manuscript). If this interpretation is valid, the Zabrodskii plot for the conductivity data shown in Fig. 5.23 should be consistent with the same physical scenario. That is, we should be able to explain it simply by having the sample in the intrinsic region, with thermal variation of the carrier density across the narrow MOF bandgap. To verify this hypothesis, we compare our 2-probe data on low gap MOF (~250 meV) with the carrier dependence on temperature for Germanium (bandgap 660 meV). Figure 5.24 (left column top) reveals the variation with temperature of carrier density in Germanium over the characteristic intrinsic, extrinsic and freeze-out regions. In the bottom, we replot that data in a Zabrodskii plot (which will be valid for a constant mobility on the same temperature range). The data reveal unambiguously that the intrinsic region (thermally activated population of carrier across the gap) is revealed in the

Zabrodskii plot as a constant reduced activation energy (W). This can be rationalized by taking into account that the Fermi level is invariant vs temperature in the intrinsic region ($E_F=E_g/2$). Furthermore, when the sample enters the extrinsic region (onset ~600 K), the Zabrodskii plot reveals a negative slope which implies a reduced activation energy with reduced T (consistent with a displacement of the Fermi level from the center of the gap towards a dopant level near the valence band in p-type Germanium). In close analogy to the Germanium case, we find that the behavior observed in our analyzed $Fe_3(THT)_2(NH_4)_3$ sample can nicely be explained within the same scenario. Figure 5.24 right-column-top shows the 2-probe data as a function of temperature for our $Fe_3(THT)_2(NH_4)_3$ sample; the data are consistent with the sample being in the intrinsic region (with a constant mobility; revealed from THz and Hall data). For temperatures below ~100 K, the sample enters in the extrinsic region where p-type doping induced by Fe centers is expected to dominate the response in the samples.

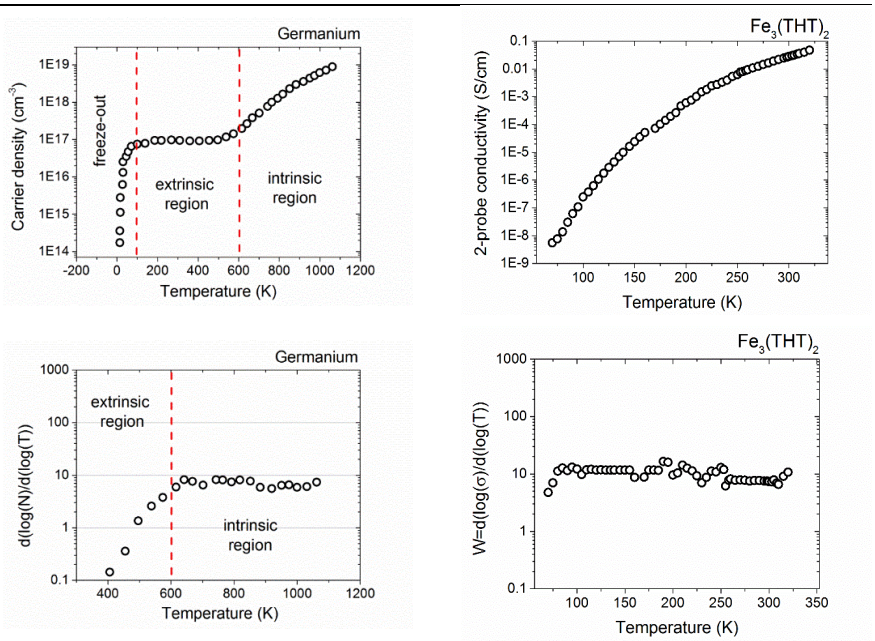

Figure 5.24. (left column) top plot reveals the variation with temperature of carrier density in Germanium over the characteristic intrinsic, extrinsic and freeze-out regions. In the bottom, we replot that data in a Zabrodskii plot (which will be valid for constant mobility on the same temperature range). Germanium data adapted from the variation with temperature for the 2-probe conductivity in our 2D MOF film; The bottom right figure shows a Zabrodskii plot of the same data.

5.5.19 DC conductivity of the $Fe_3(THT)_2(NH_4)_3$ 2D MOF film from 2-probe method

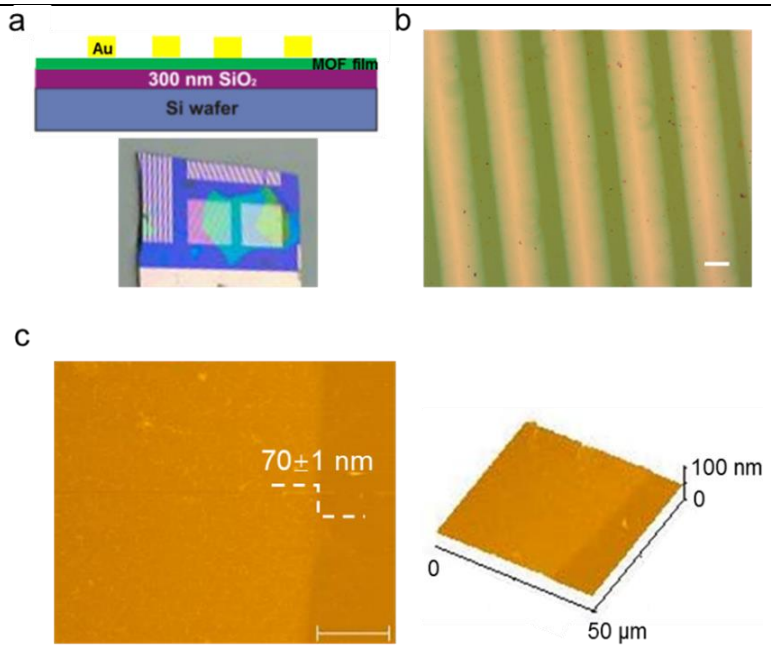

Figure 5.25. Device for the DC conductivity measurements. (a) after transfer of the $Fe_3(THT)_2(NH_4)_3$ MOF film onto a SiO_2/Si wafer, Au electrodes were deposited by thermal evaporation with a channel length of 100 µm between two electrodes and the width of 4.5 mm. (b) Photographic image of the device surface reveals continuous and flat film. No cracks were observed between the electrodes. (c) AFM images of the MOF film in image a reveals the thickness is 70±1 nm. Left: top view. Right: side view.

To measure the electrical conductivity of 2D $Fe_3(THT)_2(NH_4)_3$ MOF films with different thicknesses, the film was transferred onto an n-doped silicon wafer (SiO_2 layer with 300 nm in thickness as dielectric layer). Then a mask with four groups of patterns with different dimensions was applied to determine the area of the electrodes. The top contact gold electrodes were deposited under 10^{-9} bar vacuum conditions through thermal evaporation, at a rate of 0.15 nm/s to a final thickness of 70 nm. The model of the thermal evaporator is Organic Cube and customized by DREEBIT GmbH. The channel length between two electrodes is 100 µm and the width is 4.5 mm (shown in Fig. 5.25).

The conductivities of the films with different thicknesses (from 20 nm to 1.7 µm) at room temperature were measured under vacuum using a *V-I* method by a

semiconductor device analyzer (model: B1500-90000, Keysight Technologies). The voltage applied to the channel changes from - 0.5 V to 0.5 V in 400 steps. The conductivity is calculated based on the equation below:

$$\sigma = \frac{1}{\rho} = \frac{I \cdot l}{V \cdot W \cdot h}$$

I is the current and *V* is the voltage, *l* is the channel length, *W* is the channel width, and *h* is the film thickness. Each sample was measured at four different positions to obtain an average value.

The low-temperature measurements for films with 70 nm and 1.7 µm in thickness were performed in a Lakeshore probe station, which is cooled by continuous flow of liquid He. The DC *I-V*-characteristics were recorded using an Agilent Parameter Analyzer 4156C. The samples were first cooled down to 4.2 K, and then electrically measured while warming up in the range of -1 to +1 V in dark. Conductivity was observed at 4.2 K as a function of time after cooldown, indicating that the thermal coupling of the polymer to the environment is rather weak and that the base temperature was achieved after a cooling period of approx. 30 min. Current-voltage curves were taken at every 5 K. The homogeneity of the materials was checked at room temperature before cooling down.

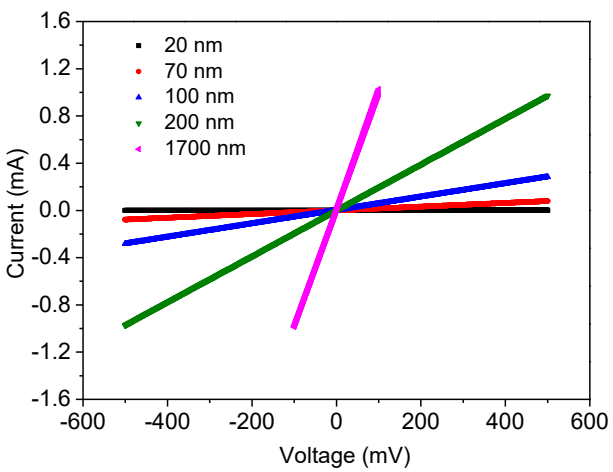

Figure 5.26. DC conductivity of $Fe_3(THT)_2(NH_4)_3$ MOF with film thickness at room temperature. These I-V curves display Ohmic response between –0.5 and +0.5 V. The electrical conductance increases with film thickness.

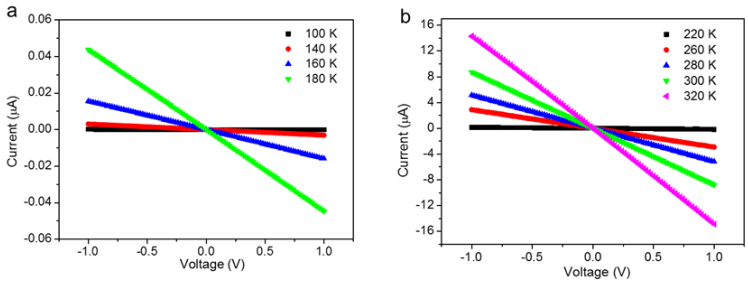

Figure 5.27. Temperature dependent I-V curves of the $Fe_3(THT)_2(NH_4)_3$ MOF film with the thickness of 70±1 nm, displaying Ohmic response between –1.0 and 1.0 V.

References

(1) Li, H., Eddaoudi, M., O'Keeffe, M. & Yaghi, O. M. Design and synthesis of an exceptionally stable and highly porous metal-organic framework. Nature 402, 276-279 (1999).

(2) Furukawa, H., Cordova, K. E., O'Keeffe, M. & Yaghi, O. M. The chemistry and applications of metal-organic frameworks. Science 341, 1230444 (2013).

(3) Eddaoudi, M. et al. Systematic design of pore size and functionality in isoreticular MOFs and their application in methane storage. Science 295, 469-472 (2002).

(4) Murray, L. J., Dincă, M. & Long, J. R. Hydrogen storage in metal–organic frameworks. Chem. Soc. Rev. 38, 1294-1314 (2009).

(5) Farha, O. K. et al. De novo synthesis of a metal-organic framework material featuring ultrahigh surface area and gas storage capacities. Nat. Chem. 2, 944-948 (2010).

(6) McDonald, T. M. et al. Cooperative insertion of CO2 in diamine-appended metal-organic frameworks. Nature 519, 303-308 (2015).

(7) Shimomura, S. et al. Selective sorption of oxygen and nitric oxide by an electron-donating flexible porous coordination polymer. Nat. Chem. 2, 633-637 (2010)

(8) Li, J. R., Sculley, J. & Zhou, H. C. Metal-organic frameworks for separations. Chem. Rev. 112, 869-932 (2012).

(9) Peng, Y. et al. Metal-organic framework nanosheets as building blocks for molecular sieving membranes. Science 346, 1356-1359 (2014).

(10) Liao, P., Huang, N., Zhang, W., Zhang, J. & Chen, X. Controlling guest conformation for efficient purification of butadiene. Science 356, 1193-1196 (2017).

(11) Lee, J. Y. et al. Metal-organic framework materials as catalysts. Chem. Soc. Rev., 38, 1450-1459 (2009).

(12) Zhang, T. & Lin, W. Metal-organic frameworks for artificial photosynthesis and photocatalysis. Chem. Soc. Rev. 43, 5982-5993 (2014).

(13) Zhu, L., Liu, X., Jiang, H. & Sun, L. Metal-organic frameworks for heterogeneous basic catalysis. Chem. Rev. 117, 8129-8176 (2017).

(14) Talin, A. A. et al. Tunable electrical conductivity in metal-organic framework thin-film devices. Science 343, 66-69 (2014).

(15) Sun, L., Campbell, M. G. & Dincă, M. Electrically conductive porous metal-organic frameworks. Angew. Chem. Int. Ed. 55, 3566-3579 (2016).

(16) Stassen, I. et al. An updated roadmap for the integration of metal-organic frameworks with electronic devices and chemical sensors. Chem. Soc. Rev. 46, 3185-3241 (2017).

(17) Campbell, M. G., Liu, S. F., Swager, T. M. & Dincă, M. Chemiresistive sensor arrays from conductive 2D metal-organic frameworks. J. Am. Chem. Soc. 137, 13780-13783 (2015).

(18) Hmadeh, M. et al. New porous crystals of extended metal-catecholates. Chem. Mater. 24, 3511-3513 (2012).

(19) Sheberla, D. et al. High electrical conductivity in Ni3 (2,3,6,7,10,11-hexaiminotriphenylene)2, a semiconducting metal-organic graphene analogue. J. Am. Chem. Soc. 136, 8859-8862 (2014).

(20) Sheberla, D. et al. Conductive MOF electrodes for stable supercapacitors with high areal capacitance. Nat. Mat. 16, 220-224 (2017).

(21) Kambe, T. et al. π-Conjugated nickel bis(dithiolene) complex nanosheet. J. Am. Chem. Soc. 135, 2462-2465 (2013).

(22) Kambe, T. et al. Redox control and high conductivity of nickel

bis(dithiolene) complex π-nanosheet: a potential organic two-dimensional topological insulator. J. Am. Chem. Soc. 136, 14357-14360 (2014).

(23) Huang, X. et al. A two-dimensional π-d conjugated coordination polymer with extremely high electrical conductivity and ambipolar transport behaviour. Nat. Commun. 6, 7408 (2015).

(24) Sun, L., Sarah S. Park, S. S., Dennis Sheberla, D. & Dincă, M. Measuring and reporting electrical conductivity in metal-organic frameworks. J. Am. Chem. Soc. 138, 14772-14782 (2016).

(25) Clough, A. J.; Skelton, J. M.; Downes, C. A.; de la Rosa, A. A.; Yoo, J. W.; Walsh, A.; Melot, B. C. & Marinescu, S. C. Metallic conductivity in a two-dimensional cobalt dithiolene metal-organic framework. J. Am. Chem. Soc. 139, 10863-10867 (2017).

(26) Ulbricht, R., Hendry, E., Shan, J., Heinz, T.F. & Bonn, M. Carrier dynamics in semiconductors studied with time-resolved terahertz spectroscopy. Rev. Mod. Phys. 83, 543-586 (2011).

(27) Makiura, R. et al. Surface nano-architecture of a metal-organic framework. Nat. Mat. 9, 565-571 (2010).

(28) Dong, R. et al. Large-area, free-standing, two-dimensional supramolecular polymer single-layer sheets for highly efficient electrocatalytic hydrogen evolution. Angew. Chem. Int. Ed. 54, 12058-12063 (2015).

(29) Lukose, B.; Kuc, A. & Heine, T. The structure of layered covalent-organic frameworks. Chemistry Eur. J. 17, 2388-2392 (2011).

(30) Dirk, C. W. et al. Metal poly(benzodithio1enes). Macromolecules 19, 266-269 (1986).

(31) Sellmann, D., Geck, M. & Moll, M. Transition-metal complexes with sulfur ligands. 62. Hydrogen evolution upon reaction of protons with sulfur-coordinated iron (II) complexes. Investigation of the H+, H2, and H-interactions with iron 1,2-benzenedithiolate. J. Am. Chem. Soc. 113, 5259-5264 (1991).

(32) Roy, N., Sproules, S., Bill, E., Weyhermüller, T. & Wieghardt, K. Molecular and electronic structure of the square planar bis(o-amidobenzenethiolato)iron(III) anion and its bis(o-

quinoxalinedithiolato)iron(III) analogue. Inorg. Chem. 47, 10911-10920 (2008).

(33) Darago, L. E., Aubrey, M. L., Yu, C., Gonzalez, M. I. & Long, J. R. Electronic conductivity, ferrimagnetic ordering, and reductive insertion mediated by organic mixed-valence in a ferric semiquinoid metal-organic framework. J. Am. Chem. Soc. 137, 15703-15711 (2015).

(34) Fonari, A. & Sutton, C. Validation of the effective masses calculated using finite difference method on a five-point stencil for inorganic and organic semiconductors. arXiv:1302.4996

(35) Chattopadhyay, D. & Queisser, H. J. Electron scattering by ionized impurities in semiconductors. Rev. Mod. Phys. 53, 745 (1981).

(36) Chen, J. H., Jang, C., Xiao, S., Ishigami, M. & Fuhrer, M. S. Intrinsic and extrinsic performance limits of graphene devices on SiO2. Nat. Nano. 3, 206-209 (2008).

(37) Ma, N. & Jena, D. Charge scattering and mobility in atomically thin semiconductors. Phys. Rev. X 4, 011043 (2014);

(38) Radisavljevic, B. & Kis, A. Mobility engineering and a metal-insulator transition in monolayer MoS2. Nat. Mat. 12, 815-820 (2013).

(39) Kaasbjerg, K., Thygesen, K. S. & Jacobsen, K. W. Phonon-limited mobility in n-type single-layer MoS2 from first principles. Phys. Rev. B 85, 115317 (2012).

(40) Sun, L. et al. Is iron unique in promoting electrical conductivity in MOFs? Chem. Sci. 8, 4450-4457 (2017).

(41) Mayadas F. and Shatzkes M. Electrical-resistivity model for polycrystalline films: the case of arbitrary reflection at external surfaces. Phys. Rev. B 1, 1382 (1970).

(42) Rivnay J., Jimison L. H., Northrup J. E., Toney M. F., Noriega R., Lu S., Marks T. J., Facchetti A. and Salleo A. Large modulation of carrier transport by grain-boundary molecular packing and microstructure in organic thin films. Nature Materials 8, 952-958 (2009).

(43) Steinhauser, J., Fay, S., Oliveira, N., Vallat-Sauvain, E. And Ballif, C. Transition between grain boundary and intragrain scattering transport

mechanisms in boron-doped zinc oxide thin films. Appl. Phys. Lett. 90, 142107 (2007).

(44) Klencsár, Z., Kuzmann, A. & Vértes, A. User-friendly software for Mössbauer spectrum analysis. J. Radioanal. Nucl. Chem. 210, 105-118 (1996).

(45) Kresse, G. & Hafner, J. Ab initio molecular dynamics for liquid metals. Phys. Rev. B 47, 558-561 (1993).

(46) Perdew, J. P., Burke, K. & Ernzerhof, M. Generalized gradient approximation made simple. Phys. Rev. Lett. 77, 3865-3868 (1996).

(47) Grimme, S. Semiempirical GGA-type density functional constructed with a long-range dispersion correction. J. Comp. Chem. 27, 1787-1799 (2006).

(48) Blöchl, P. E. Projector augmented-wave method. Phys. Rev. B 50, 17953-17979 (1994).

(49) Kresse, G.; Joubert, D. From ultrasoft pseudopotentials to the projector augmented-wave method. Phys. Rev. B 59, 1758-1775 (1999).

(50) Anisimov, V. I., Aryasetiawan, F. & Lichtenstein, A. I. First-principles calculations of the electronic structure and spectra of strongly correlated systems: the LDA+ U method. J. Phys.: Condens. Matter 9, 767-808 (1997).

(51) Dudarev, S. L., Botton, G. A., Savrasov, S. Y., Humphreys, C. J. & Sutton, A. P. Electron-energy-loss spectra and the structural stability of nickel oxide: An LSDA+U study. Phys. Rev. B 57, 1505-1509 (1998).

(52) J. Zhou, J. & Sun, Q. Magnetism of Phthalocyanine-Based Organometallic Single Porous Sheet. J. Am. Chem. Soc. 133, 15113-15119 (2011).

(53) Calzolari, A., Ferretti, A. & Nardelli, M. B. Ab initio correlation effects on the electronic and transport properties of metal(II)-phthalocyanine-based devices. Nanotechnology 18, 424013 (2007).

(54) Bernien, M. et al. Tailoring the nature of magnetic coupling of Fe-porphyrin molecules to ferromagnetic substrates. Phys. Rev. Lett. 102, 047202 (2009).

(55) Lach, S., Altenhof, A., Tarafder, K., Schmitt, F., Ali, M., Vogel, M., Sauther, J., Oppeneer, P. M. & Ziegler, C. Metal-organic hybrid interface states of a

ferromagnet/organic semiconductor hybrid junction as basis for engineering spin injection in organic spintronics. Adv. Funct. Mater. 22, 989-997 (2012).

(56) Li, W., Sun, L., Qi, J., Jarillo-Herrero, P., Dincă, M. & Li, J. High temperature ferromagnetism in π-conjugated two-dimensional metal–organic frameworks. Chem. Sci. 8, 2859-2867 (2017).

(57) Yamashita. T. & Hayes, P. Analysis of XPS spectra of Fe2+ and Fe3+ ions in oxide materials. Appl. Surf. Sci. 254, 2441-2449 (2008).

(58) Fujii, T.; de Groot, F. M. F.; Sawatzky, G. A.; Voogt, F. C.; Hibma, T. & Okada, K. In situ XPS analysis of various iron oxide films grown by NO2-assisted molecular-beam epitaxy. Phys. Rev. B 59, 3195-3202 (1999).

(59) Cao, R.; Thapa, R.; Kim, H.; Xu, X.; Kim, M. G.; Li, Q.; Park, N.; Liu, M. & Cho, J. Promotion of oxygen reduction by a bio-inspired tethered iron phthalocyanine carbon nanotube-based catalyst. Nat. Commun. 4, 2076 (2013).

(60) Kim, H.; Seo, D.; Kim, H.; Park, I.; Hong, J.; Park, K. & Kang, K. Multicomponent effects on the crystal structures and electrochemical properties of spinel-structured M3O4 (M = Fe, Mn, Co) anodes in lithium rechargeable batteries. Chem. Mater. 24, 720-725 (2012).

(61) Liu, C.; Zhang, Y.; Jia, J.; Sui, Q.; Ma, N. & Du, P. Multi-susceptibile single-phased ceramics with both considerable magnetic and dielectric properties by selectively doping. Scientific Reports 5, 9498 (2015).

(62) Eisenberg, R. & Harry B. Gray, H. B. Noninnocence in metal complexes: a dithiolene dawn. Inorg. Chem. 50, 9741-9751 (2011).

(63) Foster, M. E.; Sohlberg, K.; Spataru, C. D. & Allendorf, M. D. Proposed modification of the graphene analogue Ni3(HITP)2 to yield a semiconducting material. J. Phys. Chem. C 120, 15001-15008 (2016).

(64) Chen, S.; Dai, J. & Zeng, X. Metal-organic Kagome lattices M3(2,3,6,7,10,11-hexaiminotriphenylene)2 (M = Ni and Cu): from semiconducting to metallic by metal substitution. Phys. Chem. Chem. Phys. 17, 5954-5958 (2015).

(65) Sumi, H. & Toyozawa, Y. Urbach-martienssen rule and exciton trapped

momentarily by lattice vibrations. J. Phys. Soc. Jpn. 31, 342-358 (1971).

(66) Schreiber, M. & Toyozawa, Y. Numerical experiments on the absorption lineshape of the exciton under lattice vibrations. III. The Urbach rule. J. Phys. Soc. Jpn. 51, 1544-1550 (1982).

(67) A.G. Zabrodskiĭ, A. G. & Zinov'eva, K. N. Low-temperature conductivity and metal-insulator transition in compensate n-Ge. Sov. Phys. JETP 59, 425-433 (1984).

SUMMARY

Solar energy conversion technologies are considered among the most promising strategies of exploiting renewable energy resources for sustainable development of our society. These technologies have a common ultimate goal: converting solar energy into electricity (in photovoltaics) or storing solar energy into chemicals (solar fuels) at high efficiency/cost ratios. In order to achieve high efficiency/cost ratios, many different solar cell and solar fuel cell approaches have been developed and implemented. Specifically, employing inorganic-organic hybrid nanostructured materials as active or passive building blocks show great potential for fulfilling this goal. Among them, large area-to-volume ratio architectures like those employed in dye-sensitized solar cells as well as photocatalytic water splitting cells are among the most interesting concepts in each field thanks to their low cost of fabrication, linked with the low energy input of processing and the employment of abundant materials on their development. However, the efficiencies for these technologies are yet not fully optimized. The photoconversion efficiencies for these technologies are closely determined by the photo-induced charge carrier dynamics in the bulk as well as at the interface of components comprising the devices. Therefore it is of a huge practical significance to precisely measure, characterize, model and ultimately tune the charge carrier dynamics (charge carrier transport and interfacial transfer) via a careful selection and design of key components.

Time-resolved terahertz spectroscopy (TRTS) is a femtosecond-laser pump-probe based technique where the material is first excited by a pump pulse and then probed by a THz pulse with sub-picosecond resolution. This technique enables us to study the non-equilibrium carrier dynamics of materials. Furthermore, we can retrieve the complex optical properties at any pump-probe delay, such as the pump induced frequency-resolved complex conductivity of a given sample.

In Chapter 3 and 4 we studied photo-induced electron transfer (ET) processes in nanographene-sensitized metal oxide films. Nanographenes are carbon-based and non-toxic. Their size/edge/shape morphology and hence their optoelectronic properties can be precisely defined. The size-dependent energy gap of nanographenes holds the potential for using them in order to absorb the entire solar spectrum, a unique advantage compared with other conventional molecular sensitizers. The high surface area provided by the mesoporous metal oxide films,

together with the strong extinction coefficient of nanographenes make sensitized solar cells and solar fuels made from these constituents to promise a superior performance when compared with conventional approaches. However, the efficiencies of current prototypes based on these components are yet much lower than those based on e.g. ruthenium dyes. This has been linked from several authors to, among other factors, the poor control of the bonding geometry at the interfaces defined between donor and acceptor. Using TRTS, we provided the first experimental evidence on how physisorption or chemisorption of nanographenes onto mesoporous metal oxides affects related interfacial carrier dynamics (and hence photoconversion efficiency). In Chapter 3 we presented these results, where we resolved an almost 2-order-of-magnitude speed-up of the photo-induced electron transfer at the interfaces of the chemically absorbed (via carboxylate groups) C 42 nanographenes-sensitized metal oxides compared to that where sensitizers are physically absorbed. Our observables can be rationalized by an enhanced donor-acceptor coupling strength (i.e. donor-acceptor wavefunction overlap) in chemisorbed case. These findings indicate that functionalizing the nanographenes with anchoring head groups opens an avenue for the enhancement of photocurrent and eventually overall efficiency in carbon-based sensitizer/oxide electrodes employed in solar energy conversion schemes.

In Chapter 4 we analyzed how the size of nanographenes (defining their absorption onset) affects interfacial electron transfer rates in sensitized systems. The energy gap of nanographenes exhibited a power-law dependence on the size (i.e. the number of fused rings), in good agreement with theoretical predictions. Applying TRTS, we resolved that ET in these systems was characterized by a biphasic mechanism, likely linked with hot and cold ET channels respectively. We also found a sensitizer size dependence towards both ET rate components, that can be interpreted and modeled by the many-body Marcus theory. Within this theoretical framework, electrons are transferred from the nanographene towards the oxide faster as nanographenes decrease their size (i.e. enlarging the energy gap). In order to achieve the maximum charge collection efficiency at the metal electrode, ET from the sensitizer should favorably kinetically compete with radiative relaxation within the nanographene, while having an absorption onset (defined by its size) enabling best matching to the solar spectrum (around 1.4eV following the Shockley-Queisser formalism).

In Chapter 5 we analyzed novel two-dimensional (2D) electrically conductive metal-organic frameworks (MOFs). Due to their large and tunable porosity and

thus large surface-to-volume ratios, MOFs have been considered as ideal candidates for photocatalysis. However, this aspect is strongly limited by the fact that most of the MOFs developed to date are insulating, and therefore do not absorb visible light. In this work, we investigated the optoelectronic properties as well as the nature of charge transport in a novel semiconducting, π-d conjugated, porous $Fe_3(THT)_2(NH_4)_3$ 2D MOF. TRTS was employed to model the frequency-resolved photoconductivity of the material, from which a Drude response was obtained, indicating that band-like charge carrier transport (rather than hopping) was operative in the systems. From the Drude fit, a record charge mobility of ~220 cm^2/Vs at room temperature was demonstrated. Moreover, the temperature dependence for the complex photoconductivity revealed that scattering rates and thus mobilities are primarily limited by impurity scattering. Therefore, the mobilities inferred from TRTS refer to the lower limit. By comparing the optical and electrical conductivities of this material, we found a quantitative agreement, indicating that the long-range charge transport in our 2D MOFs was not affected by grain boundary scattering, an aspect that was rationalized by the strong p-doping in analyzed samples.

As an outlook, we anticipate that the conductivity, mobility, and bandgap of all graphene-like MOF analogs can be controlled through appropriate chemical design. Specifically, in-plane engineering can be pursued via metal substitution, modification of functional groups and organic ligands, and even by selecting appropriate guest molecules within the pores. Out-of-plane engineering is also possible by the design of 2D van der Waals heterostructures by, e.g., controlling the spacing between layers and/or the relative alignment between planes. Furthermore, controlled stacking of 2D MOF layers of dissimilar materials might allow the development of heterostructures with unique physical and chemical properties. The large degree of chemical and structural tunability for this planar (and porous) class of 2D MOF materials provides plenty of room for development in this exciting field of research. Important challenges include identifying reliable correlations between chemical composition, electronic structure, conductivity and charge carrier mobility. From a synthetic point of view, developing single crystals and delaminating them into single layers will enable not only fundamental studies of structure-properties relations, but also the development of MOF-based functional devices where long-range free carrier motion is required.

SAMENVATTING

Het omzetten van zonne-energie en de ontwikkeling van technieken die dat mogelijk maken wordt als de meest veelbelovende strategie gezien om hernieuwbare energiebronnen te benutten voor de duurzame ontwikkeling van onze maatschappij. Deze technieken hebben een gezamenlijk doel: zonne-energie omzetten in elektriciteit (via het fotovoltaïsche effect) of zonne-energie opslaan in chemische vorm (de zogenaamde zonne-brandstoffen) beide met hoge efficiëntie en lage kosten. Om dit doel te bereiken zijn er de afgelopen jaren veel verschillende types fotovoltaïsche zonnecellen en zonne-brandstofcellen ontwikkeld en toegepast. Dit geldt in bijzonder voor de veelbelovende toepassing van inorganische-organische hybride nanogestructureerde materialen, zowel als actieve en passieve bouwstenen. Vooral materialen met een hoge oppervlakte-volume verhouding, zoals toegepast in Dye-sensitized solar cells (DSSCs) en fotokatalytische cellen die water kunnen splitsen, zijn de meest interessante concepten in beide toepassingen. Dit is mede dankzij de lage productiekosten, als gevolg van het gebruik van veel voorkomende grondstoffen voor fabricage en het geringe energieverbruik bij de productie. De efficiëntie van deze materialen is echter nog niet optimaal. De fotoconversie efficiëntie van deze materialen wordt in hoge mate bepaald door het gedrag van fotogegenereerde ladingsdragers zowel binnenin alsook aan het oppervlak van het materiaal. Het is daarom van groot praktisch belang om het dynamische gedrag van de ladingsdragers precies te meten, te karakteriseren, en te modelleren met als doel om de dynamica uiteindelijk te kunnen controleren door middel van zorgvuldige selectie en ontwerp van belangrijke onderdelen.

Tijdsopgeloste Terahertz spectroscopie (TRTS) is een techniek waarmee een materiaal door middel van een femtoseconde laserpuls van zichtbaar licht wordt geëxciteerd. Een bepaalde tijd later (typisch picoseconden tot nanoseconden) worden de fotogegenereerde ladingsdragers gekarakteriseerd door middel van een Terahertz laser puls met sub-picoseconde resolutie. Deze techniek stelt ons in staat om in een materiaal de dynamica van ladingdragers die nog niet in evenwicht zijn te bestuderen. Bovendien kunnen we reële en imaginaire delen van de complexe optische eigenschappen vaststellen op ieder tijdstip na excitatie. Aldus wordt direct toegang verkregen tot de frequentie-afhankelijke complexe conductiviteit van ladingsdragers in het materiaal.

In hoofdstuk 3 en 4 hebben we de overdracht van fotogegenereerde elektron bestudeerd in metaal-oxide films die lichtgevoelig zijn gemaakt met nanografeen. Nanografeen is gebaseerd op koolstof en is niet giftig. De grootte en vorm van nanografeen, en daardoor ook de optisch-electrische eigenschappen ervan, kunnen zeer nauwkeuring worden bepaald. De bandgap van nanografeen is afhankelijk van de grootte en vorm van het deeltje, dus er is groot potentieel om uiteindelijk het hele zonnespectrum te absorberen, een uniek voordeel vergeleken met conventionele moleculaire deeltjes. Het grote oppervlak van mesoporeuze metaal-oxide films gecombineerd met de sterke absorptie van licht door nanografeen suggereren dat zonnecellen en zonne-brandstofcellen die deze combinatie gebruiken een superieure efficiëntie hebben vergeleken met conventionele aanpak. De efficiëntie van de huidige prototypes is echter nog steeds veel lager dan de, bijvoorbeeld, op ruthenium dyes gebaseerde cellen. Dit verschil wordt, onder andere, veroorzaakt door de slechte controle over de manier waarop nanografeen bindt op het oppervlak van het metaal-oxide en nanografeen, zoals gerapporteerd door verscheidende andere auteurs. Met behulp van TRTS hebben we het eerste experimentele bewijs gevonden dat fysisorptie of chemisorptie van nanografeen op mesoporeuze metaal-oxide films de dynamica tussen ladingsdragers aan het grensoppervlak beïnvloed, en daardoor ook de fotoconversie efficiëntie .

In hoofdstuk 3 wordt aangetoond dat de transfer van elektronen vanuit het chemisch geabsorbeerde C42 nanografeen naar de metaal-oxide films (via carboxylaat groepen) een factor 100 sneller is dan wanneer het nanografeen fysisch geadsobeerd is. Onze observaties kunnen verklaard worden door een verbeterde koppeling (golffunctie overlap) tussen het nanografeen en de metaaloxide film in het geval van chemisorptie. Deze resultaten geven aan dat op maat gemaakt nanografeen met specifieke bindingsgroepen de mogelijkheid biedt voor de verbetering van fotostroom. Dit kan leiden tot een verhoging van de totale efficiëntie van de metaal-oxide electrodes die lichtgevoelig zijn gemaakt met op koolstof gebaseerde nanostructuren voor de omzetting van zonne-energie.

In hoofdstuk 4 analyseren we hoe de grootte van het nanografeen deeltje – wat de absorptie van de precieze golflengte van licht bepaalt – van invloed is op de elektron-overdracht aan het grensvlak bij lichtgevoelig gemaakte systemen. De bandgap van nanografeen laat een power-law afhankelijkheid zien van de grootte van het deeltje (bepaald door het aantal gefuseerde ringen), zoals theoretisch

voorspeld. Met TRTS hebben we gevonden dat de elektron-overdracht in deze systemen wordt gekenmerkt door een bifasisch mechanisme, waarschijnlijk door 'hete' en 'koude' elektron-overdracht. We hebben ook gevonden dat de snelheid van de elektron-overdracht in beide gevallen afhankelijk is van grootte van het nanografeen deeltje en kan gemodelleerd met de Many-Body Marcus theorie. In dit theoretische model worden elektronen sneller vanuit het nanografeen naar de metaal-oxide overgedragen als het nanografeen deeltje kleiner, en dus de band gap groter, is. Om de hoeveelheid lading aan de metaal-oxide elektrode te maximaliseren, moet de elektron-overdracht in het meest gunstigste geval kinetisch concurreren met de stralingsrelaxatie in het nanografeen en tegelijkertijd een door de grootte gedefinieerde absorptie afgestemd op het zonnespectrum van ongeveer 1.4eV, zoals beschreven in de Shockley-Queisser limiet.

In hoofdstuk 5 hebben we tweedimensionale elektrisch geleidende Metal Organic Frameworks (MOFs) onderzocht. MOFs hebben een zeer grote en afstembare poreusheid en hebben dus een zeer grote volume-oppervlakte verhouding waardoor ze als ideale kandidaten voor fotokatalyse worden gezien. Helaas hebben de meeste tot nu toe geproduceerde MOF's isolerende eigenschappen, waardoor ze geen zichtbaar licht absorberen. Voor dit proefschrift hebben we de optischelektrische eigenschappen en de aard van het ladingtransport in een nieuw type halfgeleider MOF onderzocht, met name de π-d gebonden poreuze $Fe_3(THT)_2(NH_4)_3$ 2D MOF. TRTS werd toegepast om de frequentie-opgeloste fotoconductiviteit van het materiaal te verkrijgen. Het verkregen Drude conductiviteitsspectrum duidt op zgn. bandtransport van het geladen deeltje in dit materiaal. De analyse liet een record-hoge ladingsmobiliteit van ~220cm^2 /Vs zien, bij kamertemperatuur. Bovendien liet de temperatuur afhankelijke complexe fotoconductiviteit zien dat de verstrooiing, en dus de mobiliteit, hoofdzakelijk gelimiteerd werd door de onzuiverheden in het materiaal. De door TRTS gevonden mobiliteit is dus een ondergrens. De optische en elektrische conductiviteit van dit materiaal zijn ononderscheidbaar, hetgeen aanduidt dat het lange-afstands ladingstransport in onze 2D MOFs niet beïnvloed werd door verstrooiing aan de oppervlakken van kristallietjes, een aspect dat werd verklaard door de sterke p-dotering van de geanalyseerde monsters.

In de toekomst verwachten we dat de conductiviteit, mobiliteit van ladingsdragers en bandgap van alle op grafeen gebaseerde MOFs kunnen worden gecontroleerd door adequaat chemisch ontwerp. In het bijzonder kan dat via 'in-

plane' technieken zoals het kiezen van andere metalen, aanpassing van functionele groepen en organische liganden en zelfs via het kiezen van geschikte gastmoleculen in de poriën. Met 'out-of-plane' technieken is het ook mogelijk om 2D van der Waals heterostructuren te ontwerpen door, bijvoorbeeld, de ruimte tussen de lagen te controleren en/of de uitlijning ten opzichte van elkaar. Verder is het mogelijk om 2D MOFs uit verschillende materialen te stapelen waarmee wellicht heterostructuren ontstaan die unieke fysieke en chemische eigenschappen hebben. De grote mate waarin de chemische en structurele eigenschappen in deze klasse van vlakke en poreuze 2D MOF materialen aan te passen zijn, betekent dat er nog zeer veel ontwikkeling mogelijk is in dit uiterst boeiende onderzoeksgebied. Belangrijke uitdagingen zijn o.a. het identificeren van betrouwbare correlaties tussen chemische samenstelling, elektronische structuur, conductiviteit en mobiliteit van de ladingdragers. Vanuit het oogpunt van synthese is er ontwikkeling mogelijk om enkelvoudige kristallen te delamineren in enkelvoudige lagen zodat niet alleen fundamenteel onderzoek naar de relatie tussen structuur en eigenschappen kan worden uitgevoerd maar ook de ontwikkeling mogelijk is van op MOF gebaseerde structuren waarin de mobiele ladingdragers grote afstanden moeten afleggen.

ACKNOWLEDGEMENTS

First of all, I would like to give my sincere gratefulness to all persons who have helped me on my way of finishing PhD studies, especially to those whose names are not included in this acknowledgements. It is impossible for me to complete this thesis without your support.

Above all I would like to give full credit to my two supervisors: Mischa and Enrique. Thank you so much for giving me the opportunity to study and grow up in such a sweet and active international academia! Mischa, thank you for creating such a highly interdisciplinary atmosphere in our department. By participating in collaborations at all levels as well as attending seminars in all fields I feel my horizon has been unprecedentedly broadened. Thanks to your all-along patience as well as support, I am ready to embrace any challenge on my way of pursuing the scientific truth. Enrique, Enrique, Enrique. Forgive me to call your name for three times. Thank you for taking me when I was in need of help. Thank you for trusting me of beating my PhD projects even though I had zero knowledge about THz spectroscopy. Thank you for empathizing with me every time that I couldn't control my emotion and was unprofessional. The lessons you have taught me are from every perspective, including but not limited to conquering the fear of working with an optical setup, learning language from physicists, coping with unsuccessful research projects as well as challenging myself out of comfort zone. In particular I truly appreciate all your effort on supporting my completion of this manuscript within the graduate period! Bearing your words in my mind, I will try to "work not hard but smartly" and keep fighting every fight in future.

Altogether I would like to address my appreciations to the entire AK-Bonn group particularly to Yuki Nagata, Maksim Grechko, Hao Lv, Hai Wang, Heejae Kim, Ellen Backus, Sapun Parekh, Dmitry Turchinovich, Johannes Hunger, Marc-Jan Van Zadel, Florian Gericke, Hansjoerg Mengesh, Walter Scholdei, Gabriele Herrmann and our secretary Laurie Gangloff. Along with this list, I also would like to give credit to all collaborators in and out of the institute especially to Akimitsu Narita, Klaus Muellen, Xinliang Feng, Renhao Dong, Ian Hou, Xue-Lin Yao and Xiao-Ye Wang. Without your help and contribution, none of the scientific publications included in this thesis will be achieved.

I would like to give a special acknowledgment to the nanoPV group and the general THz sub-group. Without your help I will not get adapted to the THz spectroscopy and gain deeper understanding of the physics behind the

spectroscopy so quickly and smoothly. Melike, thank you for being patient to me all the time even when you were under pressure before graduate. I will never forget how your down-to-the-earth interpretation of the working principle as well as your inspiring supervision of the experimental setup helped me to walk out an affirmative step in the laser lab. Marco, thank you for troubleshooting problems from the setup as well as providing professional feedbacks of my scientific research. I sincerely appreciate your generosity of sharing knowledge from nonlinear optics as well as solid state physics with me whenever I need. Sergio, thank you for supporting me as a team member. Keno, you are probably the person I bothered most frequently out of my groupmates. Besides helping me with technical issues, you are also eager to share with me your enthusiasm about versatile scientific topics. I was amazed and deeply infected by your broad knowledge and critical thinking. It was such a joy to co-operating with you via seeking for the solution to the scientific questions. Zuanming, Wentao, Ivan, Hassan, Eduard, Francesco and Zoltan, thank you for all precious discussions we had regarding the THz physics. Alex, Wenhao, Heng, Shuai, Xiaoqing and Paniz, thank you for trusting me and helping me be more open-minded via our pleasant discussions.

Apart from science, I am also grateful for all the support I have received from life during the past four and a half years. My dear office fellows, because of your company, I feel I have never been alone. Sergio and Vasilis, thank you for the easy and friendly atmosphere you created in 1.508. Natalia, thank you for your generous help and Spanish passion. Amala and Prerna, thank you for being willing to share every happiness and sadness with me. I will never forget the unique group birthday celebration you ladies made for us and we still own you one. Tarek, you are probably the closest Muslim friend I have met until now. Thank you so much for helping me get through those hard times during the last period of my PhD studies. Ulmas, your easy-going personality and your shrewd mind just make me impossible not to like you. I guess I will always remember those walks and more impressively talks we had on our way home. Martina, thank you for being so tolerant of my random complaints. Every laugh, every small gift and every German vocabulary and so on, all of them will be in gold in the river of my memory. Masoud, Daria and Qiqi, thank you for being so supportive and understandable to me. I feel fortunate to share the same office with you all! In parallel I would like to thank all classmates in my German class. German is difficult to learn. But dear Eleni, you make the learning process funnier and more

interesting. And dear Soham, we knew each other and became good friends by attending the same class. Your rhetoric, your opinion about photography, your incredible love of food, I thank you for giving me the opportunity of experiencing for the first time of my life as an editor in JUNQ journal. Of course I would like to thank the company of other classmates as well, just to name a few here, Grace, Sudipta, Heloise. Along with this list, I would like to thank the support offered by other colleagues in our department particularly to Jenée Cyran, Christian Malm, Stephanie Jung, Sachin Kumar, Mischa Schwendy, Sabine Pütz, Lisa Dreier, Malte Deiseroth, Michael Donovan, Simon Bretschneider, Jonas Pfisterer, Laura Vietze, Amelie Ehrhard and Leonie Driessen.

In line with the support I was offered from life and work, I would like to thank specially to my beloved Chinese colleagues and friends at Mainz. Dear Xiaomin, I feel so grateful for all the generous care, concern and suggestions you offered to me. In my eyes, it is an honor to have you as an elder sister watching my stumble growth and more importantly helping me regain optimism and hope when I was drown in the valley of frustration. To say nothing about every invitation from you for the warm-hearted home-like reunion during the grand Chinese festivals. Dear Ge, it was a coincidence to bump into you and afterwards we became close friends. Thank you for your unconditional trust and frank advices so that I only started to feel lonely after you moved out of Mainz. Dear Xiao, Shumei, Fujie, Guangjiang, Yujen, Yang, Minghan, Qiang, Yuling, Sheng, Cong and Maoqi, thank you from the bottom of my heart for coloring my life at Mainz in such a wonderful way. Those strokes you painted on my life canvas, including but not limited to the food trips, home cooking, hiking, cycling, constitute the happiest time during my stay in this lovely city. And of course I would not forget to thank our MPIP table-tennis group particularly to Wei, Run, Chaojian, Ke, Yinke and Jianhua. Because of your company, I feel I am connected to my homeland in this German city.

行将搁笔，我想把最后的致谢留给我的父母和亲人。千言万语，汇于孟郊的《游子吟》中：

“慈母手中线，游子身上衣。
临行密密缝，意恐迟迟归。
谁言寸草心，报得三春晖。”